Alma Mater Studiorum – Università di Bologna

DOTTORATO DI RICERCA
IN ASTRONOMIA

Ciclo XXI

Settore/i scientifico disciplinari di afferenza: **Area 02 - Scienze Fisiche**
FIS/05 Astronomia e Astrofisica

ASTRONOMICAL SITE TESTING IN THE ERA OF THE EXTREMELY LARGE TELESCOPES

Presentata da: **GIANLUCA LOMBARDI**

Coordinatore di Dottorato
Ch.mo Prof. Lauro Moscardini

Relatori
Ch.mo Prof. Bruno Marano

Dott.ssa Valentina Zitelli

Esame finale anno 2008

This PhD thesis has been partially funded by National Institute for Astrophysics (INAF), Bologna Astronomical Observatory and partially by the European Extremely Large Telescope Design Project.

Al Desierto de Atacama, alla Puna e all'Altiplano,
ai loro bastioni dalle cime rosse, torride di giorno, ma gelide di notte,
alle stelle dell'Emisfero Australe e alla Croce del Sud,
alla gente del deserto e ai loro sorrisi accoglienti,
con umiltà e profonda gratitudine
per essere oramai parte della mia vita.

Al Desierto de Atacama, a la Puna y al Altiplano,
a cuyos bastiones de cumbres rojas, calurosas en el día, pero heladas en la noche,
a las estrellas del Hemisferio Austral y a la Cruz del Sur,
a la gente del desierto y sus sonrisas acogedoras,
con humildad y prufunda gratitud
por ser ya parte de mi vida.

To the Desierto de Atacama, the Puna and the Altiplano,
to their bastions with red summits, hot in the day, but cold in the night,
to the stars of the Southern Hemisphere and the Southern Cross,
to the people of the desert and their smiles,
with humility and gratefulness
for being already part of my life.

Contents

1 Aims of the project **1**
- 1.1 A brief history of site testing . . . 1
- 1.2 The development of the project . . . 2

2 Sky quality **5**
- 2.1 Introduction . . . 5
- 2.2 A brief introduction to the structure of the Earth's atmosphere . . . 5
  - 2.2.1 Chemical composition . . . 5
  - 2.2.2 Thermal structure . . . 6
  - 2.2.3 Atmospheric layers . . . 6
  - 2.2.4 Absorption and emission . . . 8
- 2.3 The concept of seeing . . . 8
- 2.4 Statistics of the atmospheric turbulence . . . 10
- 2.5 Coherence time . . . 14
- 2.6 Isoplanatic angle . . . 15
- 2.7 The Strehl Ratio . . . 15
- 2.8 The effects of the seeing . . . 15

3 Astroclimatology of ground-based observatories **17**
- 3.1 Introduction . . . 17
- 3.2 Meteorological stations . . . 18
- 3.3 Data analysis methods . . . 20
- 3.4 Air temperature . . . 22
- 3.5 Air pressure . . . 23
  - 3.5.1 Long time scale air pressure . . . 23
  - 3.5.2 Short time scale air pressure variations . . . 25
  - 3.5.3 General weather conditions at ORM and Paranal . . . 26
- 3.6 The North Atlantic Oscillation (NAO) Index . . . 27

3.7 The Southern Oscillation Index (SOI) . . . 28
3.8 Relative humidity . . . 29
3.9 Analysis of the dew point . . . 31
3.10 Wind . . . 32
3.10.1 Wind speed limits for observational purposes . . . 36
3.11 Preliminary correlations between seeing and meteorological parameters . . . 37
3.11.1 Seeing and vertical temperature gradient . . . 37
3.11.2 Seeing and wind speed . . . 38
3.11.3 Seeing and wind direction . . . 39

4 Atmospheric dust and aerosol extinction 41
4.1 Introduction . . . 41
4.2 The dust monitor . . . 42
4.3 Data analysis . . . 43
4.4 Dust storms . . . 46
4.5 Aerosol atmospheric extinction in B, V, and I . . . 48
4.6 Summertime aerosol atmospheric extinction and TOMS aerosol index . . . 54

5 A study of the near-infrared atmospheric extinction on Paranal 57
5.1 Database and data reduction . . . 57
5.2 Data analysis . . . 58
5.2.1 Evolution in time of the zero point . . . 58
5.2.2 Effects of the Precipitable Water Vapour . . . 60
5.3 Determination of the atmospheric extinction coefficients . . . 61

6 Measuring the turbulence 65
6.1 The Differential Image Motion Monitor (DIMM) . . . 65
6.2 The Multi-Aperture Scintillation Sensor (MASS) . . . 66
6.2.1 MASS weighting functions . . . 67
6.3 SLope Detection And Ranging (SLODAR) . . . 69
6.3.1 SLODAR weighting functions . . . 70

7 Combining turbulence profiles from MASS and SLODAR 71
7.1 The reason to combine profiles from different instruments . . . 71
7.2 The problem of the weighting functions . . . 72
7.3 The method . . . 72
7.3.1 Restoration of the turbulence profile . . . 75
7.4 Results from the recombination . . . 78

8 The study of the evolution of the seeing at Paranal 81
8.1 Introduction . . . 81
8.2 Data analysis . . . 81
8.2.1 MASS+DIMM analysis . . . 82
8.2.2 MASS+SLODAR analysis . . . 83
8.3 The surface layer hypothesis . . . 83
8.4 The evolution of the seeing at Paranal . . . 84
8.5 The origin of the surface layer . . . 86
8.6 Some conclusions and a begin . . . 86
8.7 A median turbulence profile for Paranal . . . 89

A The site testing for the European Extremely Large Telescope **91**
A.1 The site selection process 91
A.2 The working packages 92
A.3 The sites 93
A.4 Instruments and tools 94
A.5 My personal participation in the E-ELT site testing 95

Bibliography **99**

Acknowledgements **103**

List of Figures

2.1 Atmospheric layers. Note the temperature trend in altitude. 7
2.2 A schematic example of a plane wavefront perturbation by two turbulent layers. 9
2.3 Different kinds of seeing contributions. 10
2.4 a) laminar motion around an obstacle; b) formation of a turbulent motion around the same obstacle. 10
2.5 Development of a turbulent regime in a cascade process: the scale decreases down to molecular motion. 11
2.6 C_n^2 profiles measured at San Pedro–Martir (Mexico) on 16 March 2000. . . 13
2.7 A simple scheme of the effects of the seeing. 16

3.1 Annual temperatures at Paranal (solid line), CAMC (dotted line) and TNG (thick dashed line). The short-dashed lines indicate the total averages: 12.8°C at Paranal and 8.8°C at CAMC. 22
3.2 Thermal excursion distribution at Paranal (solid line) and CAMC (dotted line) after 1998. The two sites are almost equivalent. 23
3.3 Top: annual P at Paranal Observatory. Bottom: annual P at CAMC. . . . 24
3.4 Top: Monthly P at Paranal anc CAMC. Bottom: Monthly T at Paranal and CAMC. 25
3.5 Temperature (solid) and pressure (dotted) variations at CAMC in a sample of January and July 1992. 26
3.6 On the left, (center) North Atlantic Oscillation Index vs: (top) down−time due to weather conditions and (bottom) annual temperature at CAMC. On the right, Southern Oscillation Index (middle) vs. annual temperatures (top) and annual air pressure (bottom) at Paranal. annual temperatures at CAMC site. 28
3.7 Averages of monthly P (top) and RH (bottom) at Paranal (left figure) and CAMC (right figure). 30

3.8 Nighttime annual percentage of time in which $\Delta T = T - T_{DP} < 1$ and 5°C at Paranal and CAMC in winter, spring, summer and autumn. 32
3.9 Nighttime wind roses at Paranal (1998-2006), and CAMC, TNG and NOT (1998-2004). 33
3.10 Nighttime evolution of the wind direction through the years at Paranal for quadrant W-NE (left figure) and quadrant E-SW (right figure). 36
3.11 Seeing in V band VS ΔT_2^{TNG} at TNG. 38
3.12 Seeing in V band VS w_{sp} at TNG. The two extremes for optimal observations are indicated. 39

4.1 Distribution of the atmospheric particles as a function of the different size, as measured by the Abacus TM301 during the years 2001-2006 (1-2 weeks each month depending on weather conditions). The gaps correspond to interruptions in the counter operations or to rejected values due to relative humidity $> 85\%$. 44
4.2 Seasonal distribution of the monthly dust at ORM: (top) 0.3 μm dust; (middle-top) 0.5 μm; (middle-bottom) 1.0 μm dust; (bottom) 5.0 μm dust. Different years are indicated by different symbols. 45
4.3 Dust storm event of 2002 December 25 and 26: 0.3 μm (solid), 0.5 μm (dots), 1.0 μm (short-dashes) and 5.0 μm (long-dashes). 46
4.4 Wind roses at TNG during dust storm events. 47
4.5 Distribution of the median dust counts during dust storms. Particles $\geq$1.0 μm are treated as if they follow an $r^2N(r)$ power law. 47
4.6 Extinction efficiency factor as a function of the particles radius in B (dots), V (solid), and I (short-dashes). 49
4.7 Distribution of the dust altitudes from ORM altitude for Eq. (4.5). 51
4.8 Median aerosol atmospheric extinction in B, V, and I in typical dust background conditions and in typical dust-storm conditions for each particle size. The biggest particles are dominant with respect to sub-micron particles. . . 52
4.9 k_{aer} versus k_{CAMC} in the case of dust storms. The linear fit has a confidence level of 0.8. 53
4.10 Typical local aerosol extinction increases $\Delta k(\lambda)$ in B (top), V(center) and I (bottom) in connection with dust storm events at ORM. The filled circles represent the expected $\Delta k(\lambda)$ due to 10 μm particles. 53
4.11 Summertime local aerosol atmospheric extinction versus TOMS Aerosol Index in V band. The correlation calculated with the Spearman's test between the points inside the zone delimited by the solid and the short-dashed lines has confidence level > 0.8. 55

5.1 Evolution in time of the zero point for J, J_S, H and K_S. The solid vertical lines indicate M1 recoating events, while dotted vertical lines indicate ISAAC interventions. 59
5.2 (top) ZP_0 values after each event; (bottom) differences between $ZP_{0,N}$ and $ZP_{0,N-1}$. 60
5.3 Monthly trend of the PWV on Paranal in photometric and clear nights. . . 61
5.4 Bouguer curves computed for P9 in each band. 62
5.5 κ-coefficients for J, J_S, H and K_S in different periods. The weighted averages are also reported: (solid line) periods case; (dashed line) monthly case. . . . 63

5.6 Monthly extinctions (different years have different symbols). There is no evidence of a seasonal trend. The weighted averages are also reported: (solid line) periods case; (dashed line) monthly case. 64

6.1 A simple scheme of the DIMM layout. 66
6.2 A simple scheme of the MASS concept. 67
6.3 MASS weighting functions. 68
6.4 A simple scheme of the SLODAR concept. 69
6.5 A simple scheme of the SLODAR layers. 70

7.1 En example of superimposition of SLODAR and MASS layers. 72
7.2 Transformation of the MASS triangular weighting functions (top) into rectangular ones (bottom) compatible with SLODAR. 73
7.3 A qualitative scheme of the new unified grid of layers. 74
7.4 A schematic representation of the atmospheric coverage of DIMM, MASS and SLODAR sensing. The representation of the recombined profile is also shown. 75
7.5 A SLODAR layer (grey area) fully inside a bin i (white area). 77
7.6 A SLODAR layer partially inside a bin i and partially inside a bin $(i+1)$. Symbols are the same of Figure 7.5. 77
7.7 The bin is only partially filled by the *last* SLODAR layer. Symbols are the same of Figure 7.5. 77
7.8 An example of turbulence profile restored combining MASS and SLODAR profiles. The Figure shows one frame of the whole sequence of the atmospheric profile obtained in real time during the acquisition process. The plot reports all the parameters calculated from the recombination. 80

8.1 (top) Comparison of the monthly evolution of the total C_n^2 of DIMM, GL and FA at Paranal between January 2005 and June 2007. The linear fit of the DIMM energy has a slope of 6.7, while it is 8.4 for the ground layer and -1.6 for the free atmosphere. (bottom) Percentage of $C_n^2(GL)$ in the total DIMM C_n^2. The linear fit of the points gives a slope of 0.6. 82
8.2 Ground layer atmospheric turbulence model at Cerro Pachon (Chile) (Figure 6 in Tokovinin&Travouillon 2006). 83
8.3 Distribution of ϵ_{ASL} and UT1 SH image quality. The median ASL seeing is 0.61 ± 0.20 arcsec, while median image quality of UT1 SH is 0.63 ± 0.19 arcsec. 85
8.4 Regression analysis of the monthly image quality at UT1 SH versus the monthly ASL seeing derived from our theoretical calculations (Lombardi et al. 2008b). 85
8.5 (left) Paranal wind rose in connection with $\Delta\epsilon = \epsilon_{DIMM}^{5/3} - \epsilon_{SH}^{5/3}$. (right) Paranal wind rose in connection with $\Delta T = T_{30} - T_2$ (Sarazin et al. 2008). . 86
8.6 Monthly DIMM seeing compared to ASL seeing. The monthly trend of the DIMM clearly increases (the trend is $\sim$0.1 arcsec per year), while the ASL seeing is almost constant in the considered period (the slope of the fit is null). 87
8.7 25 July 2008: Paranal DIMM seeing at 6 m above the ground and Portable DIMM seeing at 20 m above the ground. There is a strong evidence of the presence of the surface layer below 20 m. 88

8.8 MASS+DIMM. Typical profiles ASL for good (33%), median and bad (66%) seeing at Paranal. The statistics is made on the basis of 657 observing nights (20057 10-minutes averages) in the period between 2 January 2005 and 30 June 2007. 90

A.1 An artist impression of the European Extremely Large Telescope. 92
A.2 A World map reporting the locations of the candidate sites and nearby existing facilities. 93
A.3 Celestron C11 telescope and MASS-DIMM #31 device on the Optical Laboratory during alignment and collimation procedure. The telescope and the MASS-DIMM #31 will be installed at Tolanchar in the incoming months. . 96
A.4 Preparation of the MASS-DIMM on Astelco EQ mount for nighttime test observations at Paranal. 96
A.5 Astronomical Site Monitor installation at Macon in May 2008. 96
A.6 MASS-DIMM instrument installed at Macon. 97
A.7 This picture shows the typical Astronomical Site Monitor installations. From left to right: a hut for nighttime work, solar panels for energy providing, the 5 m MASS-DIMM tower and the automatic weather station. The picture has been taken at Macon in July 2008. 97
A.8 Lunar Scintillometer observing at Paranal in February 2008. 98
A.9 Portable DIMM on a 10 m tower at Ventarrones at the end of February 2008. The experiment consists in the comparison between the MASS-DIMM at 6 m and the DIMM at 11 m for surface layer analysis. 98

List of Tables

3.1 Geographical positions of Paranal and telescopes at ORM. All facilities are located well above the inversion layer. 18
3.2 Available databases for the observatories. 19
3.3 Mean annual temperatures at Paranal, CAMC and TNG. 21
3.4 Mean annual air pressure at Paranal and CAMC. 24
3.5 CAMC and Paranal typical delay in hours between variation of P and T. . 25
3.6 Strongest El Niño and La Niña episodes between 1985 and 2006. 28
3.7 Seasons definition at Paranal and CAMC. 29
3.8 Mean annual RH in cold seasons at Paranal and CAMC. 29
3.9 Mean annual RH in warm seasons at Paranal and CAMC. 30
3.10 Paranal and CAMC: annual number of nights in which RH has been higher than 80% and 85% for more than 50% of the duration of the night. Only nights which duration has been ≥ 6 hours have been used in the calculation. 31
3.11 1998-2004 nighttime wind direction percentages for TNG. 34
3.12 1998-2004 nighttime wind direction percentages for NOT. 34
3.13 1985-2004 nighttime wind direction percentages for CAMC. 35
3.14 1998-2006 nighttime wind direction percentages for Paranal. 35
3.15 Nighttime yearly evolution of the wind direction frequencies at Paranal from 1998 to 2006. 36
3.16 Nighttime wind speed statistics at Paranal (1998-2006) and CAMC, TNG and NOT (1998-2004). 37
3.17 Median DIMM seeing in connection with wind speed at Paranal between 10 April 2005 and 30 November 2007. Wind speed frequencies in the same period are also reported. 39
3.18 Median DIMM seeing in connection with wind direction at Paranal between 10 April 2005 and 30 November 2007. Wind direction frequencies in the same period are also reported. 40

4.1 Main characteristics of the Abacus TM301 dust monitor. 43
4.2 Dust background content at ORM in wintertime, summertime, and in the entire annual cycle. 45
4.3 Number of storm events at ORM in wintertime, summertime, and in the entire annual cycle in the period from August 2001 to December 2006. . . . 46
4.4 Values of the extinction efficiency factor Q_{ext}. 49
4.5 Seasonal and annual local aerosol atmospheric extinction computed in dusty background conditions. 50
4.6 Relative contribution of each particle size as percentage of the total aerosol atmospheric extinction k_{aer}. 52

5.1 ISAAC SW imaging filters used in this study. 58
5.2 Technical events occurred between 2000 and 2005. 59
5.3 κ-coefficients in different periods for J, J_S, H and K_S. 62
5.4 Weighted averaged κ-coefficients for J, J_S, H and K_S for periods and monthly cases. 62

6.1 MASS weighting functions extremes definition at Paranal. 68

7.1 Definition of the extremes of the new unified grid of layers. 74

8.1 MASS+DIMM. Typical profiles ASL for good (33%), median and bad (66%) seeing at Paranal. The statistics is made on the basis of 657 observing nights (20057 10-minutes averages) in the period between 2 January 2005 and 30 June 2007. 90

A.1 Instruments and tools used for the E-ELT site testing campaigns in each site (X if used, − if not used). 94

Chapter 1

Aims of the project

The question is not what you look at, but what you see.
Henry David Thoreau

For visible and infrared astronomy, ground-based facilities can give better performances in terms of spatial resolution and sensitivity with respect to space telescopes, at lower costs (Gilmozzi 2006). So, if you want to do frontline ground-based astronomy you need new giant telescopes giving you the best image and the best spectra possible. But having a giant telescope is not enough to reach your purposes. A big telescope on bad mountain does not allow you to obtain high quality data.

The quality of astronomical sites is the first step to be considered to have the best performances from the telescopes. In particular, the efficiency of large telescopes in UV, IR, radio etc. is critically dependent on atmospheric transparency. It is well known that telescope's performances are also limited by the random optical effects induced on the light propagation by turbulent atmosphere.

All telescopes have an inherent limitation to their angular resolution due to the diffraction of light at the telescope's aperture. For astronomical instruments, the incoming light from the space is approximately a plane wave since the source of the light is so far away that can be considered at infinite distance. In this limit, Fraunhofer diffraction occurs and the pattern projected onto the focal plane of the telescope will have little resemblance to the aperture (Lotz 2009). The goal of next generation ground-based telescopes is to reach this diffraction-limited resolution. But telescopes receive light crossing kilometers of Earth's atmosphere.

1.1 A brief history of site testing

The site testing evolved during the years according to the knowledge of the atmosphere and the technical progress in telescopes design. At the end of XIX century optical telescopes where located close to urban areas (for example the *Specola* of the Astronomical Observatory of Bologna and Padova). The economical progress and the begin of the electricity moved the astronomers far from light pollution of the cities, thus a *clear* and *dark* sky was the only (main) requirement at that time.

In the years around 1960 the concept of seeing was introduced in the sites analysis. But each astronomer assumed his/her own seeing definition, making difficult to compare the quality of different sites. For instance, astronomers published seeing values derived from Polar trails (Moroder&Righini 1973), or from diurnal measurements of solar limb (Brandt 1970), or from interferometric measurements (Roddier et al. 1978), or nighttime evaluation of image profile.
The first theory on the seeing and its connection within atmospheric physical parameters arrived between the 70's and the 80's (Ceppatelli&Righini 1973; Barletti et al. 1976; Barletti et al. 1977; Roddier 1981 and 1989). The idea to evaluate the quality of an astronomical image by measuring the maximum resolved detail, had its first standardization at the end of the 80's with the introduction of the DIMM (Differential Image Motion Monitor) seeing monitor (Sarazin&Roddier 1990). The idea was (and *is*) to predict the reachable optical quality of large telescopes analysing the image obtained using small telescopes.
Nowadays, clear appears the importance to correlate the main atmospheric physical parameters with the optical quality reachable by large aperture telescopes. The sky quality evaluation improved with the introduction of new techniques, new instrumentations and with the understanding of the link between the meteorological (or synoptical) parameters and the observational conditions thanks to the application of the theories of electromagnetic waves propagation in turbulent medias: what we actually call *astroclimatology*.
At the present the site campaigns are evolved and are performed using the classical scheme of optical seeing properties, meteorological parameters, sky transparency, sky darkness and cloudiness. New concept are added and are related to the geophysical properties such as seismicity, microseismicity, local variability of the climate, atmospheric conditions related to the ground optical turbulence and ground wind regimes, aerosol presence, use of satellite data (Sarazin 1992; Muñoz-Tuñón et al 1998; Jabiri et al. 2000; Sarazin 2004; Lombardi et al. 2006, 2007, 2008a and 2008b; Sarazin 2008).

1.2 The development of the project

The purpose of this project is to provide reliable methods to analyze the atmospheric properties that affect ground-based optical astronomical observations and to correlate them with the main atmospheric parameters generating turbulence and affecting the photometric accuracy.
The first part of the thesis is developed using the existing databases from classical data source:

- data compilation: collection of the data (mainly ground-based) using meteorologiacal stations, satellites, new ad hoc measurements, seeing monitors, turbulence profilers
- data reduction: using different methods of analysis, chosen on the basis of the available data; it is important to use the same statistics when comparing different sites, in order to obtain reliable results and extrapolate the most coherent conclusions
- results interpretation and their comparison with similar studies, if available

The second part of the project taken place *in situ*. In fact part of this PhD research has been developed using several turbulence profilers in the selection of the site for the European Extremely Large Telescope (E-ELT). During the campaigns the properties of the turbulence at different heights at Paranal and in the sites located in northern Chile and

Argentina have been studied. This given the possibility to characterize the surface layer turbulence at Paranal and its connection with local meteorological conditions.

The work realized during this PhD produced some refereed papers and contribute talks at astronomical meetings. Actually, I am involved as ESO staff in Chile in a collaboration with international teams, as expert in the use of several complementary instruments designed to measure the distribution of the turbulence in the atmosphere with the aim to select the site for the E-ELT.

The thesis is organized as follows:

Chapter 2: the structure of the atmosphere of the Earth, the atmospheric turbulence theory and the general parameters responsable of the loss in spatial resolution of an optical telescope are described

Chapter 3: the astroclimatological comparison of the Paranal Observatory and the Observatorio del Roque de Los Muchachos (ORM) is shown

Chapter 4: the aeresol extinction at ORM is calculated using a ground-based dust counter and satellites data

Chapter 5: the near-IR atmospheric extinction at Paranal is investigated using existing telescope data from the Unit Telescope 1 (UT1) calibration plan

Chapter 6: the turbulence profilers used in this project are described (DIMM, MASS, SLODAR)

Chapter 7: we show a complete new technique implemented to combine turbulence profiles from MASS and SLODAR

Chapter 8: using the recombination of MASS and SLODAR we study of the evolution of the seeing at Paranal proposing our theory to justify the discrepancy between the Very Large Telescopes (VLT) image quality and the DIMM seeing

Appendix A: the E-ELT site testing and my personal participation and role played in the investigation are described

Chapter 2

Sky quality

Abstract

The structure of the Earth's atmosphere, the theory of the atmospheric turbulence and the general parameters responsable of the loss in spatial resolution of an optical telescope are described in the present Chapter.

2.1 Introduction

The Earth's atmosphere is a dynamic mixture of gases that envelops the planet in structured layers. The gases have a significant impact on the heat budget and the availability of moisture across the Earth. Local instabilities of temperature, pressure, and thus wind regimes, generate local variations of the index of refraction in each layer.
The loss in resolution is not only caused by the action of the atmosphere but this the global result of the imprecisions of the telescope optics and mechanics together with the effect of the atmospheric turbulence. Nowadays, active optics systems permit to solve the image degradation due to the optics, but still remains the degradation due to the atmosphere action. For these reasons, is imperative to well know the characteristics of the atmospheric conditions of a considered site when hosting a new telescope.

2.2 A brief introduction to the structure of the Earth's atmosphere

2.2.1 Chemical composition

The chemical composition of dry air is roughly (by volume) 78% nitrogen, 20% oxygen, 1% argon, $< 0.1\%$ carbon dioxide, and trace amounts of other gases. Air also contains a variable amount of water vapor, on average around 1%. For semplicity we refer to the *standard atmosphere* which characteristics are:

- Standard temperature: $T_0 = 0$ °C
- Standard pressure: $P_0 = 760$ mm/Hg $= 1013.246$ hPa

- Standard gravity: $g_0 = 9.80665$ m s^{-2}
- Standard density: $\rho_0 = 1.293 \cdot 10^{-3}$ g cm^{-3}
- Median molecular mass: $m = 4.810 \cdot 10^{-23}$ g

In first approximation the Earth's atmosphere is in radiative equilibrium with its surroundings and the average structures are characterized by temperature and density distribution.

2.2.2 Thermal structure

Only adiabatic processes take place in the atmosphere. UV rays are absorbed of about 5%, while there is a discrete transparency in the visible. The radiation absorption is followed by a black body emission at 280 K having a peak at 12-13 μm. This emission is absorbed by the atmospheric gases (prevalently in the H_2O and CO_2 bands), and generates an increase of temperature in the troposphere. This is the reason why the temperature decreases while 'climbing' mountains, going far from sea level.
The dry vertical adiabatic lapse rate is the negative of the rate at which a rising parcel of dry or unsaturated air changes temperature with increasing height, under adiabatic conditions, and its value is -1.0°C/100 m. The wet vertical adiabatic lapse rate takes into account the non negligible H_2O content in the atmosphere not behaving as an ideal gas. Its value is -0.6°C/100 m up to 10^4 m in the troposphere.
The atmosphere is characterized by several *thermal inversion layers* distributed in altitudes: the usual temperature gradient – warm air below cold air – is reversed, preventing the mixing of warm and cold air as the warmer air rises. The main known inversion layer is typically located between 1 and 2 km above the sea level. This traps dangerous concentrations of pollutants in the cool air below, sometimes causing dense smog over urban areas. To prevent degradation of astronomical observations, nowadays all astronomical observatories are built well above this layer.

2.2.3 Atmospheric layers

A schematic representation of the structure of the atmosphere is shown in Figure 2.1. The troposphere is the atmospheric layer closest to the planet and contains the largest percentage (around 80%) of the mass of the total atmosphere. Temperature and water vapor content in the troposphere decrease rapidly with altitude. The optical band is strongly influenced by the presence of this structure. The troposphere contains 99% of the water vapor in the atmosphere. In this layer vigorous convective air currents are present within the layer. The tropopause ranges in height from 8 km near the poles up to 18 km above the equator. Its height also varies with the seasons; highest in the summer and lowest in the winter.
The stratosphere extends above the tropopause to an altitude of about 50 km above the planet's surface. Ozone plays the major role in regulating the thermal regime of the stratosphere, as water vapor content within the layer is very low. Temperature increases with ozone concentration. Solar energy is converted to kinetic energy when ozone molecules absorb ultraviolet radiation, resulting in heating of the stratosphere. The ozone layer is

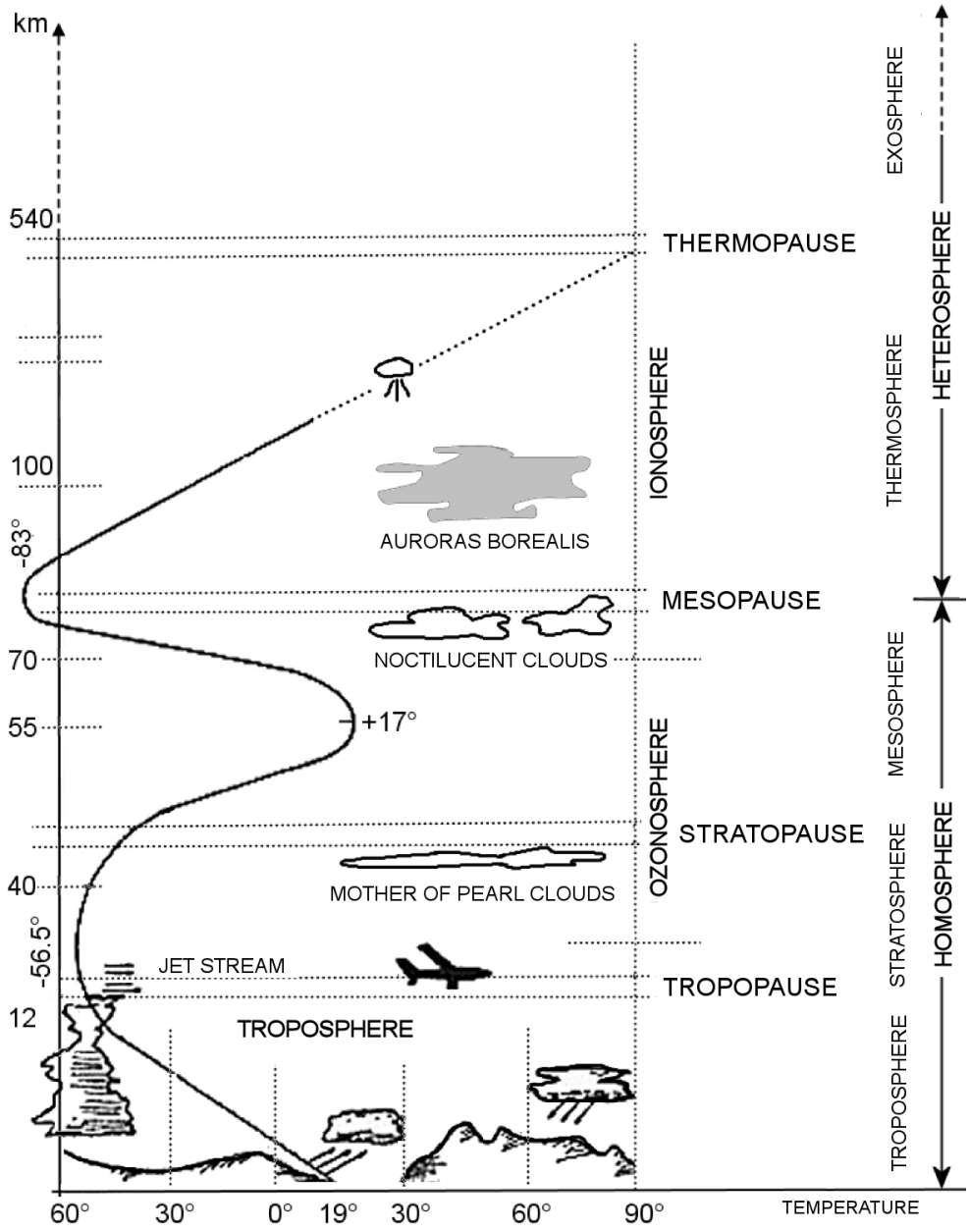

Figure 2.1: *Atmospheric layers. Note the temperature trend in altitude.*

centered at an altitude between 15-25 km. Approximately 90% of the ozone in the atmosphere resides in the stratosphere. It absorbs the bulk of solar ultraviolet radiation in wavelengths in the range 290-320 nm (UV-B radiation). The strongest night sky emission lines such as the 5577A and OH bands are formed in this region.

The mesosphere extends from approximately 50 to 90 km above the surface, is characterized by decreasing temperatures. Here resides a thin sodium layer useful to generate the sodium line at 5893A used by Laser Guide Star adaptive optics technique. The strength of the line varies with the season: ∼30 Rayleight in summer to ∼180 in winter (Allen 2000).

The thermosphere is located above the mesosphere. The temperature in the thermosphere generally increases with altitude. In this layer are produced the strong night sky emission lines of the oxygen at 6300A and 6363A. Finally, above 1000 km in height, the atmosphere is dominated by the presence of atomic H.

2.2.4 Absorption and emission

The absorption and radiation by the constituent of the atmosphere can be either total or partial. In case of partial absorption, the source spectra is modified by telluric bands. The unabsorbed radiation wavelenghts constitute the *transmission window*. Quantitatively, millimeter bands are dominated by rotational band of H_2O and CO_2.
Emission lines can be fluorescent and thermal. An example of fluorescent emission is the air glow. It is caused by various processes in the upper atmosphere, such as the recombination of ions which were photoionized by the Sun during the day, luminescence caused by cosmic rays striking the upper atmosphere, and chemiluminescence caused mainly by oxygen and nitrogen reacting with hydroxyl ions at heights of a few hundred kilometers. It is not noticeable during the daytime because of the scattered light from the Sun.
As pointed in Section 2.2.2, the radiation absorption by the Earth is followed by a black body emission at 280 K having a peak at 12-13 μm. The emission is absorbed by the H_2O and CO_2 bands, thus to minimize the thermal sky emission an appropriate choice of the site is imperative for IR and mm observations.

2.3 The concept of seeing

The Point Spread Function (PSF) is a function describing the light distribution on the focal plane of the telescope. Having a point-like source (such as a star), a perfect instrument does not produce point-like images: the diffraction of the light generated by the entrance pupil of the telescope produce an infinite number of concentric dark and clear annuluses which intensity decrease within the distance from the center (*Airy annuluses*). Thus, the resolving power of a telescope, defined as the smallest resolved detail, is

$$\theta \propto \frac{\lambda}{D} \tag{2.1}$$

where λ is the observed wavelenght and D the diameter of the entrance pupil of the telescope. The previous formula represent the theoric angular resolution θ in [rad] also known as *Airy disc*. During astronomical observation this theoretical limit can never be reached. The turbulence distorts erratically the diffraction figure and modifies the light distribution on the focal plane, so the PSF becomes larger and have an approximately gaussian profile. The atmosphere is affected by the diurnal heating of the Sun, in particular the lower layers undertake the heating originated by the emission of the ground. The heating is not homogeneous because of the presence of condensation, evaporation, pressure fluctuations and convective cells. The presence of irregularities of the index of refraction in the atmosphere generates a continuous variation in the wavefront direction (see Figure 2.2). These irregularities are mainly due to thermal inhomogeneities that can arise in many ways depending on the region of atmosphere under consideration. At ground level seeing effects can be produced by radiation cooling or by heating of the terrestrial surface, at intermediate level the main effect is due to the arrival of frontal wind systems that disrupt the homogeneity of the layer, even the lower atmosphere may remain still undisturbed.

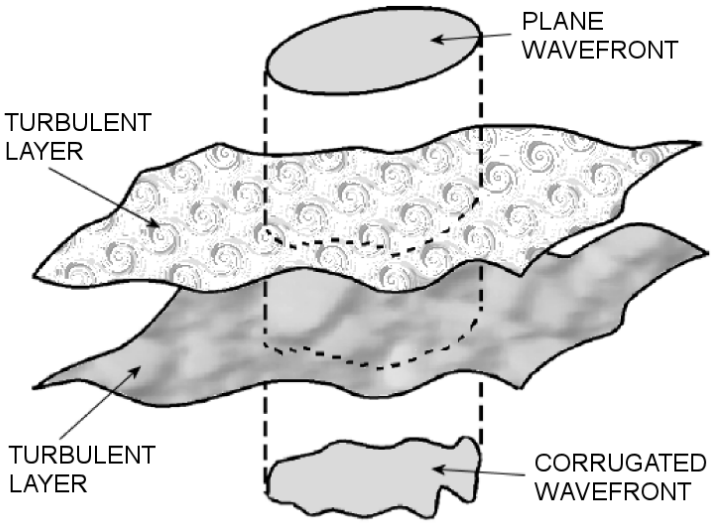

Figure 2.2: *A schematic example of a plane wavefront perturbation by two turbulent layers.*

To quantify the concept, we define the seeing as *the Full Width at Half Maximum (FWHM) of the Point Spread Function of a stellar source (point-like light)*, and is measured in [arcsec]. A *good* seeing is between 0.2 and 0.5 arcsec, while normal values vary between 0.6 and 1.0 arcsec. Beyond 1.0 arcsec the seeing is considered *bad*, in the sense that the image quality is too much affected.
We can distinguish different zones contributing to the total seeing (see Figure 2.3):

- *mirror seeing*: it forms close to the telescope primary mirror and is due to the thermal gradient between the mirror and the surrounding area; this contribution can be eliminated thermalizing the mirror at a temperature that minimize the median gradient

- *dome seeing*: it generates inside the telescope dome and is due to thermal gradients between the inner and the external area; the situation can be improved with a good ventilation of the dome (Zago 1995) in order to avoid the formation if convective cells inside the dome

- *ground layer*: now we know that this is typically the strongest contribution to the total seeing; it is due to a superficial inversion layer caused by the diurnal ground heating which consequent emission generates local convective cells

- *planetary boundary layer*: this layer extents up to 10^3 m in plain zones and stays below the main inversion layer; the diurnal effect of the Sun generates convective cells transported by ascending and descending currents that are blocked by the atmospheric main inversion layer; for these reasons all modern astronomical observatories are located well above the inversion layer

- *free atmosphere*: this contribution comes from the strong convective currents present in the troposphere up to 25 km; above this limit further contributions to the seeing are negligible

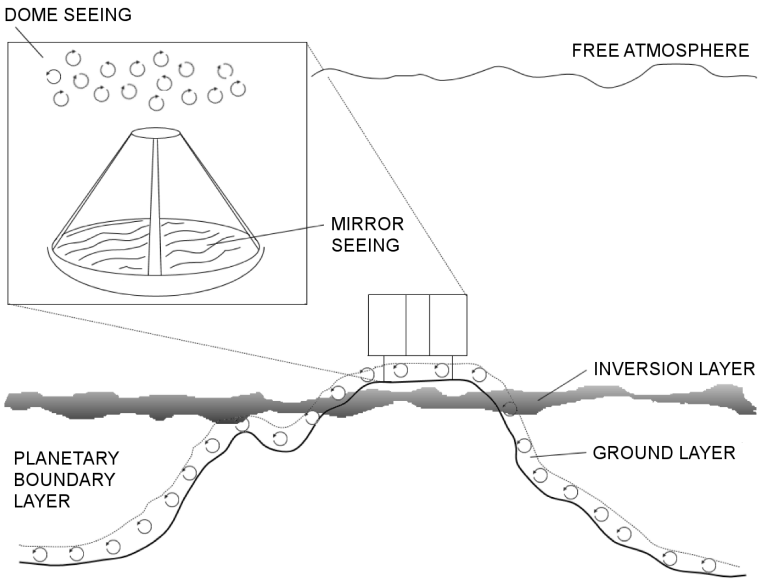

Figure 2.3: *Different kinds of seeing contributions.*

2.4 Statistics of the atmospheric turbulence

As already mentioned, the Earth's atmosphere is a dynamic mixture of gases that envelops the planet. So, the dynamics of the atmosphere is linked to the dynamics of the fluids. A fluid can be transported in *laminar* or *turbulent* regime. In the laminar regime the points of the fluid characterized by the same velocity v are distributed on a surface flowing between the adjacent ones having velocities $v + dv$ and $v - dv$, without mixing. The velocity vectors of the points forming the laminate are parallels and constants, thus the velocity gradient is perpendicular to the laminates.
The turbulent regime is characterized by the formation of vortexes which initial kinetic energy dissipates by a cascade process to minor vortexes (see Figure 2.5). When the turbulence energy is equivalent to the one dissipated at microscopic scale, the vortexes decade continuously to smaller dimensions until they dissipate in molecular motion below a critic scale depending on the kinematic viscosity of the fluid ν [m^2 s], its velocity V [m s^{-1}] and L [m], defined as *outer scale* (i.e. the diameter of a tube in which the fluid is flowing, the dimension of an obstacle obstructing the fluid motion or the thickness of an atmospheric layer).

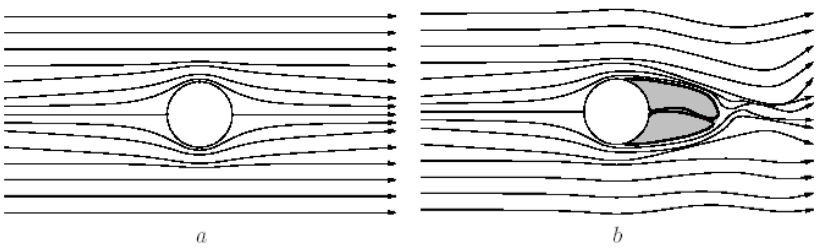

Figure 2.4: *(a) laminar motion around an obstacle; b) formation of a turbulent motion around the same obstacle.*

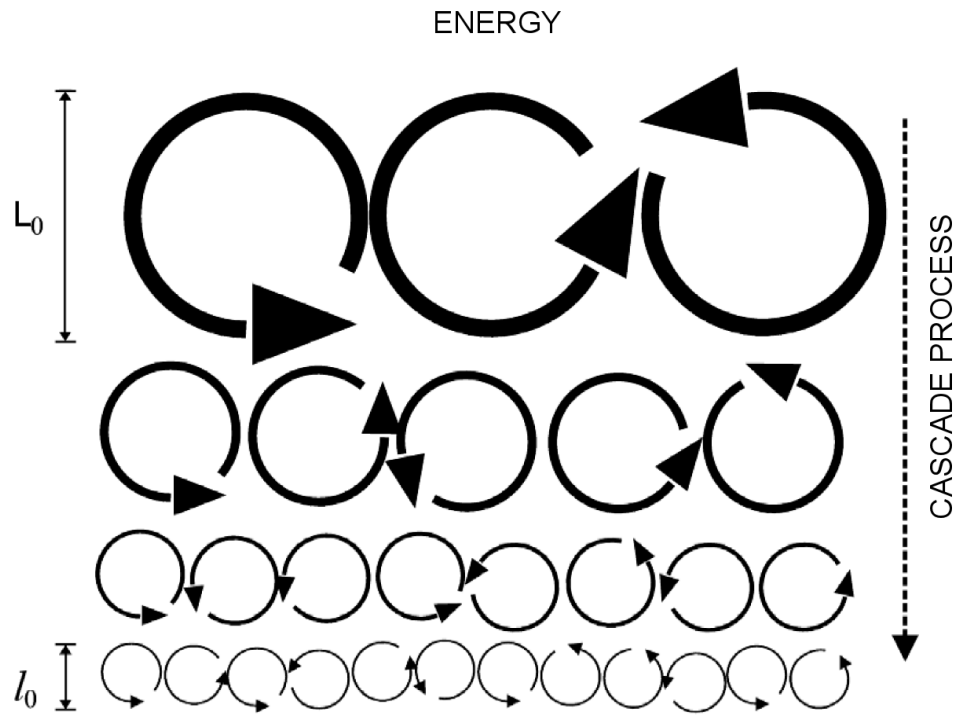

Figure 2.5: *Development of a turbulent regime in a cascade process: the scale decreases down to molecular motion.*

Turbulence sets-in when the inertial forces (ρV) are much larger than the shear forces due to viscosity (μL). The ratio of these two forces is the Reynolds number (Re, dimensionless) defined as

$$Re = \frac{\rho V}{\mu L} = \frac{VL}{\nu} > 2000 \tag{2.2}$$

where ρ is the density and μ the dynamic viscosity of the fluid (thus $\nu = \mu/\rho$). Typically in the atmosphere $\nu \simeq 10^{-6}$ m^2 s, $V \simeq 10$ m s^{-2} and $L \sim 10 - 20$ m, so $Re \approx 10^5$, thus the turbulence is completely developed.

In typical conditions in the Earth's atmosphere viscous forces are negligible compared to buoyancy forces generated by gravity and heat. Therefore turbulence sets-in when the inertial forces are larger than the buoyancy. The Richardson number Ri is defined as the ratio between these forces

$$Ri = \frac{\text{buoyancy force}}{\text{inertial force}} = \frac{gh}{V^2} \tag{2.3}$$

In the atmosphere the heat is transported vertically, and the density, pressure, temperature, humidity and velocity vary with h. From Stull (1988) we know that the Ri below which inertial stresses dominate over buoyancy forces is 0.25, thus the flow is unstable to turbulence when $Ri < 0.25$. Stull points that, because there is hysteresis, stability is regain after turbulence if $Ri > 1$.

The effects of the turbulence on electromagnetic waves are erratic fluctuations of amplitude and phase. Due to the aleatoric properties of the turbulent phenomenon, their statistical analysis becomes necessary. The first description of the nature of the wavefront perturbations introduced by the atmosphere is provided by the Kolmogorov model developed by Tatarskii (1961), based partly on the studies of turbulence by the Russian mathematician Andrei Kolmogorov (Kolmogorov 1941). This model is widely used in simulations of astronomical imaging.
In his study, Kolmogorov established that the energy of the turbulence is introduced in the vortexes in correspondence of an outer scale L_0 (Figure 2.5). From this scale the motion is transferred to smaller vortexes without loosing energy. The process evolve to vortexes even smaller until they reach a dimension l_0 (*inner scale*) and the turbulence stops. At this point Re is lower than the critical value and the energy is dissipated by viscosity friction between molecules. The interval $[l_0,\ L_0]$ is called *inertial interval*, in the sense that the energy transfer is due to the fluid inertia and the turbulence is homogeneous and isotropic. In order to let the turbulence to not stop and maintain a cell of diameter l_0 at velocity V, an energy per mass unit (ε) contribution is necessary

$$\varepsilon \simeq \frac{V^3}{l} \tag{2.4}$$

from which we derive the Kolmogorov formula

$$V \simeq (\varepsilon l)^{1/3} \tag{2.5}$$

From Hardy (1990) we know that the ratio L_0 to l_0 is

$$L_0/l_0 \simeq (Re)^{3/4} \tag{2.6}$$

Tatatrskii (1961) affirms that erratic fluctuations of the index of refraction n due to the turbulence can be produced only in presence of a component related to heat, pressure and humidity. This term acts as a trigger and it is possible to characterize the turbulence referring to it.
The phase fluctuations in Tatarskii's model are usually assumed to have a gaussian random distribution with the following second order structure function

$$D_\varphi(\vec{r}) = \langle |\varphi(\vec{r}+\vec{x}) - \varphi(\vec{r})|^2 \rangle_{\vec{r}} \tag{2.7}$$

where $D_\varphi(\vec{r})$ is the variance induced by the atmosphere between the phase at two parts of the wavefront separated by a distance $\vec{r}$ in the aperture plane.
In the inertial interval the fluid flux is regulated by the scale L and the energy dissipation rate $d\varepsilon/dt$, so that

$$D_\varphi(\vec{r}) \propto (\varepsilon r)^{\frac{2}{3}} \tag{2.8}$$

The proportionality is expressed by a *structure constant* for each considered variable linked to the turbulent motion (the velocity V, the temperature T and n).
The structure function of the velocity is

$$D_V(\vec{r}) = C_V^2 r^{\frac{2}{3}} \tag{2.9}$$

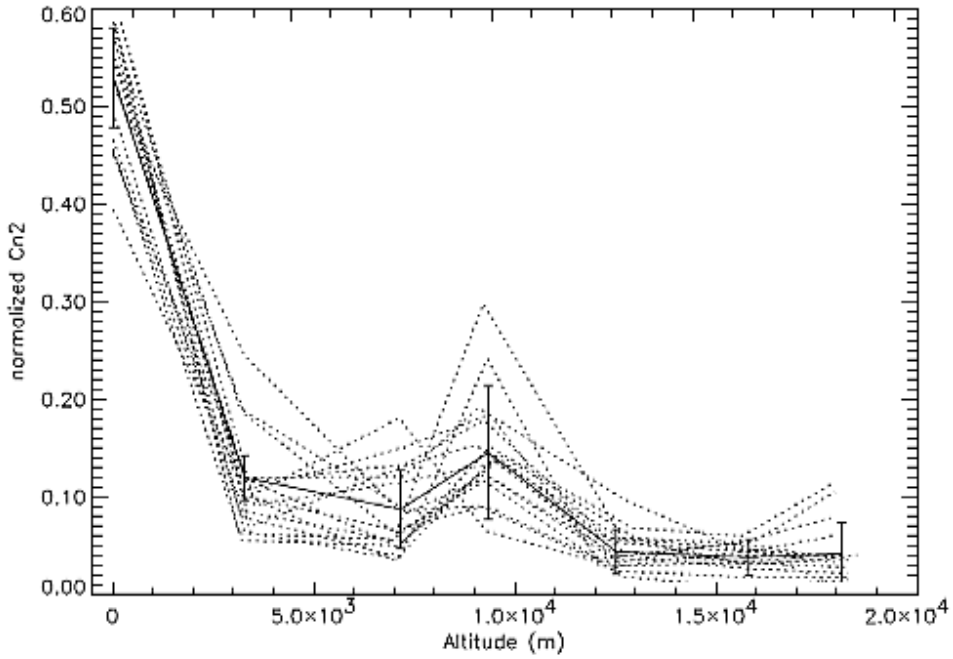

Figure 2.6: *C_n^2 profiles measured at San Pedro–Martir (Mexico) on 16 March 2000 (Le Roux 2003).*

while the structure function of the temperature is

$$D_T(\vec{r}) = C_T^2 r^{\frac{2}{3}} \tag{2.10}$$

C_V^2 depends on the energy of the process while T fluctuations affect the air density and produce fluctuations of n.
As already mentioned, the index of refraction depends on the temperature, the pressure and the relative humidity, the latter having a negligible influence with respect to the others. In this case the structure function of the index of refraction is

$$D_n(\vec{r}) = C_n^2 r^{\frac{2}{3}} \tag{2.11}$$

where $C_n \approx (\Delta P/\Delta T)C_T$ defines the *structure constant of the index of refraction* measured in [$m^{2/3}$]. Although it is called *constant*, C_n^2 is not constant at all, in fact it varies within the altitude and in time. C_n^2 express the strength of the turbulence, since it is related to the turbulence energy. Typically, it is 10^{-14} $m^{2/3}$ at the ground and 10^{-17} $m^{2/3}$ in the free atmosphere (Tatarskii 1961).
The atmospheric turbulence tends to decrease within the altitude, but it presents peaks of high intensity in connection with each thermal inversion layer (an example is reported in Figure 2.6).
C_n^2 is linked to the turbulence spectrum by the so called *−5/3 Kolmogorov law* that in the unidimensional case is

$$\Phi(\vec{r}) = C_n^2 r^{-\frac{5}{3}} \tag{2.12}$$

while in the tridimensional case it is defined as

$$\Phi(\vec{r}) = C_n^2 r^{-\frac{11}{3}}. \tag{2.13}$$

The structure function of Tatarskii (1961) can be described in terms of a single parameter r_0 (*Fried parameter* or *Fried radius*; Fried 1966a and 1966b)

$$D_\varphi(\vec{r}) = 6.88 \left[\frac{r}{r_0}\right]^{\frac{5}{3}} \tag{2.14}$$

The Fried parameter is a *coherent length* for the atmosphere and indicates the strength of the phase fluctuations as it corresponds to the diameter of a circular telescope aperture non perturbed by the turbulence and having the same resolution of the perturbed telescope used for the observations. In good astronomical sites r_0 can vary between 10 and 40 cm.
Defining h an arbitrary altitude in the troposphere, the Fried parameter is linked to $C_n^2(h)$ by the formula (Roddier 1981 and 1989)

$$r_0 = \left[0.423 r^2 \sec\zeta \int_{h_m}^{h_M} C_n^2(h) dh\right]^{\frac{3}{5}} \tag{2.15}$$

from which we obtain that

$$r_0 \propto \lambda^{\frac{6}{5}} \tag{2.16}$$

In long exposure images with telescopes having diameter $D \geq r_0$, the FWHM is proportional to λ/r_0, that means

$$FWHM \propto \lambda^{-\frac{1}{5}} \tag{2.17}$$

Equation 2.17 shows that r_0 describes the seeing, in fact

$$\epsilon_{FWHM} = 0.98 \left[\frac{\lambda}{r_0(\lambda)}\right] \tag{2.18}$$

2.5 Coherence time

Information on the cells size and on the scale of motions in the layer is often needed. As suggested by Taylor (1938), when the turbulent cells evolve in a time scale longer than the time it is measured, the turbulence might be considered to be frozen. Thus, the wind speed could be used to translate turbulence measurements as a function of time to their corresponding measurements in space (Stull 1988).
Because of the wind of velocity v, the wavefront moves perpendicularly to the line of sight of the telescope maintaining the same shape. The time in which the perturbation pass

through the coherence cell of dimension r_0 is defined as *coherence time* (τ_0)

$$\tau_0 = -\frac{r_0}{v} \tag{2.19}$$

Inside τ_0 the turbulence in the cell does not vary more than 1 rad^2. The structure function of Tatarskii (1961) can be described in terms of τ_0 as

$$D_\varphi(\tau) = 6.88 \left[\frac{\tau}{\tau_0}\right]^{\frac{5}{3}} \tag{2.20}$$

2.6 Isoplanatic angle

Consider two different source in the sky separated by an angle θ. The wavefronts from the two sources cross different portion of atmosphere, thus are affected by different turbulence. We define the critical angle θ_{iso} (*isoplanatic angle*) corresponding to the maximum angular separation of two different sources beyond which they lose spatial coherence.
Being H the altitude of the turbulence, we have

$$\theta_{iso} \simeq 0.314\frac{r_0}{H} \tag{2.21}$$

Typical values for θ_{iso} are 1-2 arcsec in V, while in the IR it is

$$\theta_{iso} \propto \lambda^{\frac{6}{5}} \tag{2.22}$$

2.7 The Strehl Ratio

The Strehl Ratio (SR) is a dimensionless parameter quantifying the quality of an optical system affected by turbulence. It is defined by the ratio of the peak of the PSF of the real image (I) to peak of the PSF of the theoretical diffraction limited image (I_0)

$$SR = \frac{I}{I_0} \tag{2.23}$$

The more SR is close to 1, the better is the image quality of the optical system.

2.8 The effects of the seeing

The seeing generates different kinds of distortions of an incoming wavefront. Figure 2.7 shows some examples.
The *scintillation* is an erratical variation of the radiation intensity from a non-resolved source. This phenomenon is generated by turbulent layers in the high atmosphere.
The *tip-tilt* is a change in the wavefront slope on the telescope entrance pupil. The effect is more significant on instruments having aperture $D \ll r_0$.

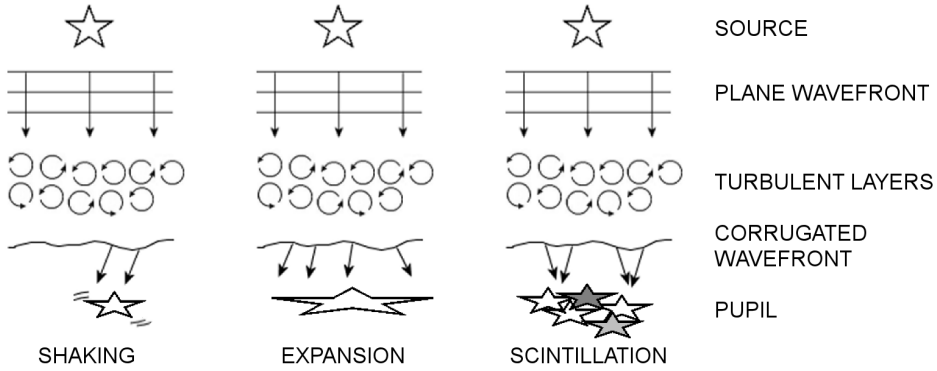

Figure 2.7: *A simple scheme of the effects of the seeing.*

In short-exposure images it is possible to detect the presence of *speckles*[1] erratically appearing and disappearing in the focal plane. The angular dimension of a speckle are in the order of $\theta \simeq \lambda/D$, while the global phenomenon is circumscribed in an area of radius $\theta \simeq \lambda/r_0$. In long-exposure images spatial coherence is lost in the pupil plane, thus the image is missing high frequency components. The result is a blurring in an area of dimension $\theta \simeq \lambda/r_0$. Finally, incident radiation at zenithal distance $\zeta \neq 0$ is decomposed in spectral components depending on λ. The result is an elongation in height proportional to ζ, furthermore the spectral components lose their correlation.

[1] A speckle pattern is a random intensity pattern produced by the mutual interference of a set of wavefronts.

Chapter 3

Astroclimatology of ground-based observatories

Abstract

This Chapter concerns the analysis and interpretation of long- and short-time scale meteorological data at two of the most important astronomical sites located in very different environments: the Paranal Observatory in the Atacama Desert (Chile), and the Observatorio del Roque de Los Muchachos (ORM) located in La Palma (Canary Islands, Spain). Important differences have been found between the two sites. In particular, we show very different relative humidity regimes (which condition the number of nights lost for moisture condensation on the instrumentation) and local wind properties (responsible of the turbulence in the surface of the observatories).

3.1 Introduction

The analysis of the astronomical and meteorological parameters in different sites are conducted, since today, using different approach. In this Thesis we want to apply for the first time the same methods to compare two different and important sites for the development of the astronomical observations: the site of Paranal Observatory located in the Atacama Desert (Chile, southern hemisphere), and the Observatorio del Roque de Los Muchachos (ORM) located at La Palma (Canary Islands, northern hemisphere). The two opposite locations have different observing characteristics not only because it is possible to see two different sky regions, but also because the oceanic currents impress different climatic regimes to the two sites. While Paranal is located in a desert area, 12 km far from the Pacific Ocean, and it is subjected to the oscillating weather variation due the presence of El Niño and La Niña events, the ORM is influenced by a semipermanent Azores high pressure system and it is influenced by the almost periodical variation of the North Atlantic Oscillation (NAO).

More than 20 years of meteorological data have been collected at Paranal and ORM. At ORM we taken data from the Carlsberg Automatic Meridian Circle (CAMC) which has the longest data sets at ORM (about 21 years), the Telescopio Nazionale Galileo (TNG) (which represent the most advanced italian facility in the site) and the Nordic Optical Telescope (NOT) meteorological stations. Results shown here have been already published in Lombardi et al. (2006) (hereafter Paper I) and Lombardi et al. (2007) (hereafter Paper II). A

Table 3.1: *Geographical positions of Paranal and telescopes at ORM. All facilities are located well above the inversion layer.*

	Latitude	Longitude	Height [m a.s.l.]	
Paranal	24° 37' 31" S	70° 24' 10" W	2636	(Platform)
TNG	28° 45' 28" N	17° 53' 38" W	2387	(Elevation Axis)
CAMC	28° 45' 36" N	17° 52' 57" W	2326	(Dome floor)
NOT	28° 45' 26" N	17° 53' 06" W	2382	(Dome floor)

detailed comparison between ORM and Paranal has been already submitted to MNRAS.
It is known that the very good astronomical conditions of the ORM are mainly due to the stable subsiding maritime airmass that place most of the time the telescopes near the top of the mountain well above the inversion layer occurring in the range between 800 m and 1200 m (McInnes&Walker 1974). All the telescopes are located along the northern edge of the Caldera de Taburiente, at the N−W side of La Palma Island, where the irregular shapes produce a complex orography and the crowdedness of the top, due to the presence of all the astronomical observatories, suggests a possible modification of the local microclimate making difficult to foresee in advance the precise local meteorological parameters. Therefore in these last years the ORM has been extensively monitored thanks to the efforts of the several site testing groups belonging to the hosted astronomical observatories (Brandt&Righini 1985; Murdin 1985).
Extensive site testing campaigns have been conducted on the top of the Paranal Observatory since years. Thanks to the excellent results, the site was chosen to host the four Very Large Telescopes (VLT) by the European Southern Observatory (ESO). This site, like La Silla, the other Chilean ESO site, have been very deeply analyzed by ESO teams. Now ESO telescopes are considered the touchstones and their characteristics are used to be compared with the other sites and the other telescopes.

3.2 Meteorological stations

Table 3.2 reports the databases characteristics. Data at ORM are taken from different locations among the observatory to check for local variations in the environmental conditions across the site. Telescopes are located on a space baseline of about 1000 m, with the NOT in the middle at 500 m from the other two telescopes. Table 3.1 reports coordinates and altitude of telescope at ORM and of Paranal.
The TNG meteo tower is a robust steel structure with a total height of 15 m. The tower is located about 100 m far from TNG building. The data are regularly sent from the tower to TNG annex building by means of an optic fiber link since 27 March 1998. The data sampling rate is 10 seconds, while data storage is done every 30 seconds.
The CAMC carried out regular meteorological observations in the period 13 May 1984 to 31 March 2005 and the records are more or less continuous in that period. For the years 1984, 1985 and 1986 meteorological readings are only available at 30 minute intervals. From January 1987 readings were made at 5 minute intervals throughout the day and night regardless of whether observing was in progress. Beginning in December 1994, all readings were made at 20 seconds intervals and then averaged over 5 minutes[1].
The NOT provides a complete archive since 2 March 1997. The data are available in regular readings done every 5 minutes[2].

[1] http://www.ast.cam.ac.uk
[2] http://www.not.iac.es

Table 3.2: *Available databases for the observatories.*

	TNG	CAMC	NOT	Paranal
Data rate	30 sec	5 min	5 min	20 min
Begin	March 1998	May 1984	March 1997	January 1985
End	December 2007	March 2005	December 2005	December 2006
Total	$\sim$ 10 yr	$\sim$ 21 yr	$\sim$ 9 yr	$\sim$ 22 yr

The Paranal Astronomical Site Monitor is located in the north area of the Paranal Observatory platform and hosts several instruments used in the characterization of the site. The Vaisala tower is a robust steel structure having a total height of 30 m. All the data are regularly collected since January 1st, 1985 and have to be intended as 20 minutes averages.

– **Air temperature (T)**
  Temperature at TNG is measured by sensor distributed along the tower at different heights (ground, 2, 5 and 10 m) and giving an accuracy of 0.1°C. The CAMC sensor is located at 10.5 m above the ground and gives an accuracy of 0.1°C. No temperature data from NOT were available. The external air temperature at Paranal is simultaneously measured at 2 and 30 m above the ground (same height of the VLT's domes) with an accuracy of ±0.2°C (Sandrock et al. 1999).

– **Air pressure (P)**
  Air pressure data at ORM are sampled with an accuray of ±0.1 hPa. The TNG sensor is placed 1 m above the ground on the meteo tower, the CAMC one is placed inside the dome, 1 m above the floor and NOT sensor is also placed inside the dome, 2 m above the floor. P at Paranal is measured at 2 m above the ground with an accuracy of ±0.1 hPa

– **Relative humidity (RH)**
  The relative humidity is the percentage of water vapour in the air with respect to the theoretical amount necessary to reach condensation at the same temperature. For the three telescopes at ORM the relative humidity sensors give an accuracy better than 2%. TNG sensor is placed 2 m above the ground on the meteo tower, while CAMC sensor was placed inside the dome until 1987 October 17 when it was moved to the outside north-facing wall of the dome; finally, NOT sensor is placed outside the dome. At Paranal the relative humidity is measured at 2 m above the ground with an accuracy of ±1% respectively.

– **Dew point (T_{DP})**
  The dew point temperature is the critical temperature at which condensation occurs. When dew point temperature and air temperature T are equal the air said to be saturated and condensation appears if the air cools. It is clear that the knowledge of the dew point temperature is crucial for the maintenance of the optics of the telescope to avoid condensation, in particular if the the instrumentation is maintained at temperatures few degrees lower than the air temperature. Condensation can be reached mostly in clear nights, when the Earth cools rapidly, therefore this parameter is relevant because in case of high value it is imposed to close the dome for safety reasons.

– **Wind vector ($\vec{V}$)**
Wind vector can be assumed as $\vec{V} = w_{sp} \cdot \vec{w}_{dir}$, where w_{sp} and $\vec{w}_{dir}$ are respectively wind speed and wind direction. The wind speed is measured in m s^{-1}, while wind direction in degrees (North is represented with 0°, East with 90°). TNG sensor is placed at the top of the meteo tower and has an accuracy better than 2% for w_{sp} and ±3° for $\vec{w}_{dir}$. CAMC sensor was placed 6 m above the ground until 1991 May 16, then it was moved 10.5 m above the ground. It has a wind speed accuracy of ±1% below 20 m s^{-1} and ±2% above 20 m s^{-1}, while wind direction is provided with a ±5° accuracy. NOT sensor has an accuracy better than 2% for w_{sp} and better than 5° for $\vec{w}_{dir}$. At Paranal wind speed and wind direction measurements are taken at 10 m above the ground with a precision of ±0.5 m s^{-1} for the wind speed and ±3° for the wind direction.

3.3 Data analysis methods

Distinguishing between *long* and *short* time scale purposes helps a lot in the definition of the parameters considered in this thesis.
The investigation on a long time scale provides information concerning the trend of the astroclimate through decades, if there are or not seasonal effects and possible links with wide-scale phenomenons (North Atlantic Oscillation, El Niño, etc.). The goal of the long time scale astroclimatological studies is to provide a possible forecast of the climate conditions of the site in a time scale comparable to the life of the telescope. In particular, the parameters directly involved in this study are:

- Air temperature
- Air pressure
- Relative humidity
- Dew point temeperature
- Wind (prevalent wind direction and speed range)
- Cloud coverage

Short time scale meteorological parameters are directly linked to the local properties of the atmosphere, thus to the turbulence and the extinction stability:

- Vertical and horizontal temperature gradients ⇒ presence of turbulent surface layer
- Local wind direction and wind speed ⇒ presence of turbulent surface layer, wavefront velocity
- High altitude wind speed ⇒ wavefront velocity, isoplanatic angle
- Vertical wind speed up to 25 km ⇒ wavefront velocity
- Altitude distribution of the turbulence energy ⇒ wavefront corrugation
- Aerosol Index (particles pollution) ⇒ extinction stability in UV

- Precipitable water vapor, molecules ⇒ extinction stability in IR, sub-mm etc.

- Pressure and temperature fluctuations ⇒ instruments thermalization

From each raw data series of T, P and RH we compute the hourly averages and then from each set of them we compute the monthly averages. This is useful to reduce the short−time fluctuations due to natural day/night cycle.
A particular care was used to minimize any effect due to biases in case of lacking of data that typically occurred in winter time. For each missing month value we take into account the average obtained from the two corresponding months in other years in which the values of the months before and after the absent one are similar. For example, if the lacking month is September 2002, we look for the two Augusts and Octobers in the other years having similar mean values of August and October 2002. The accepted September 2002 value is the average of the Septembers corresponding to the chosen Augusts and Octobers. Finally, we computed the annual averages of T from the monthly ones for the three telescopes.
Wind vector has been analyzed considering its daytime and nighttime behaviour. Daytime data have been defined in the range 10:00−16:00 (local time), while nighttime data in the range 22:00−4:00 (local time). From each raw data series of w_{sp} and $\vec{w}_{dir}$ we computed the hourly averages.
From each set of wind speed hourly averages, we computed the monthly averages and then the annual averages for both daytime and nighttime.
Daytime and nighttime wind direction statistics have been evaluated by calculating the annual percentage of hours in which the wind come from each direction $\vec{D}$. The wind rose has been divided into 8 mean directions (N, NE, E, SE, S, SW, W, NW) and the percentages of hours are calculated into intervals defined as $[\vec{D} - 22.5°, \vec{D} + 22.5°[$.
RH and T_{DP} statistics in daytime and nighttime have been also considered. Entire day (00:00−24:00; local time) statistics have been calculated too. CAMC data for P, RH and T_{DP} are used to compare ORM to Paranal. This is because CAMC data at ORM have a time baseline data archive comparable to the one of Paranal.

Table 3.3: *Mean annual temperatures at Paranal, CAMC and TNG [°C].*

Year	1985	1986	1987	1988	1989	1990	1991	1992
T_{PAR}	12.2	12.7	–	12.8	11.9	12.2	–	–
T_{CAMC}	8.8	8.9	9.1	7.4	5.2	8.8	8.7	7.9
T_{TNG}	–	–	–	–	–	–	–	–
Year	1993	1994	1995	1996	1997	1998	1999	2000
T_{PAR}	12.8	13.2	13.1	12.5	13.1	12.9	12.3	12.0
T_{CAMC}	7.0	9.8	9.5	8.6	8.9	10.0	9.3	9.6
T_{TNG}	–	–	–	–	10.1	9.6	9.9	
Year	2001	2002	2003	2004	2005	2006	2007	Avrg.
T_{PAR}	12.8	12.8	13.6	12.9	13.0	13.6	–	12.8
T_{CAMC}	10.1	9.6	9.8	9.0	–	–	–	8.8
T_{TNG}	10.7	9.7	9.7	8.9	9.5	10.0	9.6	–

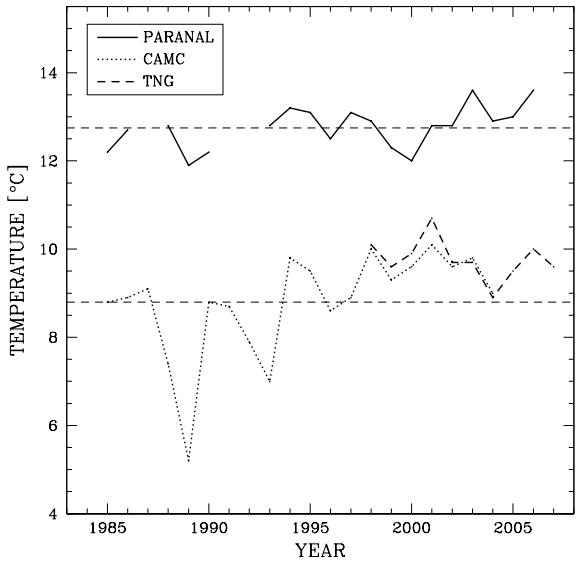

Figure 3.1: *Annual temperatures at Paranal (solid line), CAMC (dotted line) and TNG (thick dashed line). The short-dashed lines indicate the total averages: 12.8° C at Paranal and 8.8° C at CAMC.*

3.4 Air temperature

For TNG we chose to use the 10 m temperature (T_{TNG} hereafter) because corresponds to the height of the primary mirror inside the TNG dome.
The Paranal temperature is taken at two different level, at 2 and 30 m above the ground. The vertical variation of temperature with the altitude (wet and dry adiabatic lapse rate) is between 6.0 and 10.0°C/km (Kittel&Kroemer 1980), so we expect a $\sim 0.2 - 0.3$ °C difference in temperature between the two sensors at 2 and 30 m. The mean difference of the temperature taken at the two heights is 0.2°C, that is comparable with the accuracy of the sensor. For this reason we decide to use the 22 years long database at 2 m as representative of the temperature at Paranal (T_{PAR}). Table 3.3 reports the annual T at Paranal, CAMC (T_{CAMC}) and TNG. Values reported in Table 3.3 are plotted in Figure 3.1.
We measured a samples of instantaneous temperatures differences of simultaneous data from CAMC and TNG, in the months of March 2004, August 2004, November 2004 and January 2005, in order to estimate an upper limit in the errors of the computed annual values. We found a RMS range between 0.1 and 0.5°C. Comparing the instrumental accuracy of 0.1°C we see a good agreement between the two instruments and we can assume that the residual difference is due to atmospherical local variation.
The data from the CAMC and TNG are remarkably similar, with average temperatures differing no more than 0.6°C (year 2001). We note an oscillation of the CAMC values with a period of about 3−4 years that seems to be slightly smoothed during the last 10 years. Another evidence is that in the oscillation the points of local minimum and local maximum have a different behaviour, in fact the minimums increase more rapidly then the maximums. Trends at Paranal and CAMC show a positive slope during the years, while TNG data have a flat trend. The best linear fit of CAMC data gives an increase of the temperatures of about 1.0°C/10yrs, while the slope computed for Paranal gives a value of 0.4°C/10yrs. This is not

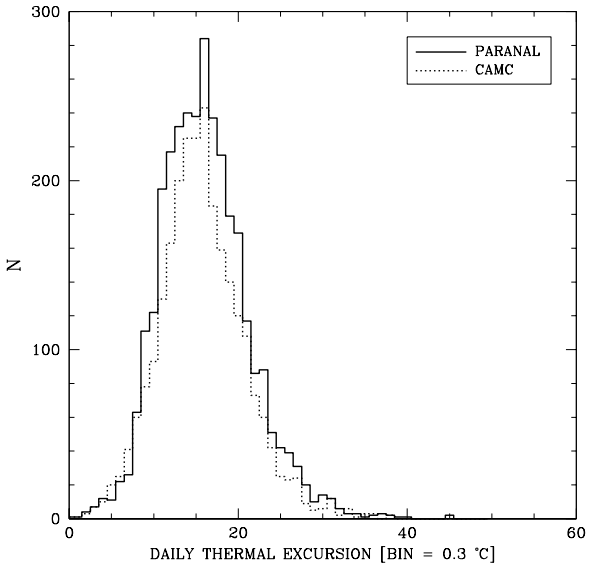

Figure 3.2: *Thermal excursion distribution at Paranal (solid line) and CAMC (dotted line) after 1998. The two sites are almost equivalent.*

surprising considering that the global warming and the glacier retreat are less pronounced in South America. To facilitate the comparison, it is also drown the total average for Paranal and CAMC (thin dashed line).

But it is interesting to note that after 1998 data at TNG seem to indicate a flattening of the increasing temperature trend. This rises the question if we are in presence of a global warming or it is a typical temperature oscillation through decades and/or a regional effect. The 22 years long baseline of Paranal is characterized by an increasing trend, the linear regression of Paranal data in the period 1993-2000 shows a slope of -0.12 while data in the period 2000-2006 have an opposite slope slightly steeper (0.19). This suggests a possible correlation with the occurrence of wide-scale climatological events such as El Niño and La Niña phenomenons (see Sections 3.6 and 3.7). In fact, a preliminary check has shown the presence of strong La Niña episodes in 1999 and 2000 that are linked to the coldest annual temperatures at Paranal (see Section 3.7). This confirms the strong link between air and ocean temperature that may influences the high level of the atmosphere.

The year 1989 appears to be the coldest for both sites in the last 20 years. The year 2001 is the warmest for CAMC while the 2003 and 2006 are the warmest for Paranal. The typical $3-4$ years oscillation of the temperatures at CAMC is not so clear for Paranal.

An interesting results comes from the analysis of the daily thermal excursion after 1998 in the two sites. In fact looking at Figure 3.2 we do see a very similar distribution for both sites with a peak at bin number 18, corresponing to a thermal excursion of about 4.8°C.

3.5 Air pressure

3.5.1 Long time scale air pressure

Figure 3.3 shows the annual mean pressure P calculated at Paranal and CAMC. Table 3.4 reports the values plotted in the figure. The average pressure at Paranal during the entire

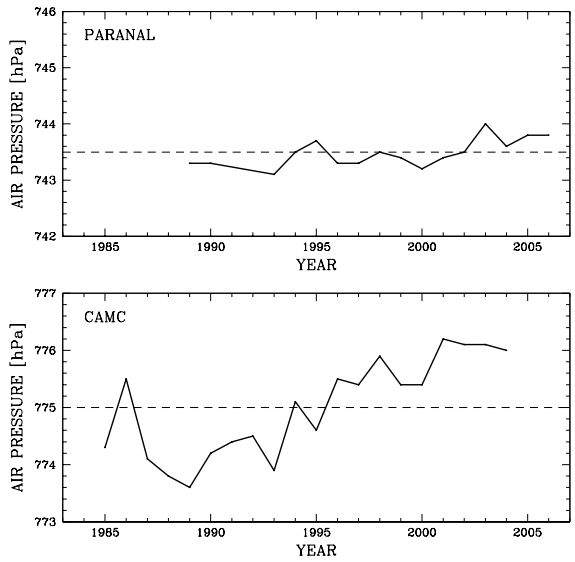

Figure 3.3: *Top: annual P at Paranal Observatory. Bottom: annual P at CAMC.*

baseline is 743.5 hPa, while the average pressure at CAMC is 775.0 hPa. The plot shows two different behaviors at Paranal with a changing of slope in the year 2000. Splitting the fit in two subsamples we see that the best fit of the points before the 2000 is almost flat with a mean value of 743.4 hPa. The best fit after the year 2000 is characterized by a positive slope of about 0.1 and the mean pressure is 743.5 hPa. This difference is comparable to the accuracy of the measuring instruments. A more detailed analysis is needed to check if this is a long term increasing trend of pressure. The data obtained from CAMC show a similar increasing trend during the years (∼1.5 hPa).

The minimum pressure measured at Paranal was 728 hPa in September 1989, while the highest one was in April 1998 with a value of 754 hPa. Instead, CAMC minimum pressure was 747.7 hPa in September 2004, while the maximum was 785.8 hPa in July 2001.

Two interesting plots are shown in Figure 3.4, where the monthly P and T averages in the two sites are plotted. There is a clear decreasing of the dispersion of the monthly P

Table 3.4: *Mean annual air pressure at Paranal and CAMC [hPa].*

Year	1985	1986	1987	1988	1989	1990
Paranal	–	–	–	–	743.3	743.3
CAMC	774.3	775.5	774.1	773.8	773.6	774.2
Year	1991	1992	1993	1994	1995	1996
Paranal	–	–	743.1	743.5	743.7	743.3
CAMC	774.4	774.5	773.9	775.1	774.6	775.5
Year	1997	1998	1999	2000	2001	2002
Paranal	743.3	743.5	743.5	743.2	743.4	743.5
CAMC	775.4	775.9	775.4	775.4	776.2	776.1
Year	2003	2004	2005	2006	Avrg.	
Paranal	743.0	743.6	743.8	743.8	743.5	
CAMC	776.1	776.0	–	–	775.0	

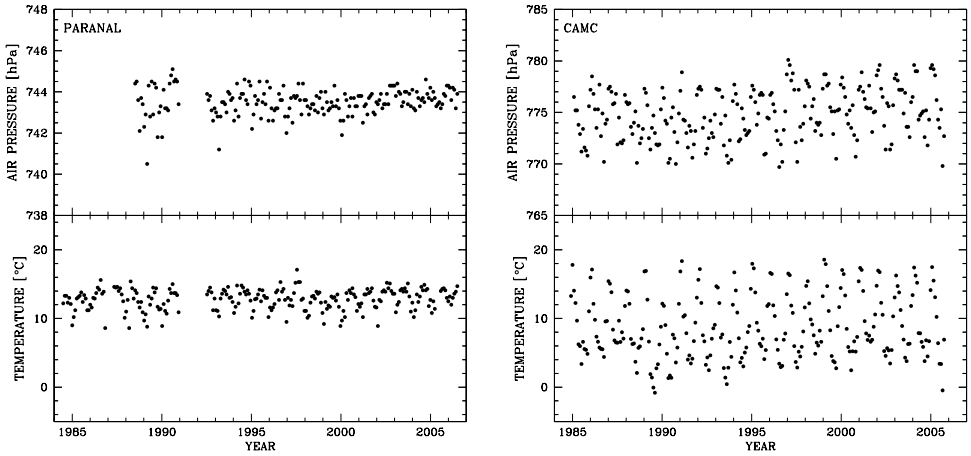

Figure 3.4: *Top: Monthly P at Paranal anc CAMC. Bottom: Monthly T at Paranal and CAMC.*

during the years at Paranal as confirmed by the analysis of the standard deviation of the annual averages. In fact at Paranal it decreased of about 70% between 1990 and 2006, while the same data computed at CAMC do not show the same phenomenon. Looking at monthly temperatures, we notice a lower seasonal dispersion at Paranal with respect to CAMC. Temperature dispersion remained almost constant up to now in both sites.
To check if the effect of the yearly variation of the pressure at Paranal can be explained taking into account wide-scale climatological episodes, we have checked a possible correlation with the Souther Oscillation Index. This analysis will be discussed in Section 3.7.

3.5.2 Short time scale air pressure variations

We have analyzed short time scales relationships (hour-by-hour and day-by-day) between air pressure and temperature variations . An example for January and July 1992 at CAMC is reported in Figure 3.5. We have cross-correlated the hourly mean of P and T in 1998, 1999 and 2000 at TNG and Paranal. Table 3.5 reports the obtained delay in hours. The typical correlation range at ORM is 50-90%, while at Paranal is between few % to 70%.

Table 3.5: *CAMC and Paranal typical delay in hours between variation of P and T.*

	1998		1999		2000	
Month	CAMC	Paranal	CAMC	Paranal	CAMC	Paranal
JAN	4	2	2	2	3	3
FEB	3	1	2	3	1	3
MAR	2	1	< 1	3	1	3
APR	1	1	< 1	2	2	2
MAY	1	2	< 1	2	< 1	4
JUN	< 1	4	< 1	3	< 1	5
JUL	< 1	3	< 1	3	< 1	< 1
AUG	< 1	2	< 1	3	< 1	–
SEP	< 1	3	< 1	2	< 1	–
OCT	1	2	1	2	2	3
NOV	1	2	1	2	2	2
DEC	1	2	2	3	2	3

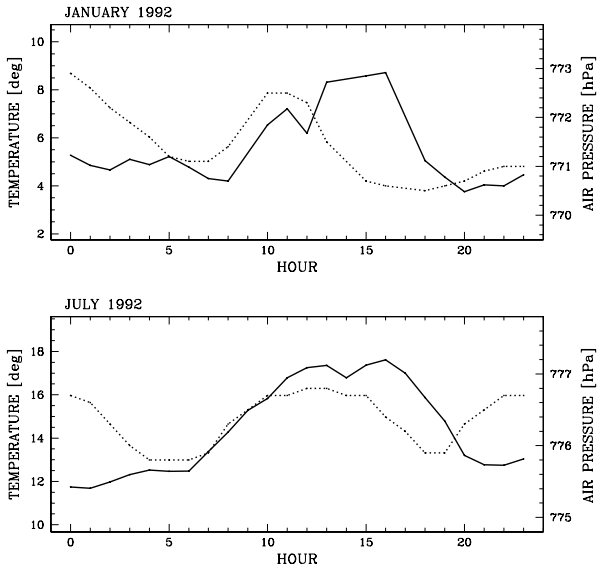

Figure 3.5: *Temperature (solid) and pressure (dotted) variations at CAMC in a sample of January and July 1992.*

Although the effect is more evident at ORM, in both observatories the delay decreases in warm seasons.
The relationship between P and T suggests that it is possible to foresee with 1 to 3 hours in advance the changes of the temperature on the basis of the changes in pressure. In this way it is possible to optimize the thermalization of the telescope and of the instruments.

3.5.3 General weather conditions at ORM and Paranal

In order to compare the general climate conditions at ORM and Paranal we should take into account that they are at different latitudes and different altitudes above sea level. So we need to put them in a scale of values to be comparable each other. This can be done calculating the theoretical pressure for the two sites using the barometric correction that depends on site's scale height H in the barometric law.
We can derive an empiric scale height using temperature and pressure data. Following Holton (1992), for an atmospheric layer of thickness $\Delta z = z_2 - z_1$ ($z_2 > z_1$) between the pressure surfaces P_1 and P_2 ($P_2 < P_1$) we have

$$\Delta z = \frac{R}{g_0} \int_{P_2}^{P_1} T \, d(\ln P) \tag{3.1}$$

where $R = 287$ J Kg^{-1} K^{-1} is the gas constant for dry air and $g_0 \equiv 9.80665$ m s^{-2} is the global average of gravity at mean sea level. The layer mean temperature can be defined as

$$\langle T_{layer} \rangle = \int_{P_2}^{P_1} T \, d(\ln P) \left[\int_{P_2}^{P_1} d(\ln P) \right]^{-1} \tag{3.2}$$

and the mean scale height as

$$H \equiv R \langle T_{layer} \rangle / g_0 \tag{3.3}$$

Using (3.2) and (3.3), (3.1) can be written as $\Delta z = -H \ \ln(P_1/P_2)$ that is

$$P_2 = P_1 \ \exp(-\Delta z/H) \tag{3.4}$$

Equation (3.4) is the tipical barometric law and means that the pressure decreases exponentially with the height by a factor of e^{-1} per H. The scale height is simply

$$H = -\frac{\Delta z}{\ln(P_1/P_2)} \tag{3.5}$$

At CAMC we have found a typical scale height $H_{CAMC} = 8325$ m and a theoretical pressure of 766.0 hPa in the period between 1998-2004, while the data give 775.9 hPa on average, confirming that ORM is dominated by high pressure. Same calculations in the same period at Paranal give $H_{PAR} = 8334$ m and a theoretical pressure of 738.3 hPa. This result is lower with respect to the averaged pressure for Paranal, so we can confirm that also Paranal is dominated by high pressure. The Paranal scale height is a bit higher than at ORM (8334 m vs 8325 m) as expected having a lower latitude site and higher average temperature than ORM.

3.6 The North Atlantic Oscillation (NAO) Index

The North Atlantic Oscillation is the dominant mode of atmospheric circulation in North Atlantic region (Wanner et al. 2001). It consists of a north−south dipole of pressure anomalies, with one center located over Greenland and the other center of opposite sign spanning the central latitudes of the North Atlantic between 35°N and 40°N.
NAO Index is generally defined as the difference in pressure between the Azores High and the Icelandic Low. The positive phase of the NAO reflects below−normal heights pressure across the high latitudes of the North Atlantic and above−normal heights pressure over the central North Atlantic, the eastern United States and western Europe. The negative phase reflects an opposite pattern of pressure anomalies over these regions. The NAO exhibits considerable interseasonal and interannual variability, and prolonged periods (several months) of both positive and negative phases of the pattern are common[3].
Because the great influences of the NAO on the meteo conditions in the northern emisphere, it is important to investigate a possible correlation between NAO and other key parameters determining good or bad observing astronomical conditions. For these reasons we calculated the annual averages for NAO from the monthly ones retrieved from the National Weather Service web site.
In Figure 3.6 (left: top and center) the NAO Index from 1985 to 2004 and the respective down−time at CAMC due to weather conditions is compared. No correlation is found between NAO Index and number of non-observing nights (the significance in this case is $<$ 0.3). A carefully inspection shows some particular effects of delay or different correlations (i.e. years 1989 and 1998) probably caused by peculiar events that should be investigated in other studies.
Figure 3.6 (left) also shows the comparison between NAO Index (center) and temperatures (bottom) computed from CAMC data archive. In this case, the correlation between the

[3] http://www.cpc.ncep.noaa.gov

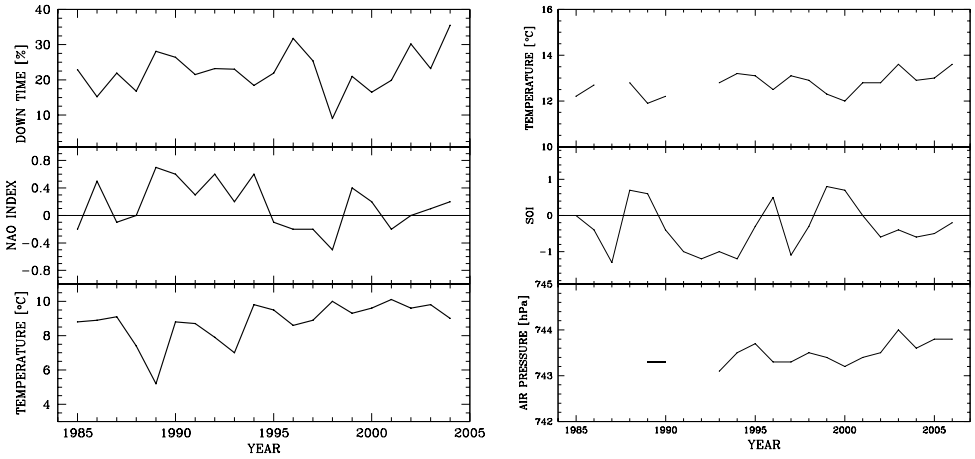

Figure 3.6: *On the left, (center) North Atlantic Oscillation Index vs: (top) down−time due to weather conditions and (bottom) annual temperature at CAMC. On the right, Southern Oscillation Index (middle) vs. annual temperatures (top) and annual air pressure (bottom) at Paranal. annual temperatures at CAMC site.*

amount of variability of the temperatures year by year and the trend of the respective NAO Index has about 0.8 of significance. The action of positive NAO Index is like a brake for the increase of temperatures, and like an accelerator for the decrease. Vice versa, negative NAO Index acts in opposite mode.
An interesting point is the assumption of Graham (2005) that there is a poor correlation on annual basis between NAO and air temperature from Mazo Airport in La Palma. This gives an indication of a different influence of the NAO above or below the inversion layer.

3.7 The Southern Oscillation Index (SOI)

In the case of Paranal we have analysed the Southern Oscillation Index. The SOI is defined as the difference in air pressure occurring between the western and eastern tropical Pacific (Tahiti and Darwin, Australia). Changes in the SOI correspond also with changes in temperatures across the eastern tropical Pacific. The negative phase of the SOI represents below-normal air pressure at Tahiti and above-normal air pressure at Darwin. Prolonged periods of negative SOI values reflect abnormally warm ocean waters across the eastern tropical Pacific, typical of El Niño episodes, while periods of positive SOI values coincide with abnormally cold ocean waters across the eastern tropical Pacific, typical of La Niña episodes.
Because of the strong influence of the SOI on the meteorological conditions in the southern

Table 3.6: *Strongest El Niño and La Niña episodes between 1985 and 2006.*

El Niño	La Niña
1987	1988
1992-1994	1996
1997	1999-2000

Table 3.7: *Seasons definition at Paranal and CAMC.*

	Paranal	CAMC
WINTER	July-August-September	January-February-March
SPRING	October-November-December	April-May-June
SUMMER	January-February-March	July-August-September
AUTUMN	April-May-June	October-November-December

hemisphere, and on observing conditions at Paranal and La Silla, it is important to investigate possible correlations between the SOI and the temperature and pressure at Paranal. For this reason we calculated the annual averages of the SOI from the monthly averages retrieved from the National Prediction Center Web site.
Figure 3.6 (middle) shows the SOI as a function of the year. Each minimum in the figure corresponds to warm episode (El Niño), while each maximum to cold episode (La Niña). As shown in the figure and also reported in Table 3.6, strong El Niño occurred in the years 1987, 1992-1994 and 1997, while strong La Niña occurred in 1988, 1996 and 1999-2000.
The top of Figure 3.6 shows the T annual averages at Paranal. We see an increase in the annual temperatures in connection with El Niño, vice versa minimum temperatures occur with La Niña episodes (correlation is ~ 0.7). Local minimums in the P annual trends at Paranal (Figure 3.6, bottom) are linked to the presence of La Niña events, while maximums with El Niño, but in this case poor correlations is found between the yearly trends.

3.8 Relative humidity

Relative humidity and dew point are two important parameters for the astronomical instrumentation, because they set the occurrence of moist and water condensation on the coldest part of the telescope and of the instruments. In particular, these parameters may affect the upper surface of the main mirror and the pipes of the cooling system.
We separated the annual RH in 4 seasons as defined in Table 3.7. Note that Paranal and ORM are in opposite hemispheres, so the definitions are inverted for the two observatories.

To facilitate the discussion we consider as *cold season* autumn and winter, and *warm season* spring and summer. Tables 3.8 and 3.9 report the computed annual RH in cold and warm seasons at Paranal and CAMC. Typically, in cold seasons RH is lower than 60% at CAMC and 15% at Paranal. In warm seasons RH is lower than 40% at CAMC and 20% at Paranal.

Table 3.8: *Mean annual RH in cold seasons at Paranal and CAMC [%].*

Year	1985	1986	1987	1988	1989	1990	1991	1992
Paranal	9.1	9.7	–	9.2	12.0	9.6	–	–
CAMC	40.3	43.8	48.2	52.2	49.2	56.5	57.4	52.7
Year	1993	1994	1995	1996	1997	1998	1999	2000
Paranal	10.8	11.0	10.5	10.7	14.8	12.6	10.9	14.9
CAMC	47.8	40.4	40.6	53.1	44.7	30.9	12.5	53.0
Year	2001	2002	2003	2004	2005	2006	Avrg.	
Paranal	12.5	14.5	11.4	12.4	11.5	12.4	11.6	
CAMC	33.7	56.4	36.3	40.8	–	–	44.5	

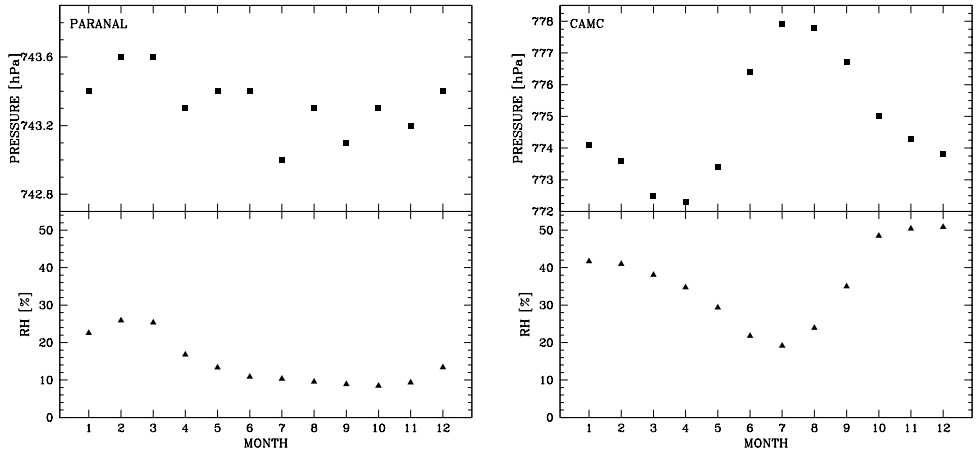

Figure 3.7: *Averages of monthly P (top) and RH (bottom) at Paranal (left figure) and CAMC (right figure).*

Figure 3.7 shows the seasonal trend of P (top) and RH (bottom) in both sites considered as the average of the same month through the considered years of the databases. The variation of P at Paranal is < 1 hPa, very lower with respect to CAMC (~ 6 hPa!). We clearly see an anti-correlation between P and RH in summer at CAMC, while at Paranal this effect is not obvious. Because of the effect of the Bolivian Winter, driving equatorial humid air from amazonian basin along the Andes, the RH at Paranal is higher in warm seasons ($\sim$ 20%) with respect to cold ones ($\sim 12\%$). Higher RH appears clearly in wintertime than in summertime at CAMC.
A standard requirement for the use of telescopes is a RH value $< 80\%$ or $< 85\%$. For both sites we have calculated the number of nights in which RH has been higher than the mentioned limits for more than 50% of the duration of the night. Only nights which duration has been ≥ 6 hours have been used in the calculation. Results are reported in Table 3.10 and denote a significant difference between Paranal and CAMC, the first appearing almost immune to high RH events. The number of nights at CAMC is the same for the two imposed limits.

Table 3.9: *Mean annual RH in warm seasons at Paranal and CAMC [%].*

Year	1985	1986	1987	1988	1989	1990	1991	1992
Paranal	–	16.9	15.8	13.0	16.9	11.5	16.3	–
CAMC	43.1	42.0	43.6	30.8	35.9	42.5	29.2	26.1
Year	1993	1994	1995	1996	1997	1998	1999	2000
Paranal	–	15.8	16.2	15.0	20.0	16.4	21.1	25.5
CAMC	21.0	16.7	26.5	15.0	15.6	6.5	19.7	24.3
Year	2001	2002	2003	2004	2005	2006	Avrg.	
Paranal	22.8	19.8	15.3	17.0	18.0	–	17.4	
CAMC	21.9	22.0	24.5	32.2	–	–	27.0	

Table 3.10: *Paranal and CAMC: annual number of nights in which RH has been higher than 80% and 85% for more than 50% of the duration of the night. Only nights which duration has been ≥ 6 hours have been used in the calculation.*

	$RH > 80\%$		$RH > 85\%$	
Year	Paranal	CAMC	Paranal	CAMC
1984	–	2	–	2
1985	1	8	0	8
1986	0	8	0	8
1987	0	22	0	22
1988	0	51	0	51
1989	1	68	0	68
1990	0	73	0	73
1991	0	53	0	53
1992	0	58	0	58
1993	0	58	0	58
1994	0	41	0	41
1995	0	51	0	51
1996	0	81	0	81
1997	2	52	0	52
1998	0	36	0	36
1999	2	48	2	48
2000	4	49	2	49
2001	0	60	0	60
2002	4	31	3	31
2003	0	27	0	27
2004	0	35	0	35
2005	3	–	3	–

3.9 Analysis of the dew point

The dew point temperature (T_{DP}) is the critical temperature at which condensation occurs. When dew point temperature and air temperature T are equal the air said to be saturated and condensation appears if the air cools. It is clear that the knowledge of the dew point temperature is crucial for the maintenance of the optics of the telescope to avoid condensation, in particular if the the instrumentation is maintained at temperatures few degrees lower than the air temperature. Condensation can be reached mostly in clear nights, when the earth cools rapidly, therefore it is important to know the percentage of time in which condensation may occur to have the best performances from ground based telescopes. To this aim we have computed the dew point temperature using nighttime data for both Paranal and CAMC. We have defined as nighttime the range 20:00−6:00 hr Local Time. Only clear nights have been taken into account.

The analysis concerns the annual percentage of time in which $\Delta T = T - T_{DP} < X$, where X corresponds to a variable upper limit for ΔT ($X = 1$ and 5°C). This statistics is crucial for the knowledge of the amount of time in which a danger of condensation on the telescopes hardware may occur in two extreme ΔT.

In Figure 3.8 we report the computed frequencies in the two sites. In winter, spring and autumn we see a significant difference between Paranal and CAMC until 2000. After such year the two sites seem to became more similar.

Paranal shows negligible percentages for all X limits in spring, while it never goes above $\sim 4\%$ for $X = 5$°C in winter (2002) and autumn (2002 and 2004). CAMC has frequency often $> 10\%$ when $X = 5$°C. After 2001 CAMC shows similar percentages with respect to Paranal when $X = 1$°C. This is due to the very little increasing of the percentages at Paranal after 2001. In summer the two sites are very similar maintaining percentages never

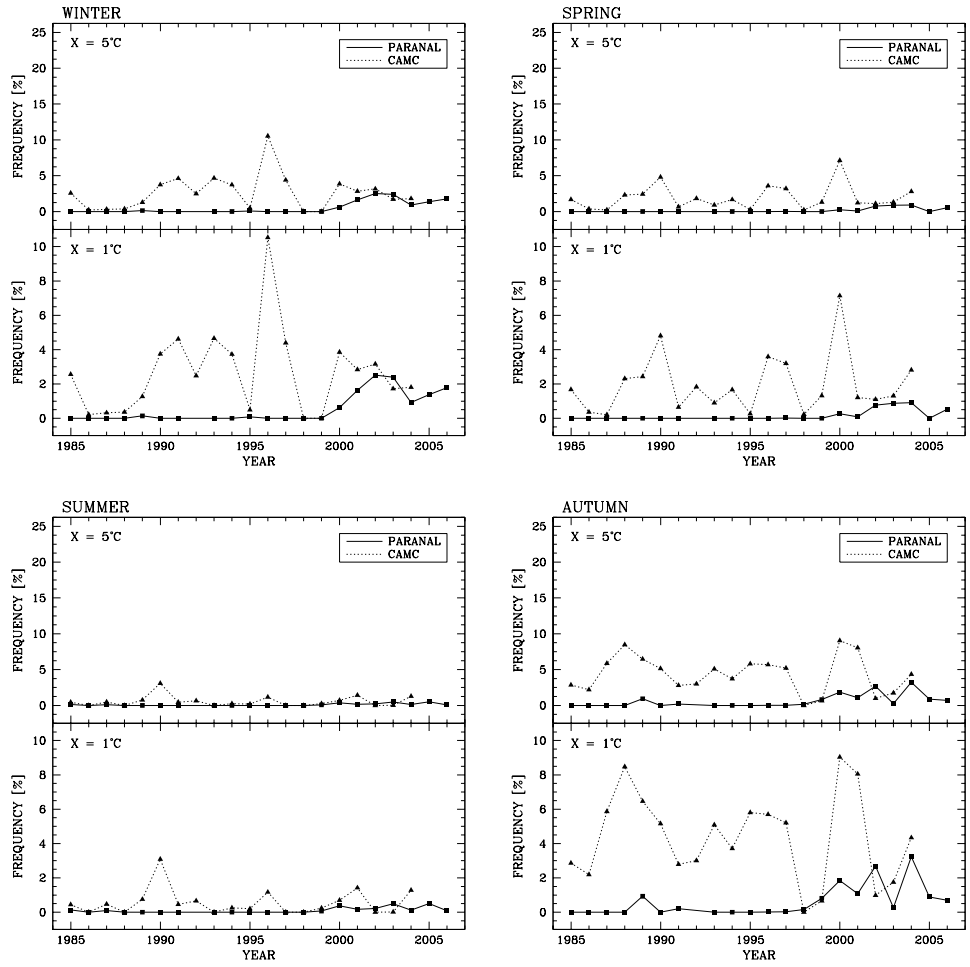

Figure 3.8: *Nighttime annual percentage of time in which* $\Delta T = T - T_{DP} < 1$ *and* $5^\circ C$ *at Paranal and CAMC in winter, spring, summer and autumn.*

higher than $\sim 3\%$ at Paranal and $\sim 4\%$ at CAMC when $X = 5°$C, with the exception of the year 1990 for CAMC.

3.10 Wind

Trade winds are the main responsibles of the climate of Canary Islands. Font-Tullot (1956) affirms that the overall climate of the Canary Islands is determined by the trade winds which are 90% prevalent in summer and 50% prevalent in winter, with main direction from NW at the level of the observatories. Mahoney et al. (1998) point out to a seasonal variation due to the Azores anticyclone which, together with the Canary Current, drives the trades in N-S direction.

Several authors analyzed the wind pattern and speed at ORM, but results are quite different. In the period 1971-1976 Brandt&Righini (1985) obtained a mean velocity of 6 m s^{-1} and dominant wind direction NW with secondary peaks from NE to SE at ORM JOSO (Joint Organization for Solar Observations) sites. Daytime statistics by Brandt&Woehl (1982) for

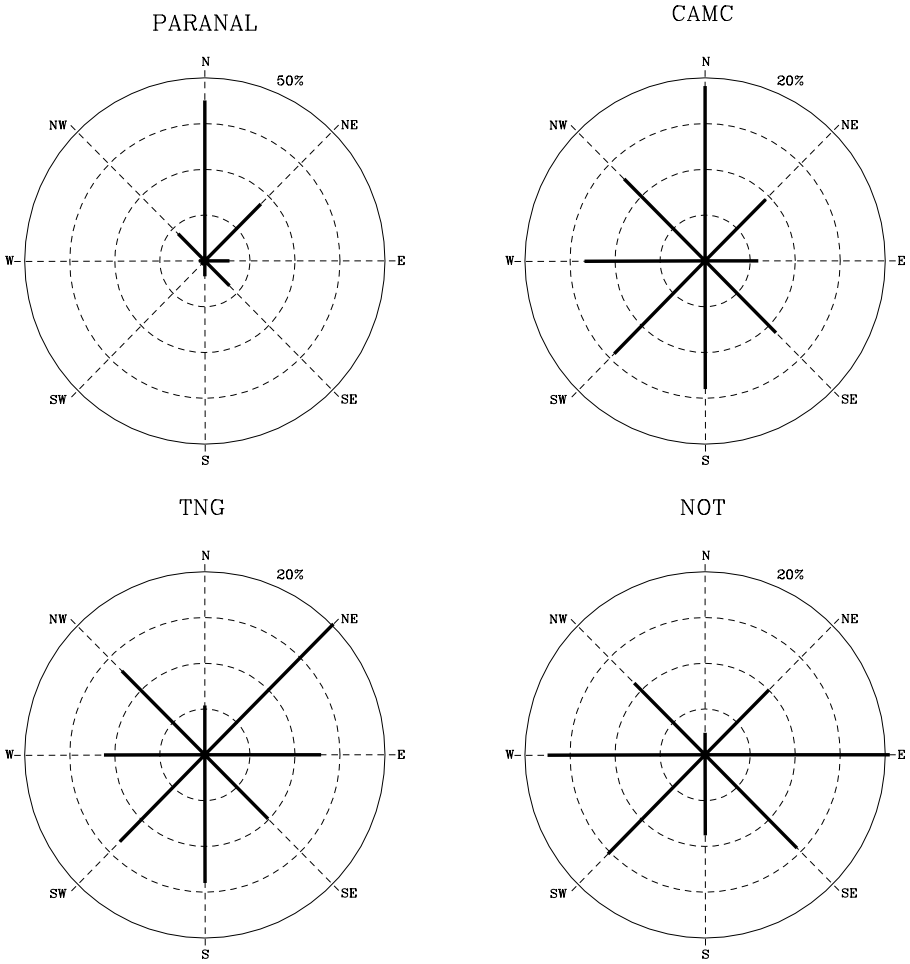

Figure 3.9: *Nighttime wind roses at Paranal (1998-2006), and CAMC, TNG and NOT (1998-2004).*

period 1978-1979 on the neighbouring slope of ORM shows distribution in wind direction with a prevailing component from E.
Nighttime data found by Mahoney et al. (1998) at Gran Telescopio Canarias (GTC) site denote NE dominant wind direction. Further analysis by Jabiri et al. (2000) at CAMC site in the period 1987-1995 shows a prevailing wind flow from N-NW during the day that change to N-NE in nighttime. Jabiri's wind speed analysis give a mean w_{sp} of 2.8 m s^{-1}.
We can conclude that the wind direction significantly changes across the site.
In our analysis we make use of TNG and NOT 7 years long databases (1998-2004) and CAMC 20 years long database (1985-2004). The TNG sensor is placed on the top of the meteo tower at an altitude of 2370 m above sea level, while NOT and CAMC sensors are approximatively placed at the same height of the respective dome floors, that means 2382 m for the NOT sensor and 2326 m for the NOT sensor.
Figure 3.9 shows the nighttime wind roses for Paranal, TNG, NOT and CAMC calculated taking into account the common period 1998-2004 for telescopes at ORM, and 1998-2006 for Paranal. More detailed informations about the behaviour of the wind direction in each yaer are given in Tables 3.11, 3.12, 3.13 and 3.14.

Table 3.11: *1998-2004 nighttime wind direction percentages for TNG.*

	N	NE	E	SE	S	SW	W	NW
1998	8.4	22.6	11.2	11.8	14.6	10.4	10.3	10.7
1999	6.0	20.3	11.3	8.0	13.8	12.9	10.3	17.4
2000	4.1	19.7	11.4	11.3	14.1	13.3	10.9	15.2
2001	6.8	21.5	14.0	7.0	12.3	12.5	12.6	13.3
2002	4.2	18.9	14.3	10.0	14.8	14.0	13.2	10.6
2003	5.0	17.8	11.3	9.6	14.7	15.5	12.8	13.3
2004	4.6	21.2	15.6	11.1	13.3	14.2	8.3	11.7

Table 3.12: *1998-2004 nighttime wind direction percentages for NOT.*

	N	NE	E	SE	S	SW	W	NW
1998	1.4	9.6	15.0	13.8	9.5	16.1	18.5	16.1
1999	2.2	11.7	22.6	13.6	10.0	17.0	13.6	9.3
2000	1.8	9.8	21.9	16.0	7.9	13.2	17.6	11.8
2001	1.2	11.6	23.1	14.8	10.1	15.2	15.7	8.4
2002	3.2	9.0	20.2	14.5	7.0	15.4	19.3	11.4
2003	2.8	10.1	24.4	14.1	9.8	14.7	16.6	7.5
2004	3.9	8.3	17.1	13.8	8.0	16.2	20.6	12.1

TNG shows a NE dominant mode in nighttime (see Table 3.11) and a less evident prevailing wind from S to W in daytime. The mean wind speed is $\sim$4.6 m s^{-1}, lower than the 6 m s^{-1} found by Brandt&Righini (1985) and higher than the 2.8 m s^{-1} of Jabiri et al. (2000). The maximum wind speed measured at TNG is of 26.9 m s^{-1} in January 1999.
Dominant direction both in nighttime (Table 3.12) and daytime at NOT has two prevailing directions from W or E. NOT shows a mean w_{sp} of 7.2 m s^{-1}, the highest measured at ORM. The maximum wind speed measured at NOT is 29.8 m s^{-1} in December 2004.
CAMC shows a lower mean wind speed (2.2 m s^{-1}). This result is also lower than the 2.8 m s^{-1} at CAMC found of Jabiri et al. (2000). The difference can be explained in term of statistics because our analysis uses a longer database. The maximum wind speed measured at CAMC is 18.3 m s^{-1} in April 1987.
Wind direction for CAMC is very peculiar. Table 3.13 shows nighttime $\vec{w}_{dir}$ percentages per sector in nighttime over the two analyzed decades. Northern winds seems to oscillate with a period of 10 years, while winds from NW shows a similar oscillation in opposite phase. Anyway, there are no evidences of a prevailing direction, furthermore N and NW percentages become periodically comparable with those of other directions. The situation changes dramatically in 2004 when the percentage of wind from N increases steeply up to 71.8%. The recent behaviour of the wind at CAMC point out that a deeper analysis of such phenomenon will be needed in the future.
Muñoz-Tuñón et al. (1998) demonstrated the homogeneity of the image quality among the ORM. Considering the difference between nighttime wind roses at different locations in the observatory that we have mentioned above, and considering also the complex orography of the ORM, should be interesting to investigate if any difference exists in the local surface turbulence among the observatory. This is an important issue because local conditions have been demonstrated to be crucial for image quality at Paranal (Lombardi et al. 2008b and Sarazin et al. 2008).

At Paranal a dominant wind blowing from north and north-east appears during the night. Table 3.14 reports the computed wind direction frequencies at Paranal between

Table 3.13: *1985-2004 nighttime wind direction percentages for CAMC.*

	N	NE	E	SE	S	SW	W	NW
1985	14.2	11.9	7.6	8.7	23.2	16.1	5.6	12.6
1986	22.5	18.4	12.9	12.9	12.4	7.5	5.5	8.0
1987	7.9	12.8	13.5	11.3	14.8	18.4	8.5	12.9
1988	7.6	9.6	16.6	14.3	20.1	12.3	6.6	12.9
1989	8.6	10.2	13.0	12.7	16.7	17.4	7.8	13.6
1990	7.6	11.5	16.5	13.5	15.0	17.8	7.6	10.5
1991	8.6	17.6	16.2	13.1	13.3	13.4	6.6	11.7
1992	9.3	14.4	18.0	16.6	13.7	9.5	7.8	10.7
1993	9.7	13.0	11.8	14.3	13.8	10.0	12.7	14.7
1994	26.6	13.6	9.1	12.5	15.5	8.7	5.8	8.2
1995	24.3	17.9	6.0	14.9	11.0	10.0	7.1	8.8
1996	5.4	1.7	6.8	47.1	17.3	7.1	7.7	6.7
1997	2.6	5.1	4.7	11.6	15.9	16.7	18.2	25.3
1998	2.0	4.8	4.2	11.3	16.1	20.4	22.6	18.7
1999	2.6	5.1	4.1	11.1	16.9	17.4	20.3	22.6
2000	7.8	6.8	5.3	11.3	15.0	16.9	18.5	18.5
2001	15.4	15.3	8.2	11.0	13.7	16.6	10.9	9.0
2002	15.5	14.2	9.1	16.3	16.7	12.2	8.9	7.2
2003	16.2	16.7	8.4	12.4	12.2	12.5	11.1	10.5
2004	71.8	3.6	2.6	5.6	7.9	4.1	1.7	2.6

Table 3.14: *1998-2006 nighttime wind direction percentages for Paranal.*

	N	NE	E	SE	S	SW	W	NW
1998	48.6	23.6	6.5	4.3	2.0	0.6	1.1	13.3
1999	46.7	23.3	6.2	8.0	3.7	0.4	1.2	10.5
2000	46.8	21.1	5.8	8.9	4.7	1.0	1.7	10.0
2001	45.8	19.6	7.8	9.8	3.4	1.1	2.0	10.5
2002	46.4	21.3	6.3	7.7	3.3	1.4	2.7	10.9
2003	38.5	19.8	7.2	14.6	4.0	1.9	2.0	12.0
2004	42.8	23.3	8.7	10.1	3.0	1.8	1.5	8.8
2005	38.6	19.3	5.6	12.3	8.0	3.4	1.1	11.7
2006	35.0	26.7	7.8	12.3	6.5	2.0	1.5	8.2

1998 and 2006. The values in the table are plotted in Figure 3.10 where we include the wind frequencies since 1985 distinguishing two different epochs before and after the VLT first light occurred in 1998. Wind from north shows a clear decreasing trend through the years togheter with an increasing of the wind direction from south-east. This result is in agreement with Sarazin (2004) that in a previous analysis show a progressively replacement of the north-westerly wind by a north-easterly wind. To better investigate this behavior we have computed the yearly evolution of the nighttime frequencies of the wind in each direction. There is a strong oscillation of the wind from north until 1994 (see Figure 3.10, left). Data from 1998 show a clear trend as shown in Table 3.15 that reports the computed trend of the yearly evolution of the frequencies in each direction. Wind from north is characterized by a decrease of the frequency of 1.6% per year marginally compensated by and increasing of wind coming from south-east (0.9% per year). We can conclude that progressively wind coming from the sea is replaced by wind coming from the Atacama Fault. At the moment it is not clear if we are in presence of a wide-scale changing of the atmospheric conditions or if this effect is induced by local conditions.

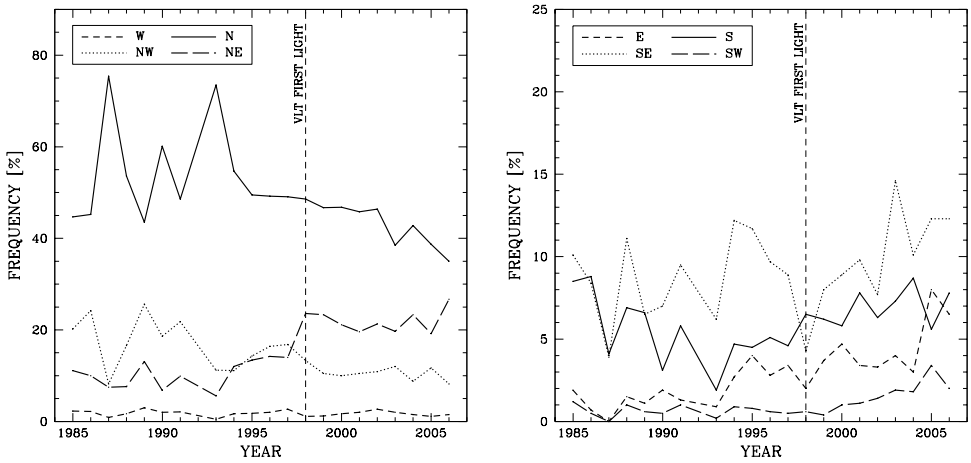

Figure 3.10: *Nighttime evolution of the wind direction through the years at Paranal for quadrant W-NE (left figure) and quadrant E-SW (right figure).*

Table 3.15: *Nighttime yearly evolution of the wind direction frequencies at Paranal from 1998 to 2006 as [% per year].*

N	NE	E	SE	S	SW	W	NW
-1.6	$+0.3$	$+0.2$	$+0.9$	$+0.5$	$+0.3$	< 0.1	-0.3

3.10.1 Wind speed limits for observational purposes

The analysis of the wind speed at Paranal and ORM is carried out from the calculation of the time in which w_{sp} is in fixed intervals established on the basis of the safety operations at the observatories. We consider five main situations:

- $w_{sp} < 3$ m s^{-1}: negligible wind speed, typically in this case the seeing increases;
- $3 \leq w_{sp} < 12$ m s^{-1}: the wind speed is in the safety range, telescopes observe without restriction in the pointing direction, seeing conditions are optimal;
- $12 \leq w_{sp} < 15$ m s^{-1}: in this interval the telescopes can only point to objects in a direction $\geq 90°$ with respect to the actual w_{dir});
- $w_{sp} > 15$ m s^{-1}: at ORM the telescopes are closed for strong wind;
- $w_{sp} > 18$ m s^{-1}: at Paranal the telescopes are closed for strong wind.

Table 3.16 reports the percentages of time in which the wind speed is in the fixed intervals. Also in this case, because of the wind speed differences noticed between CAMC, TNG and NOT, none of them can be considered as fully representative of the ORM, so they have to be taken into account together. For this reason Table 3.16 reports also the results for TNG and NOT obtained in Paper II.
The site of CAMC has a predominance of $w_{sp} < 3$ m s^{-1} (83.6%), while Paranal has 22.1%, TNG the 30.2% and NOT the 18.5%. Paranal preserves good wind speed conditions in the $\sim 70\%$ of the time (same of TNG and NOT), while CAMC only the $\sim 16\%$. CAMC never shows $w_{sp} > 12$ m s^{-1}, while Paranal has a percentage of 5.9 in the interval $[12, 15[$ m s^{-1} and 3.3% of $w_{sp} > 15$ m s^{-1} while not-observing conditions due to strong wind occur in

Table 3.16: *Nighttime wind speed statistics at Paranal (1998-2006) and CAMC, TNG and NOT (1998-2004).*

w_{sp} range [m s^{-1}]	Paranal [%]	CAMC [%]	TNG [%]	NOT [%]
$w_{sp} < 3$	22.1	83.6	30.2	18.5
$3 \leq w_{sp} < 12$	68.7	16.4	68.4	70.2
$12 \leq w_{sp} < 15$	5.9	0.0	1.1	7.1
$w_{sp} \geq 15$	3.3	0.0	0.3	4.2
$w_{sp} \geq 18$	< 0.5	0.0	0.0	1.2

$< 0.5\%$ of the time. The TNG has $\sim 1\%$ of the time with $w_{sp} > 12$ m s^{-1}, while NOT has considerable higher values in the intervals $[12, 15[$ ms^{-1} s^{-1} (7.1%) and $w_{sp} > 15$ m s^{-1} (4.2%). The highest wind speed measured at Paranal during the years 1998-2006 is 27.4 m s^{-1} in May 2000.

3.11 Preliminary correlations between seeing and meteorological parameters

3.11.1 Seeing and vertical temperature gradient

It is well known that the image quality, computed as FWHM of the image profile obtained at the focal plane of the telescope, is strongly dependent on the temperature gradient between the main mirror and the external air. Since the year 1995 Zago (1995) shows that a difference in temperature of 1°C can worsen the seeing of about 0.5 arcsec. More recently Ortolani (2008) shown the same results obtained using images taken at TNG in June 2008 at TNG in La Palma reaching values of seeing close to the best conditions. This result, reached after several nights spent to optimize the observing conditions, put the question if it is possible to predict the observing conditions few hours in advance in order to reduce the loosing time directly at telescope. A collaboration with meteorologist is welcome to go in this direction.

Following Racine et al. (1991), Zago (1995), Lombardi et al. (2006) and Ortolani (2008) we check if any correlation exists between the image quality and the vertical temperature gradient below the TNG primary mirror. We make use of 118 images obtained with the image camera OIG (Optical Imager of Galileo) at TNG, pointed near the zenith (and corrected to the true zenith by a small amount), from 31 January to 4 February 2000. We computed FWHM of several stellar images in the V band frames following the standard procedure (bias subtraction and flat fielding) using IRAF packages. In a comparison between the temperature T_{M1} measured close to the TNG primary mirror and T_{TNG} we found no appreciable difference, so we can approximate T_{TNG} as the temperature of M1.

Remembering that T_{TNG} is the temperature measured on the tower at 10 m, we compute the gradients of temperature as $\Delta T_2^{TNG} = T_2 - T_{TNG}$ (where T_2 is the temperature measured by the sensor at 2 m) at the same UTs of the 118 images of which we computed the FWHM. Figure 3.11 displays the comparison between ΔT_2^{TNG} and the FWHM. In the plot the seeing deteriorates when $\Delta T_2^{TNG} > -0.6$°C. This can be explained as consequence of the lower temperature at 2 m because the higher temperature at 10 m inhibits the thermal convection below the primary mirror height.

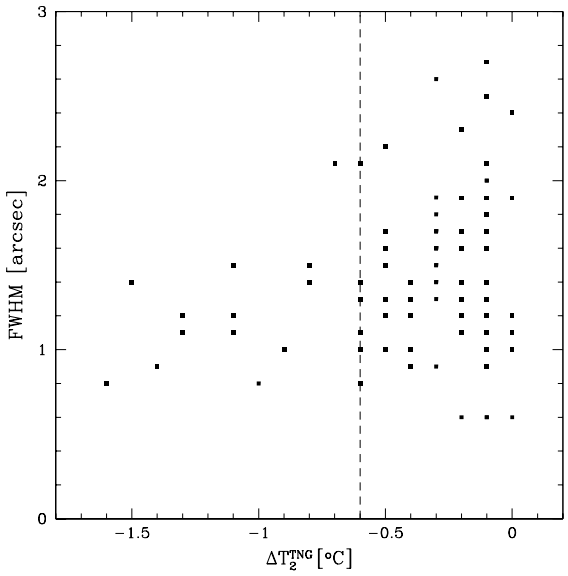

Figure 3.11: *Seeing in V band VS ΔT_2^{TNG} at TNG.*

3.11.2 Seeing and wind speed

Wind speed is an important parameter because is linked to the optical turbulence (C_n^2) and to the wave-front coherence time. It is well known (Sarazin 1992) that the effects of wind velocity are negligible for $w_{sp} \in [w_{MIN}, w_{MAX}[$, where the two extremes are site dependent and $w_{MIN} > 0$.
In this example we use the same computed FWHM of Section 3.11.1. The images quality in term of FWHM is compared to the wind speed measured at the same starting UTs of each image. Figure 3.12 displays the comparison between w_{sp} and the FWHM. We see that the 50% of the points is distribuited below $w_{sp} < 3.3$ m s^{-1} (first vertical dashed line) where the median values of FHWM is 1.5 arcsec. Furthermore, for $w_{sp} \geq 3.3$ m s^{-1} the distribution of the points shows a median value of 1.3 arcsec. This indicates that for $w_{sp} < 3.3$ m s^{-1} the seeing deteriorates, so we can define $w_{MIN} = 3.3$ m s^{-1}. No observations are available for $w_{sp} > 12$ m s^{-1} (second vertical dashed line). Sarazin (1992) shows in La Silla a limiting value of $w_{MAX} = 12$ m s^{-1}. Finally, we can conclude that TNG has optimal seeing conditions if $w_{sp} \in [3.3, 12[$.

In a second experiment we used seeing data from the Paranal DIMM and meteorological data from the Paranal meteo tower in the common period between 10 April 2005 and 30 November 2007. DIMM seeing at Paranal is measured at 6 m above the ground. As demonstrated in Lombardi et al. (2008b), because of the presence of a strong turbulent surface layer at Paranal that extents between the ground and ∼20 m (see Chapter 8), DIMM seeing is overestimated with respect to the real turbulence affecting the science with the VLT. For this reason the median seeing values reported in this Section should not be considered as representative of the site, but only to understand the behavior of the turbulence within the considered synoptical parameters. We have calculated the median DIMM seeing in connection with different wind speed conditions. We have used bins of 2 m s^{-1}. Table 3.17 shows the median DIMM seeing calculated in each bin and the frequencies of w_{sp} in the considered period.

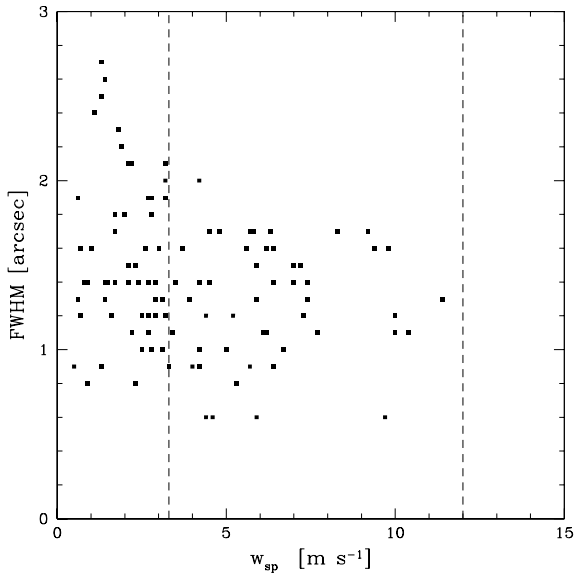

Figure 3.12: *Seeing in V band VS w_{sp} at TNG. The two extremes for optimal observations are indicated.*

Table 3.17: *Median DIMM seeing in connection with wind speed at Paranal between 10 April 2005 and 30 November 2007. Wind speed frequencies in the same period are also reported.*

w_{sp} [m s^{-1}]	seeing [arcsec]	freq. [%]
$w_{sp} < 2$	0.90	13.0
$2 \leq w_{sp} < 4$	0.80	18.3
$4 \leq w_{sp} < 6$	0.82	18.3
$6 \leq w_{sp} < 8$	0.85	16.3
$8 \leq w_{sp} < 10$	1.13	16.5
$10 \leq w_{sp} < 12$	1.21	9.9
$12 \leq w_{sp} < 14$	1.42	5.0
$14 \leq w_{sp} < 16$	1.44	2.3
$16 \leq w_{sp} \leq 18$	1.66	0.4

As shown in the table the best seeing conditions occurs when w_{sp} is between 2 and 8 m s^{-1} ($\sim$0.82 arcsec). In the considered period this has occurred the 52.9% of the time.

3.11.3 Seeing and wind direction

Using same Paranal data analyzed in Section 3.11.2 we have computed the median DIMM seeing in connection with wind coming from each direction defined in the windrose and results are reported in Table 3.18.
We found that at Paranal the DIMM seeing is clearly direction dependent. The best conditions are if the wind comes from north to west, that is from the Pacific Ocean. In this case, because its distance of 12 km form the coast, the observatory is under *oceanic island*-like conditions. Instead, there is a worsening of the DIMM seeing if the wind comes from north-east to south, that is from the Andes mountains.
In Table 3.18 we also report the frequencies of the wind direction in the considered period. As shown in the table, very good seeing conditions for the Paranal DIMM (i.e. from north to west) occurred the 52.0% of the time.

Table 3.18: *Median DIMM seeing in connection with wind direction at Paranal between 10 April 2005 and 30 November 2007. Wind direction frequencies in the same period are also reported.*

w_{dir}	seeing [arcsec]	freq. [%]
N	0.89	40.4
NE	1.23	24.9
E	0.97	6.9
SE	1.07	8.7
S	1.12	6.2
SW	1.00	1.3
W	0.77	1.7
NW	0.71	9.9

Chapter 4

Atmospheric dust and aerosol extinction

Abstract

Atmospheric extinction is the astronomical parameter that evaluate sky transparency. Air dust content may influence the astronomical extinction form U to the near-IR and Laser Guide Star efficiency. The optical properties of airborne dust in La Palma have been investigated collecting outdoor data using the TNG dust monitor. We found that particles at ORM can reach an altitude of 2.5 km above the observatory. The aerosol extinction process is more efficient for particles $\geq 1.0\mu$m.

4.1 Introduction

Due to the proximity of the ORM to the North African continent, the winds coming from the central side of the Sahara desert carry a large amount of dust in suspension that can reach high altitudes and increase the atmospheric dust concentration.
Whittet et al. (1987) pointed that this wind action removes approximately $2 \cdot 10^8$ tonnes of dust every year from Sahara desert, and they can be carried out to altitudes up to 6 km. This seasonal action can reach the south of the Canary Islands, and extended dust clouds often appear above the sky of La Palma, originating a phenomenon locally named *la Calima*. This natural event may affect the quality of the astronomical observations reducing the available radiation. Furthermore, it can reduce the quality of the observations since the extinction varies across the sky.
In the optical band the extinction is dominate by Rayleigh scattering due to particles, typically molecules, smaller with respect to the working wavelenght. The Rayleigh scattering decreases with the altitude and larger particles (dust and aerosols) contribute to increase the extinction, as it happens at ORM when is affected by Calima.
The first detailed study of the impact of Calima on astronomical observations in La Palma is in Murdin (1985), who found a seasonal trend in atmospheric transmission, ranging from 90% of nights classified as good (i.e., nearly aerosol-free), between October and March, to 58% during July, August, and September. Another interesting result from Murdin is the atmospheric extinction measured in a site-test campaign in La Palma. A Murdin summarisation of studies from other authors shows that 78% of the clear nights in the months starting from February to September 1975 and 83% from December 1974 to November 1975 have extinction less than 0.3 mag airmass^{-1}. In this context, aim of our study is to provide

the aerosol extinction using a wider database collected in the same area.
To improve the TNG meteorological station, the TNG site group put in operation a dust monitor. The first preliminary results can be found in Porceddu et al. (2002) and Ghedina et al. (2004). The primary motivation behind this measurement is to have a continuous characterisation of the air conditions above the primary mirror for several reasons. The first one is to compare dust measurements and atmospheric extinction to know which level of dust may affect astronomical observations. The second is to have better maintenance. In fact we know that the deposition of the dust over the optical surfaces reduces both the optical throughput (laboratory measurements of the primary mirror reflectivity show a decrease from 99% reached in the case of fresh aluminum to 70% in the case of a dusty surface) and the signal-to-noise ratio of the images. The third one is for safety reasons and for coating lifetimes, when humidity condensation sticks the dust on the mirror. The knowledge of the level of dust counts helps us to prevent damage to the optical surfaces of the telescope. Finally, the knowledge of the dust concentration at different sizes is also important for the proper design of the sealing of the telescopes and instruments moving mechanical parts.
Extended dust clouds periodically appear above the ORM complex. Murdin (1985) shows that dust collected at the ground level at ORM is composed of small round quartz aggregates having diameters ranging between 10 to 60 μm diameter. The optical properties of this dust have been investigated by several authors (Stickland 1987; Murdin 1985; Jiménez et al. 1998), all founding a flat wavelength dependence of the extinction; in particular, Murdin points out that Saharian dust's size is much bigger than the standard photometric V band wavelength. Big plumes of dust during the Calima days are also visible using satellites probes. In Siher et al. (2004) an analysis of 5200 data covering the years 1978-1993 shows a correlation between astronomical extinction and the Total Ozone Mapping Spectrometer (TOMS) satellite derived extinction as well as a seasonal trend above the Canaries with a significant increase in dusty days at the end of July. Siher et al. (2004) also shows an average of 55 dusty days from the beginning of June to the beginning of September (about half of the summer nights). The data since 1978 seems to indicate that the dusty period is drifting during the years. An independent analysis, based on CAMC telescope data, has been published by Guerrero et al. (1998).
The present Chapter has the goal of improving the knowledge of the aerosol-particle-size distribution and the effects on astronomical observations in La Palma. In particular, we have analysed for the first time the influence of the dust collected at the level of TNG primary mirror (M1) as a function of its size to the aim: a) to understand if local measurements may be taken as good indicators of the upper conditions in the atmosphere (a dust ground condition has reproduced a similar situation in the atmosphere?); b) to give an accurate extinction study selecting among different sizes of dust; c) to use this information as a primary tool for a fast warning of the unclean environment.
Results shown in the present Chapter have been already published in Lombardi et al. (2008a) (hereafter Paper III).

4.2 The dust monitor

The selection of air-particles counting equipment is primary triggered by the particle sizes to be monitored to obtain their estimated amount. The parameters used for this selection were the sizes of the dust, the flow rate, and the background noise counts. Each measured size of the dust corresponds to the number of available channels of the counter. The sensitivity of the detector is given by the smallest size of particle that the sensor is able to detect. The

Table 4.1: *Main characteristics of the Abacus TM301 dust monitor.*

size sensitivity	0.3 μm at 50% counting efficiency
input flow rate	0.1 Cubic Foot Minute [CFM]
size channels	0.3, 0.5, 1.0, 5.0 μm
light source	laser diode ($\lambda = 780$ nm)
concentration limits	$\geq 10^6$ per dm instantaneous
zero counts	< 1 per CF
output	RS-232
data storage	500 sample, rotating buffer
sample time	selectable from 1 sec to 99 minutes
purge time	selectable from 1 sec to 99 minutes
dalay time	selectable from 1 sec to 99 minutes

flow rate is the amount of the flux that the sensor can receive through the sample volume, while the background noise is the instrument dark current value. We have addressed our choice to an easy-to-use instrument, hand-held, reliable, and very sensitive. Moreover, a particle counter based on the optical detection technique that can count particles above 5.0 μm diameter was selected. The reason for such sensitivity is that we expect the number of dust particles to be less than the total number of atmospheric particles and we expect them to occur mostly on scales near 1 μm with a typical concentration range of a few tens per cubic centimetre. We therefore chose the particle counter Abacus TM301 (made by Particle Measuring System, Inc.), which uses a laser scattering technique for environmental ambient air analysis. Abacus TM301 is a compact and portable system designed to measure the purity of close environments, like a clean room, the counter is a system to measures the density of particles in open air. This system is based on a filter through which the air is forced to flow. Different kinds of filters are used sequentially to measure different sizes of particles centered at 0.3, 0.5, 1.0, and 5.0 μm according to the estimated dimension of dust and sand of the Sahara desert as described by Murdin (1985). A small pump placed inside the dome sucks the air and, through scattering the light from a laser diode, measures the number of particles. The four sizes of particles can be measured in both integrated and differential modes. Although the counter is mounted inside the TNG dome and at the level of telescope, a 1 m long silicon pipe through the wall feeds the pump to external air at 13 m above the ground. This is a needed precaution because, even if we intend to use the counter to monitor the external air, it must be kept in a closed site, safe from adverse weather conditions. Unfortunately, we cannot distinguish between the type of particles, but only their size. For instance, it is not possible to distinguish between water vapour and dust. For this reason it is necessary to stop the monitoring if relative humidity increases to the condensation point (typically $\geq$ 85%). Table 4.1 summarises the instrumental basic performances already reported in Porceddu et al. (2002) and also reported here for completeness.

4.3 Data analysis

The dust monitor measures outdoor dust at the same level as to TNG M1 to have a monitoring as close as possible the M1 local conditions. Data coming from Abacus TM301 are considered not as instantaneous values but as mean values after an integration time of 10 minutes. Before each measurement, a 5-minute long reset is used to clean the sensor. Abacus TM301 stores about 500 sets of data in memory, and when the memory is full, it

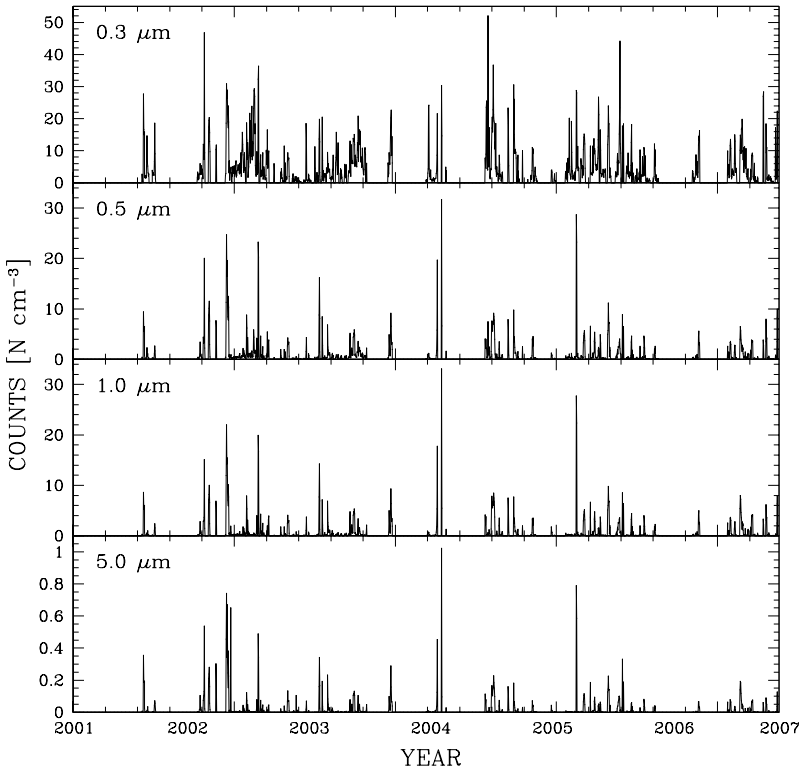

Figure 4.1: *Distribution of the atmospheric particles as a function of the different size, as measured by the Abacus TM301 during the years 2001-2006 (1-2 weeks each month depending on weather conditions). The gaps correspond to interruptions in the counter operations or to rejected values due to relative humidity* $> 85\%$.

uses an RS232 serial common port to transfer data to the PC for further analysis. Up to now the database collects measurements from August 2001 to December 2006, and it is used consecutively for 1-2 weeks each month depending to the weather conditions. In particular the counting is stopped if relative humidity $> 85\%$. In Figure 4.1 we report the full dust-count distribution for each particle size as measured during the years. The gaps in the figure corresponding to zero counts are caused by interruptions in the counter operations or by rejected values due to relative humidity $> 85\%$.

To check the presence of a seasonal variation, we split the dust database in two epochs, defining wintertime the months from October until March and summertime the months from April until September. In this analysis we define the dust storm event by each dust count having a value a few σ-levels over the monthly mean values. The background is evaluated using the σ-clipping algorithm also described in Huber (1981) and Patat (2003). The particle counts (N_i) were assumed to have a Poissonian distribution. For each month we computed the median value of the counts (MED), then for each different size of dust we calculated the median absolute deviation (MAD) defined as the median of the distribution

$$|N_i - MED|\,. \tag{4.1}$$

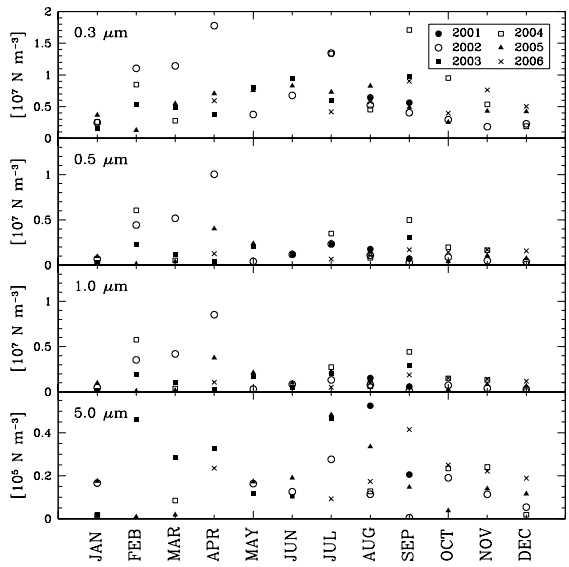

Figure 4.2: *Seasonal distribution of the monthly dust at ORM: (top) 0.3 μm dust; (middle-top) 0.5 μm; (middle-bottom) 1.0 μm dust; (bottom) 5.0 μm dust. Different years are indicated by different symbols.*

We set the σ parameter to the value $\sigma = 1.48\ MAD$ (according to Huber 1981), where 1.48 is the ratio between the standard deviation and the MAD under the assumption of a Gaussian distribution. During the iteration we rejected counts having

$$|N_i - MED| > K\sigma. \tag{4.2}$$

The procedure for estimating the dust background was iterated twice. In the first iteration we rejected the points exceeding $\pm 3\sigma$ with respect to the computed monthly median. In the second iteration, we rejected points exceeding 2σ and -3σ so that the background distribution is uncontaminated by any other dust peaks corresponding to dust storms.

We have found that, in connection with dust storms, counts of particles having diameters of 0.3, 0.5, and 1.0 μm increase by 2 orders of magnitude with respect to the background. Unfortunately 5.0 μm particles often present a typical fluctuation between 1 and 2 orders of magnitude, so it is difficult to distinguish dust storms from the typical dust background. For this reason an increase of 3 orders of magnitudes does allow us to distinguish the 5.0 μm peaks from the background.

Figure 4.2 shows the median monthly distribution of the particles as a function of the month. It is evident that the level of background depends on size. The distribution shows

Table 4.2: *Dust background content in [N m^{-3}] at ORM in wintertime, summertime, and in the entire annual cycle.*

	wintertime	summertime	annual
0.3 μm	$1.27 \cdot 10^6$	$4.38 \cdot 10^6$	$2.98 \cdot 10^6$
0.5 μm	$1.21 \cdot 10^5$	$3.76 \cdot 10^5$	$2.53 \cdot 10^5$
1.0 μm	$0.51 \cdot 10^5$	$1.51 \cdot 10^5$	$1.02 \cdot 10^5$
5.0 μm	$0.66 \cdot 10^3$	$1.47 \cdot 10^3$	$1.09 \cdot 10^3$

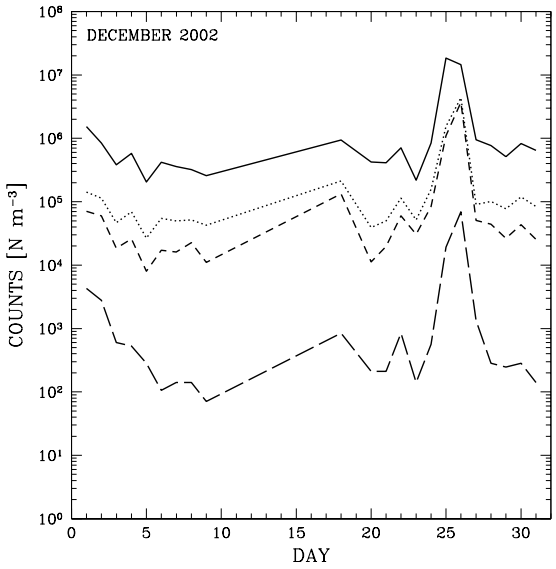

Figure 4.3: *Dust storm event of 2002 December 25 and 26: 0.3 μm (solid), 0.5 μm (dots), 1.0 μm (short-dashes) and 5.0 μm (long-dashes).*

Table 4.3: *Number of storm events at ORM in wintertime, summertime, and in the entire annual cycle in the period from August 2001 to December 2006.*

	wintertime	summertime	total
0.3 μm	10	8	18
0.5 μm	15	12	27
1.0 μm	21	22	43
5.0 μm	9	7	16

the increase in the counts during February-April and July-September, while May and June are the months with the lower level of dust.
Table 4.2 shows the median dust content as computed in the two seasons and in the entire annual cycle. The table clearly shows that small particles are dominant both in wintertime and in summertime. It is not surprising because heaviest particles decay quickly, while lighter particles flow in the atmosphere for longer.

4.4 Dust storms

As mentioned, we define dust storm as the event where the content of dust, given in counts per cubic metre [N m^{-3}], increases with respect to the typical dust background content in clear days by 2 orders of magnitude or more for 0.3, 0.5, and 1.0 μm dust, and 3 orders of magnitude or more for 5.0 μm dust. Figure 4.3 shows a more detailed situation of a dust storm that occurred in December 2002. This event persisted for two days, on 2002 December 25 and 26, and it shows an increase of several orders of magnitude in the counts.

In a deeper analysis we noticed that the dust storms are typically 3-4 days long, but sometimes it is possible to have some short storms 2 days long or, more rarely, long-lasting storms persisting 5-6 days. We correlated the wind direction with the dust-storm counts.

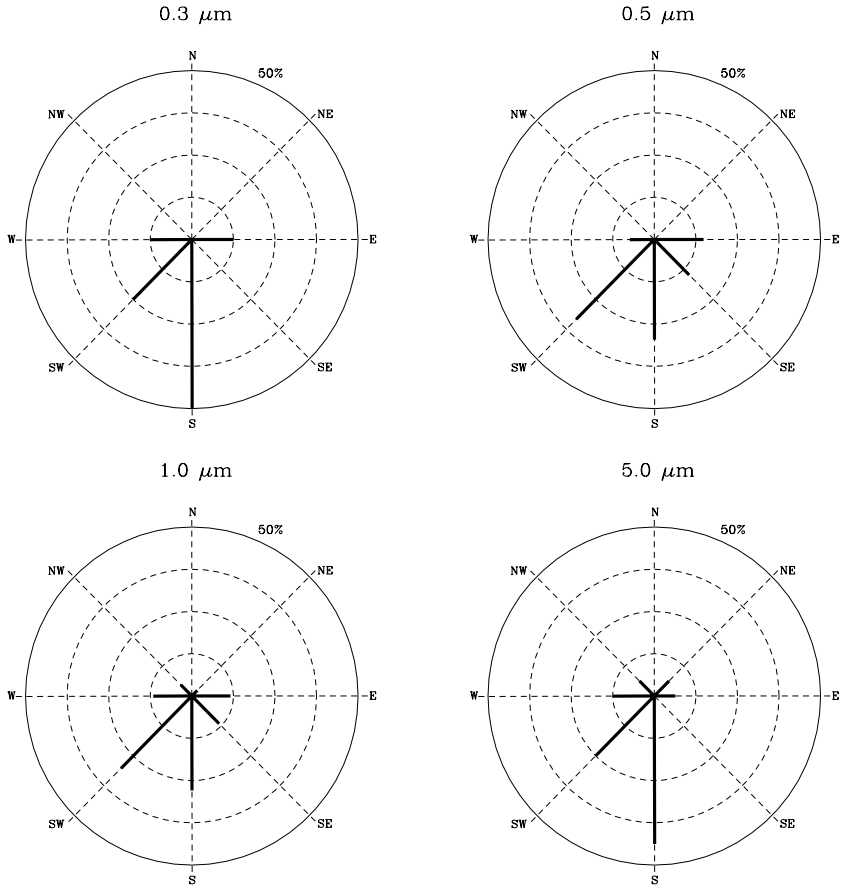

Figure 4.4: *Wind roses at TNG during dust storm events.*

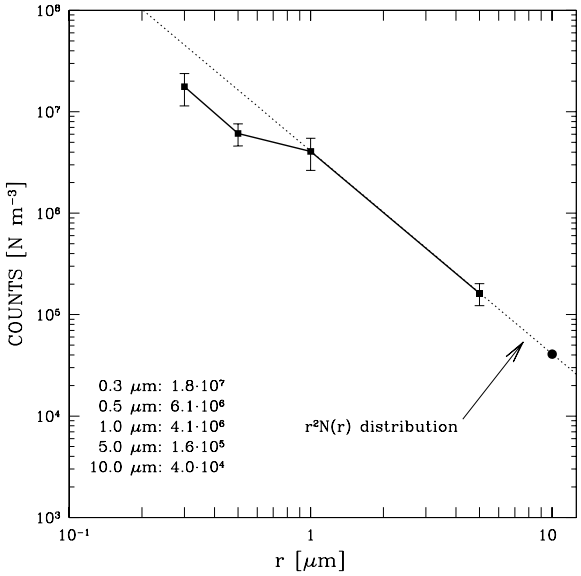

Figure 4.5: *Distribution of the median dust counts during dust storms. Particles* $\geq$*1.0* μ*m are treated as if they follow an* $r^2N(r)$ *power law.*

Figure 4.4 shows the wind roses obtained during the storm events as a function of particle size. The wind direction is recorded by the TNG meteorological tower and data were already analysed in the previous Chapter. There is a clear correlation between dust storms and wind direction. Only the winds blowing from south-west, i.e. from the edge of the Caldera de Taburiente, carry a large amount of dust particles. We confirm that the best photometric conditions occur when the wind blows from the north.
In Table 4.3 the total number of events for both wintertime and summertime in the period from August 2001 to December 2006 is reported. Particles having 1.0 and 0.5 μm size show the larger number of events. Table 4.3 shows that dust storms occur with the same statistic in both wintertime and summertime. Whittet et al. (1987) demonstrated that 95% of the aeolian deposits collected at La Palma have diameters between 1 and 100 μm. To better understand this analysis we calculated the median value of the dust content in case of storms for each measured size, and to include more massive grains we extrapolated the counts to 10.0 μm. Following Whittet et al. (1987), we assume a power-law distribution $r^2N(r)$ for particles $\geq$1.0 μm. Because we cannot distinguish between seasons, we decided to consider this background as a constant in both wintertime and summertime. Under these assumptions we found that 10.0 μm particles have a typical background of $\sim$10 N m^{-3} which is a lower concentration than the other particles we measured. The same power law permits us to extrapolate the concentration to the 10.0 μm size in case of dust storms. We obtained a concentration of $\sim 4 \cdot 10^4$ N m^{-3}. Results of this analysis are plotted in Figure 4.5.

4.5 Aerosol atmospheric extinction in B, V, and I

The optical properties of the dust in La Palma have been investigated by several authors. In particular, Stickland (1987) pointed out that extinction during dust storms is relatively stable on a time scale of 15 minutes. No analysis exists for the effects of the different dust sizes on astronomical extinction.
In this study we want to compare the differential extinction computed using our measured dust with simultaneous nighttime astronomical extinction obtained from the CAMC database, which is a very useful tool for quantitatively studying dust effects. We evaluate aerosol atmospheric extinction (k) for each size of dust at 3 different wavelengths: 435, 550, and 780 nm corresponding to the central wavelengths of the standard photometric bands B, V, and I. We believe that using the differential dust counter may help us evaluate the different extinction contributions from the different dimensions of the grains as a function of the wavelength.
The aerosol extinction is obtained by applying the model based on the Mie theory and has also been used by Mathis et al. (1977), Whittet et al. (1987), Jiménez et al. (1998), and Marley et al. (1999). The Mie theory assumes the particles are homogeneous spheres of radius r. Following Patterson (1977) definitions, the scattering coefficients for a Mie solution are linked to the size and composition of the particles through the parameter $x = 2\pi r/\lambda$. For an incident light at wavelength λ, the extinction coefficient k due to particles of radius r is defined by the formula

$$k_{\lambda,r} = Q_{ext}(n, r, \lambda)\, \pi r^2\, N \tag{4.3}$$

where the term $Q_{ext}(n, r, \lambda)$ is the *extinction efficiency factor* computed for Mie's particles, while N is the number of particles of radius r in a cubic centimetre. With this definition,

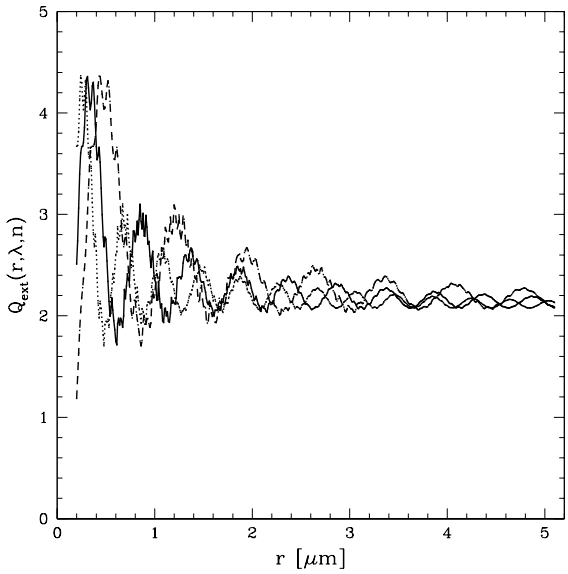

Figure 4.6: *Extinction efficiency factor as a function of the particles radius in B (dots), V (solid), and I (short-dashes).*

$k_{\lambda,r}$ is expressed in magnitudes per centimetre [mag cm^{-1}] and is correlated with the *local* density of the dust content in the atmosphere above the TNG dome.

In the equation, the extinction efficiency factor Q_{ext} is a complex function depending on the particles radius r, the absorbed wavelength λ and the complex refractive index n. In the definition (Patterson 1981), the real part of n is the ratio between light speed in a vacuum and the light speed in particles, while the imaginary part is related to the Bouguer absorption coefficient κ through the formula $n_{im} = \kappa\lambda/4\pi$. Following Patterson (1977), Carlson&Benjamin (1980), Fouquart et al. (1987), and Jiménez et al. (1998), we assigned $n = 1.55 - 0.005i$ ($i = \sqrt{-1}$) as the typical refractive index for Saharan dust aerosols.

We computed the extinction efficiency factor Q_{ext} for the adopted photometric bands using the Mie scattering code of Wiscombe (1980). Figure 4.6 shows the plot of Q_{ext} as a function of the particle radius for B, V, and I bands, while in Table 4.4 we report the computed values of Q_{ext} for 0.3, 0.5, 1.0, and 5.0 μm dust in the three bands. We show that for $r \geq 1.0$ μm, Q_{ext} is almost constant in the three bands, confirming that for massive grains the extinction is colour-neutral as pointed out by Jiménez et al. (1998).

Applying Eq. (4.3), we obtained the local aerosol atmospheric extinction in [mag cm^{-1}] caused by different grain sizes in typical dust background conditions (k_{MED}) and in the presence of dust storm events (k_{dusty}).

Table 4.4: *Values of the extinction efficiency factor Q_{ext}.*

	B	V	I
0.3 μm	4.148	4.334	2.783
0.5 μm	1.946	2.756	4.137
1.0 μm	2.367	2.355	2.205
5.0 μm	2.142	2.135	2.140
10.0 μm	2.072	2.084	2.099

Table 4.5: *Seasonal and annual local aerosol atmospheric extinction computed in dusty background conditions*[a].

	wintertime		
	$k_{MED}(B)$	$k_{MED}(V)$	$k_{MED}(I)$
0.3 μm	1.49	1.56	0.99
0.5 μm	0.19	0.26	0.39
1.0 μm	0.38	0.38	0.35
5.0 μm	0.11	0.11	0.11
10.0 μm	< 0.01	< 0.01	< 0.01
	summertime		
	$k_{MED}(B)$	$k_{MED}(V)$	$k_{MED}(I)$
0.3 μm	5.14	5.37	3.45
0.5 μm	0.58	0.81	1.22
1.0 μm	1.12	1.12	1.05
5.0 μm	0.25	0.25	0.25
10.0 μm	< 0.01	< 0.01	< 0.01
	annual		
	$k_{MED}(B)$	$k_{MED}(V)$	$k_{MED}(I)$
0.3 μm	3.49	3.65	2.34
0.5 μm	0.39	0.55	0.82
1.0 μm	0.76	0.76	0.71
5.0 μm	0.18	0.18	0.18
10.0 μm	< 0.01	< 0.01	< 0.01

[a] Values are given in [10^8 mag cm^{-1}].

Table 4.5 reports the k_{MED} in B, V, and I in wintertime, summertime, and in the entire annual cycle using data as reported in Table 4.2 and for the extrapolated value of dust background at 10.0 μm. As shown in the table, on clear days 0.3 μm dust gives the highest contribution to the global extinction, in particular in summertime. The extinction due to 0.3 μm dust is lower at higher wavelengths, while for 0.5 μm dust it becomes stronger at higher wavelengths, in particular in the summertime. Finally, the effect of the grains starting from 5.0 μm is almost constant in the three bands. We found that the contribution of the extinction due to 10.0 μm particles is negligible.

To understand the aerosol contribution on the total astronomical extinction, we need to evaluate the distribution in altitude of the particles. We compare our local extinctions in V to simultaneous astronomical extinctions in V from the CAMC database (k_{CAMC}) under the assumption that k_{CAMC} is mainly due to our measured dust. We assume

$$k_{aer}(\lambda) = k_{\lambda,0.3} + k_{\lambda,0.5} + k_{\lambda,1.0} + k_{\lambda,5.0} + k_{\lambda,10.0} \tag{4.4}$$

Because the CAMC-extinction database is only in V band, we compare our V band aerosol extinctions. For each $k_{aer}(V)$ we assume that particles are distributed in the atmosphere at an altitude h, in order to have

$$k_{aer}(V)\, h = k_{CAMC}(V). \tag{4.5}$$

We assume again that dust is uniformly distributed in altitude in a column of atmosphere having a base of 1 cm^2 and height h as obtained from Eq. (4.5). Figure 4.7 shows the distribution of the altitudes above the ORM obtained from each computed mean dust count. The maximum of the histogram shows the altitude reached by the dust. We found that the peak of the altitude distribution of the dust is about 2.5 km above the telescope. This value agrees very closely with studies based on independent radiosonde data (Hsu 1999)

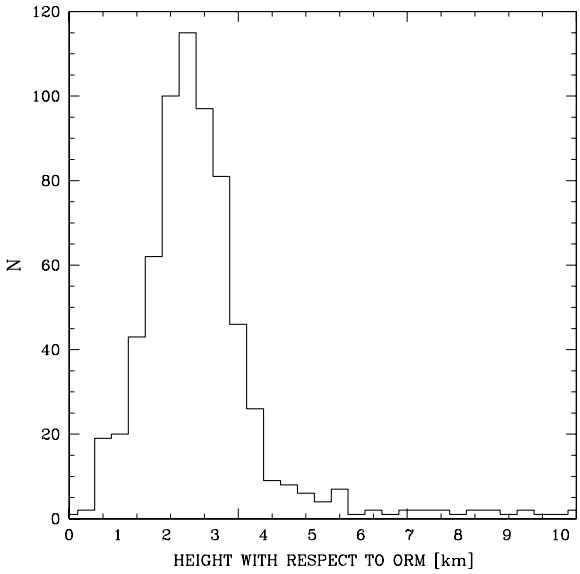

Figure 4.7: *Distribution of the dust altitudes from ORM altitude for Eq. (4.5).*

that found an height between 0.5 and 5.0 km depending on the season. Our results also indicates that the settlement process of the dust from the Sahara to La Palma, in the size range 0.3-10.0 μm, is not relevant, in agreement with the models of Murphy (1990). We conclude that, under the assumption of a uniform distribution of the dust, the particles are distributed in the first 2.5 km, on average. We then recompute the aerosol atmospheric extinction using Eq. (4.3), integrating on a column of atmosphere of 2.5 km. We assumed this obtained altitude to be equivalent to 1 airmass and the final extinction is therefore given in [mag airmass^{-1}].

The $k_{\lambda,r}$ for each particle size in typical dust background conditions and in typical dust storm conditions are now recomputed by integrating on a 2.5 km column of atmosphere above the TNG mirror. Figure 4.8 shows the aerosol atmospheric extinction $k_{\lambda,r}$ in [mag airmass^{-1}] and integrated on a column of atmosphere of 2.5 km in the entire annual cycle as a function of the size of the dust (cfr. Table 4.2 and Figure 4.5) for clear and dusty days. We show that on clear days, the extinction is dominated by 0.3 μm particles. Table 4.6 reports the percentage of contribution by different size of dust in each filter on both clear and dusty days. As shown in the table, on clear days 0.3 μm particles are responsible for more than 70% of the total aerosol extinction in B and V, while their contribution in I is about 60%. The biggest particles ($\geq$1.0 μm) dominate in dusty days. It is interesting to note the different behaviors of I band during dust storms with respect to the B and V bands. Bigger particles show a contribution to the total extinction of more than 70% in all the bands (see Table 4.6).

Following Eq. (4.4), the expected total local aerosol atmospheric extinction has to be calculated as the sum of the contributions of each particles size. On dusty days this extinction is typically $\sim$0.2 mag airmass^{-1} (see Figure 4.8) and can rise to $\sim$1.0 mag airmass^{-1} during very strong dust storms (see Figure 4.9). Figure 4.9 shows $k_{aer}(V)$ calculated on dusty days compared to simultaneous astronomical extinctions in V band as extracted from the CAMC database. Figure 4.9 shows a good correlation, the dotted line is the linear fit at

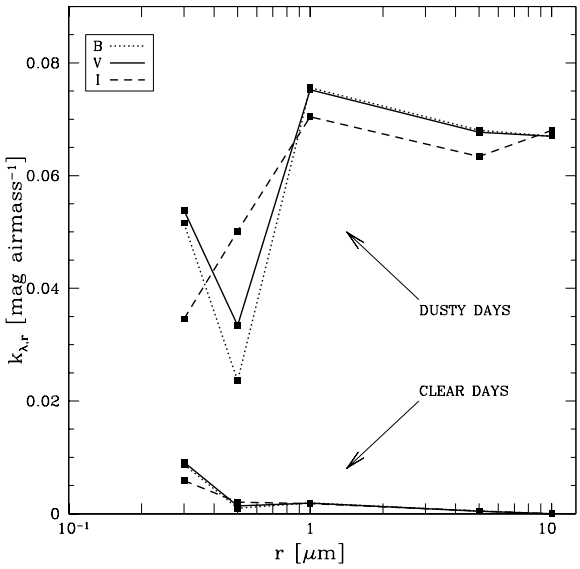

Figure 4.8: *Median aerosol atmospheric extinction in B, V, and I in typical dust background conditions and in typical dust-storm conditions for each particle size. The biggest particles are dominant with respect to sub-micron particles.*

Table 4.6: *Relative contribution of each particle size as percentage of the total aerosol atmospheric extinction k_{aer}.*

	clear days				
	0.3 μm	0.5 μm	1.0 μm	5.0 μm	10.0 μm
B	72	8	16	4	< 0.1
V	71	11	14	4	< 0.1
I	58	20	17	5	< 0.1
	dusty days				
	0.3 μm	0.5 μm	1.0 μm	5.0 μm	10.0 μm
B	18	8	26	24	24
V	18	11	25	23	23
I	12	17	24	23	24

a confidence level of 0.8 and having a slope of 0.77. We can conclude that it is possible to have an estimation of astronomical extinction, starting from a measure of dust count and by an appropriate calibration.

To evaluate the increase in the local aerosol extinction in connection with dust storm events, we also evaluated the differences between (i) the aerosol extinctions calculated on each day of a dust storm and (ii) the extinction calculated in the typical dust background conditions of each defined seasonal epoch:

$$\Delta k(\lambda) = k_{dusty}(\lambda) - k_{MED}(\lambda). \tag{4.6}$$

Figure 4.10 plots the mean increases calculated for each dust size in B, V, and I. In the figure we have also taken the extrapolated extinction due to 10.0 μm particles into account. The typical increases are between 0.015 and 0.065 mag airmass^{-1}.

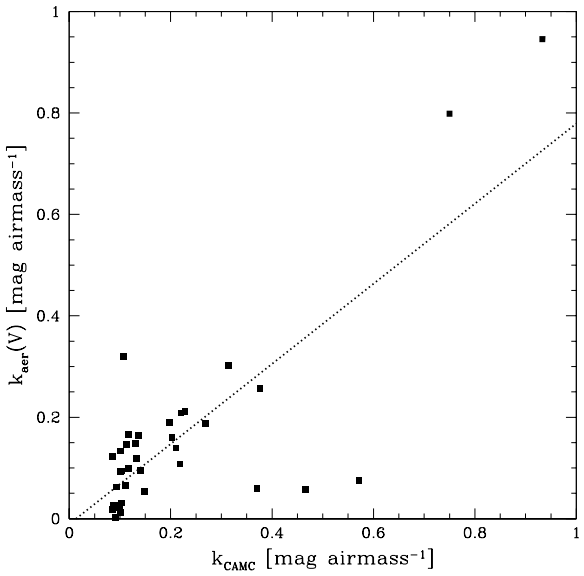

Figure 4.9: *k_{aer} versus k_{CAMC} in the case of dust storms. The linear fit has a confidence level of 0.8.*

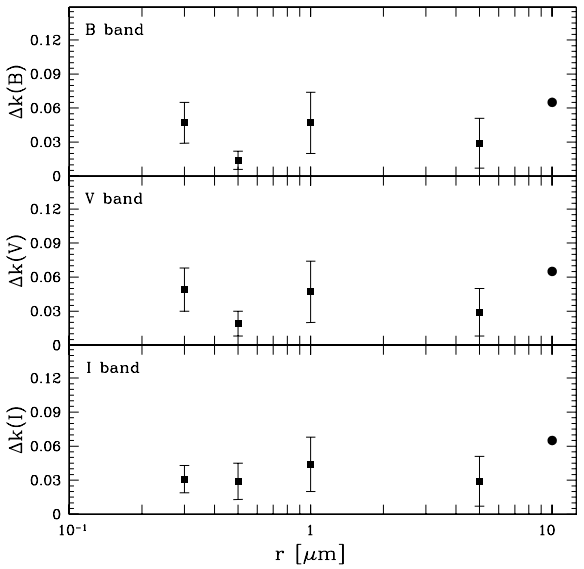

Figure 4.10: *Typical local aerosol extinction increases $\Delta k(\lambda)$ in [mag airmass^{-1}] in B (top), V (center) and I (bottom) in connection with dust storm events at ORM. The filled circles represent the expected $\Delta k(\lambda)$ due to 10 μm particles.*

4.6 Summertime aerosol atmospheric extinction and TOMS aerosol index

Recently the use of aerosol satellite data have been an useful technique for site characterization (Siher et al. 2004). TOMS database is one of the most accepted data to detect the daily aerosol content, but the management of satellite data need to pay a careful attention, in particular when compare tropospheric aerosol index (AI) and astronomical extinction.
The TOMS data are set with the data closest to the ORM within a 1×1 deg latitude and longitude box. TOMS AI is selected on the same days as $k_{aer}(\lambda)$. Following Siher et al. (2004) we have set our threshold at AI > 0.7. Because TOMS AI measurements above the Canaries are done in daytime, we obtained the nighttime AI by interpolating the values of two consecutive days. Satellite AI is obtained by the reflectivity effect. Because both dust and clouds may show reflectivity even at different threshold, we rejected AI points when sky reflectivity $> 15\%$ (Bertolin 2005) to be sure to have only the dust effect.
Once more we split the data between wintertime and summertime, and we noticed the absence of AI points in wintertime in connection with our local aerosol extinction calculations. Most of those points are the ones previously rejected for high sky reflectivity. In fact, in wintertime the sky is often contaminated by high reflectivity caused by thin cirrus or snow at the ground. Furthermore, in wintertime the dusts are often at low altitudes, too deep in the atmosphere to be revealed by the satellite.
Figure 4.11 shows the plot of the local aerosol atmospheric extinction in summertime versus the AI in V band (B and I show similar behaviours). In the plot we can distinguish three areas. The locus between the solid and short-dashed lines include all points having a correlation between $k_{aer}(\lambda)$ and AI with a confidence level > 0.8 (Spearman's test). The points below the short-dashed line show high AI but low local extinction. This high reflectivity is caused by the Saharan dust suspended at a very high level that is not detectable at the TNG mirror level. The (very few) points above the solid line show high local extinction and low AI. We ascribe the cause to local, recycled dust that remain suspended at low altitude and cannot be revealed by the satellite.
To support this affirmation, we computed the two wind roses for the data subsets relative to those days on which we believe that the extinction is due to local recycled dust, and on those days when the high reflectivity comes from the Saharan dust suspended in the high atmosphere. We found that, in the case of local recycled dust, the winds come prevalently from W-SW, while in the case of dust suspended in the high atmosphere the prevailing direction is from S-SW.
We can conclude that observations may often be affected also by local recycled dust and not only by Calima events. More data may help us this point. Taking all the reasons mentioned above into account we conclude that in site testing, both local dust monitors and data from satellites have to be used together for a complete investigation of the effects of the aerosols.

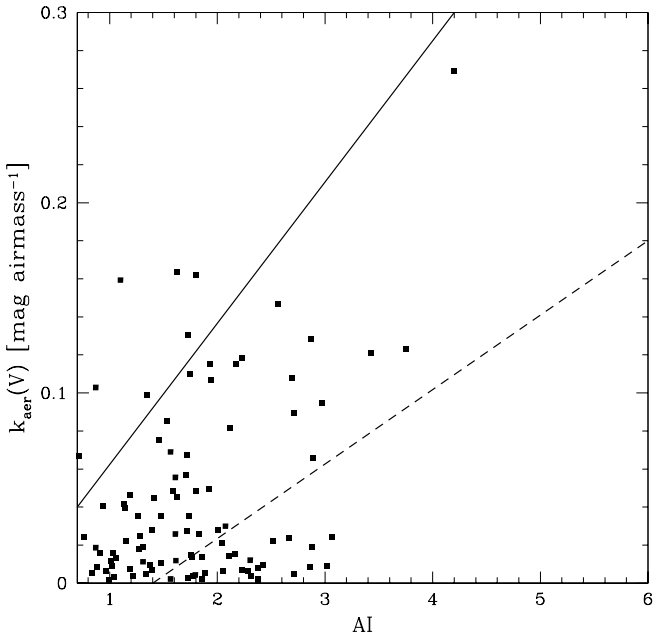

Figure 4.11: *Summertime local aerosol atmospheric extinction versus TOMS Aerosol Index in V band. The correlation calculated with the Spearman's test between the points inside the zone delimited by the solid and the short-dashed lines has confidence level* > 0.8.

Chapter 5

A study of the near-infrared atmospheric extinction on Paranal

Abstract

The dryness of the location makes Paranal a suitable observatory for near-IR observations. For this reason we want to characterize the extinction properties of Paranal in the spectral range 1.00-2.30 μm (J, J_S, H, and K_S) using an empirical method. The wavelengths of interest for this study correspond to the short-wavelength (SW) filters of the Infrared Spectrometer And Array Camera (ISAAC) at the Very Large Telescope UT1. We found that extinction coefficients are < 0.1 mag airmass^{-1} in all the considered bands.

5.1 Database and data reduction

Paranal observatory is characterized by very low humidity regimes (see Sections 3.8 and 3.9). This suggests very good characteristics of the site for near-IR observations. No study about the near-IR properties of the sky at Paranal exists up to now, so, in order to improve the knowledge of the atmospheric extinction at these wavelenghts, we have calculated the extinction coefficients using existing data from the calibration plan of the Infrared Spectrometer And Array Camera (ISAAC) at the Very Large Telescope UT1.
We use a 5 years long database of photometric Persson's standard stars (Persson et al. 1998) observed by ISAAC in J, J_S, H, and K_S during photometric and clear nights in the period from March 2000 to December 2004. Table 5.1 reports the ISAAC filters characteristics.
In IR photometric calibration standard stars have to be observed at least twice with a telescope offset in between, allowing for the sky to be subtracted. The Very Large Telescope domes are not equipped with calibration screens. For this reason, in imaging, twilight flats are the only possibility offered to ISAAC observers.
The images reduction is obtained using the ISAAC Pipeline and its fundamental package **eclipse** (ESO C Library Image Processing Software Environment). Each file is corrected from electrical ghosts generated by the detector, for dark and flat field.
Standard stars are imaged over a grid of five positions (one just above the center of the array and one in each quadrant). The pipeline founds the star (this one is approximately in the center of the first frame of five), computes the instrumental magnitude, and than determines the zero point (ZP) uncorrected for extinction.The final goal of this step is to

Table 5.1: *ISAAC SW imaging filters used in this study (the central wavelength varies slightly across the Field of View).*

Filter	Central Wavelength [μm]	Width [μm]	Width [%]
J	1.25	0.29	23
J_S	1.24	0.16	13
H	1.65	0.30	18
K_S	2.16	0.27	13

normalize the measurements of all standards observed at different time exposures (Amico et al. 2002; Cuby et al. 2004). Finally, the ZP is calculated using the conversion formula

$$ZP = M_{cat} + 2.5 \cdot \lg_{10}(F) - 2.5 \cdot \lg_{10}(DIT) \tag{5.1}$$

where M_{cat} indicates the catalog magnitude of the star (Persson et al. 1998) in the observed band, F the measured flux and DIT the Detector Integration Time.
Actually, the pipeline is still under a process of improvement, so programming and statistical reasons suggest that the computed zero point standard deviation (σ_{ZP}) is over estimated. For this reason we decide to consider as uncertainty of each computed ZP_i the value $\sigma_{ZP_i}/\sqrt{n}$, where $n = 5$ is the number of frames used by the recipe that compute the final object zero point. In order to produce an accurate analysis, points having $\sigma_{ZP_i} > 0.050$ mag are skipped from our sets of data.

5.2 Data analysis

Our database consists of 575 stars in J, 603 stars in J_S, 604 stars in H and 667 stars in K_S from the UT1 calibration plan. The zero points calculated from the images reduction shows a constant decreasing trend in time, between well defined time intervals (see Figure 5.1). A further inspection demonstrates that the intervals correspond to consecutive technical events concerning the telescope or ISAAC itself (Table 5.2). This means that the computed zero points are biased by deterioration of the telescope optics or instruments troubles. Furthermore, stars observed in the IR bands with different abundances of Precipitable Water Vapour (PWV) in the atmosphere are characterized by zero points that are biased with respect to the median PWV of the site (Manduca&Bell 1979).
In order to eliminate the mentioned bias we need to normalize our zero points for the effect of the evolution in time and for the different amount of water vapor in the atmosphere.

5.2.1 Evolution in time of the zero point

Figure 5.1 shows the evolution in time of the computed zero points in the four bands. The mentioned subsets (or periods), are delimited by two consecutive technical events, either a recoating of UT1 primary mirror (M1) or ISAAC technical intervention. A list of the events occurred between 2000 and 2005 is reported in Table 5.2.
Coating deterioration is mainly due to dust or oxidation and causes a progressive reduction of the mirror reflectivity, an increase in the thermal background emission (Frogel 1998) and a consequent ZP decrease. A change (increase or decrease) in the zero point trend is also consequents to ISAAC intervention as it may affect the instrument configuration. Our idea

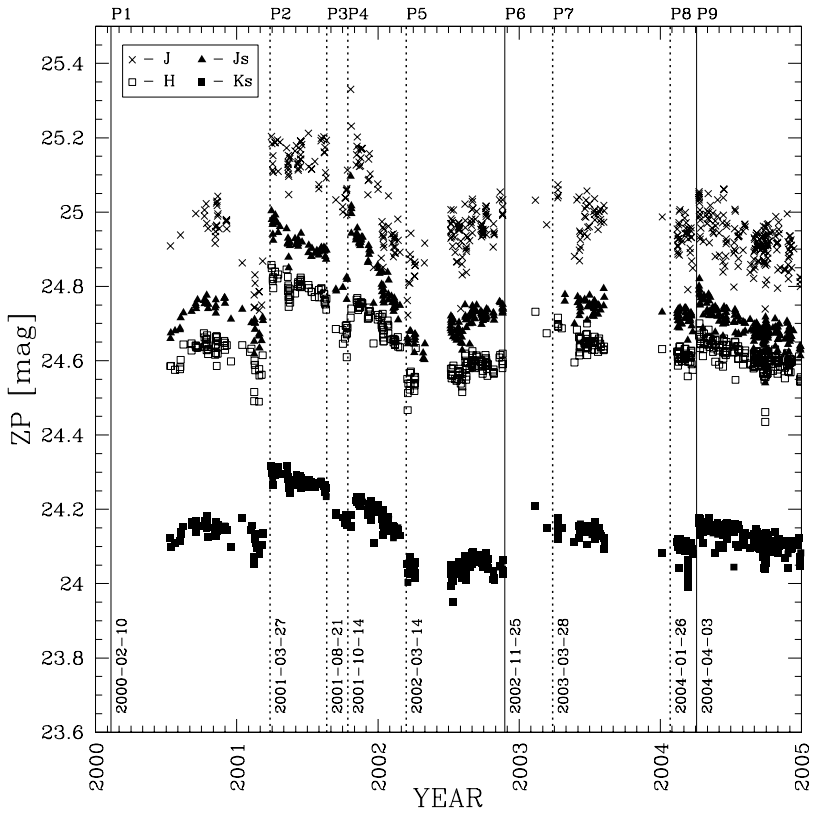

Figure 5.1: *Evolution in time of the zero point for J, J_S, H and K_S. The solid vertical lines indicate M1 recoating events, while dotted vertical lines indicate ISAAC interventions.*

is to consider separately each period and for each one of them we remove the ZP time trend by adding the linear fit of the zero point evolution in time to the ZP_i distribution: in practice we are simply normalizing the ZP to the value at the beginning of the considered period. The fit of the points in single subset represents the evolution in time of ZP and can be written as

$$ZP(t) = Ct + ZP_0 \tag{5.2}$$

where t is the time, ZP_0 correspond to the zero point at the beginning ($t = 0$) of the considered period, and C the slope of the fit. The differences $ZP(t = 0) - ZP_i$ are computed

Table 5.2: *Technical events occurred between 2000 and 2005.*

Item	Date	Event
P1	2000 02 10	M1 recoating
P2	2001 03 27	ISAAC intervention
P3	2001 08 21	ISAAC intervention
P4	2001 10 14	ISAAC intervention
P5	2002 03 14	ISAAC intervention
P6	2002 11 24	M1 recoating
P7	2003 03 28	ISAAC intervention
P8	2004 01 26	ISAAC intervention
P9	2004 04 03	M1 recoating

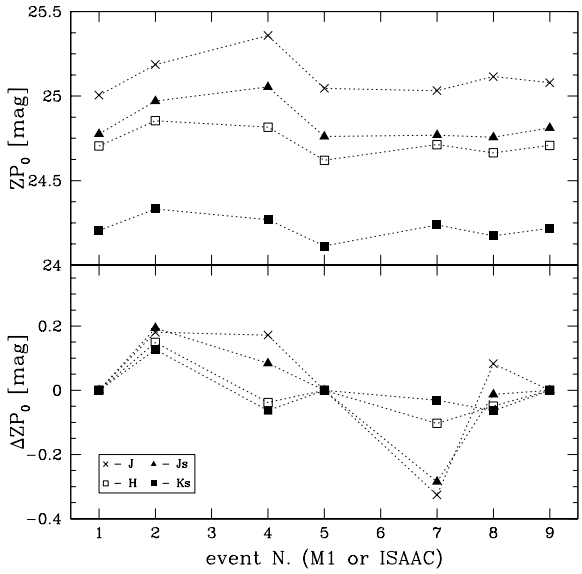

Figure 5.2: *(top) ZP_0 values after each event; (bottom) differences between $ZP_{0,N}$ and $ZP_{0,N-1}$.*

and added to each observed ZP_i. Periods P1, P5 and P8 have not been corrected for time evolution as there is not a clear trend of the ZP decreasing with time as expected. Furthermore, because of the presence of few points, P6 gives inaccurate fit. For this reason it will not be considered anymore in the analysis.
It is interesting to check the variation of the ZP_0 after each event. If the instrument intervention is not affecting the instrument performances, the ZP_0 values should be all identical. Figure 5.2 (top) shows the ZP_0 values after each event, while Figure 5.2 (bottom) shows the mutual differences between ZP_0 after two consecutive events, being $\Delta ZP_0 = ZP_{0,N} - ZP_{0,N-1}$. We indeed observe significant difference after each intervention, particularly after P2.

5.2.2 Effects of the Precipitable Water Vapour

The H_2O abundance above Paranal has been continuously monitored since July 2000 by an automatic station giving measurements with a precision of 10^{-3} mm sampled every 3 hours beginning at 00h UT.
Figure 5.3 shows the yearly trend of the PWV sampled at Paranal in photometric and clear nights. We note yearly periodic modulation with very high values (up to 13 mm in 2002) in the trimester January-March corresponding to the so called *Bolivian winter*. As shown in the figure, the resulting median PWV at Paranal in photometric and clear nights is 2.3 mm.
Increases in the H_2O abundance will make instrumental values of $(J - K_S)$ and $(H - K_S)$ blue because the effect of the atmospheric water vapour is stronger in K_S than in J and H (Frogel 1998).
We eliminate the bias introduced by different PWV by normalizing all ZP_i to the reference value of $PWV = 2.3$ mm. The correction is obtained by calculating the fit of the point in the space $[PWV, ZP]$ and flatting the fit at $PWV = 2.3$ mm. Thus, the correction applied

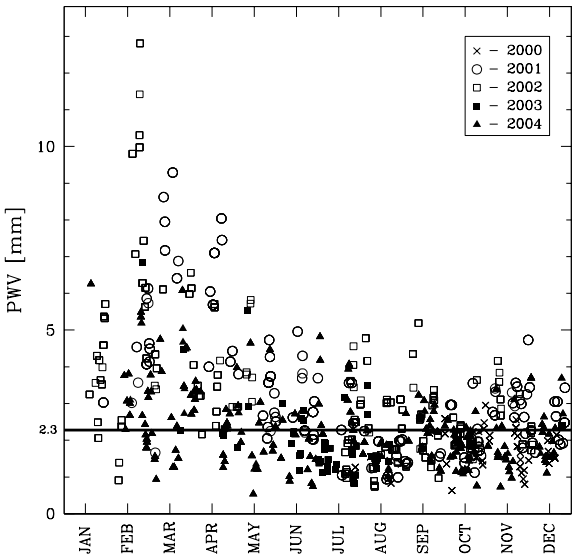

Figure 5.3: *Monthly trend of the PWV on Paranal in photometric and clear nights.*

to each point is

$$\Delta ZP_i = ZP_i + [ZP(2.3) - ZP(PWV_i)] \quad (5.3)$$

$$= ZP_i + ZP(2.3) - [a\,PWV_i + b] \quad (5.4)$$

where $ZP(PWV_i) = a PWV_i + b$ is the fit that describes how the ZP depends by the PWV.

5.3 Determination of the atmospheric extinction coefficients

We again consider all periods separately. The zero points corrected for the effects of the evolution in time and PWV-normalized are used in order to linear fit the Bouguer curves in the space $[X, ZP]$, where X is the airmass. The extinction coefficient (κ-coefficient hereafter) is the slope of the linear fit. The fits are calculated running two σ-clipping iterations and rejecting points exceeding $\pm 3\sigma$ with respect to the best fit. Examples for P9 of each band are shown in Figure 5.4, while Table 5.3 reports the calculated κ-coefficients for each band. We do not observe significant differences between the periods (see Figure 5.5). We consider the κ-coefficients calculated as the weighted average of the 8 available periods for each band and results are reported in Table 5.4 (column 2).

As a test we also computed κ-coefficients for each month having at least 5 standard stars observed. In this case the final extinction coefficients are obtained from the weighted average of the monthly determinations and the results are reported in Table 5.4 (column 3) and Figure 5.6. We do not observe significant variations between monthly and periods calculations. The κ-coefficients calculated with the monthly averages have smaller error-bars with respect to the periods ones. It is due to the fact that in the monthly case the computation is done on about 30-40 data points and not just on 8 as in the periods case. The weighted

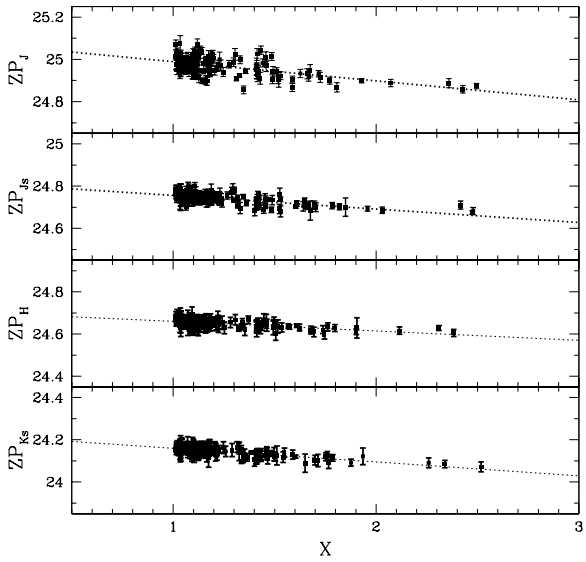

Figure 5.4: *Bouguer curves computed for P9 in each band.*

Table 5.3: *κ-coefficients in [mag airmass^{-1}] in different periods for J, J_S, H and K_S.*

Period	κ_J	κ_{J_S}	κ_H	κ_{K_S}
P1	0.064 ± 0.067	0.035 ± 0.032	0.066 ± 0.030	0.054 ± 0.026
P2	0.039 ± 0.043	0.000 ± 0.036	0.018 ± 0.028	0.020 ± 0.011
P3	0.167 ± 0.190	0.028 ± 0.488	0.157 ± 0.104	0.090 ± 0.054
P4	0.102 ± 0.035	0.055 ± 0.019	0.030 ± 0.010	0.019 ± 0.090
P5	0.083 ± 0.034	0.050 ± 0.025	0.034 ± 0.015	0.054 ± 0.013
P6	–	–	–	–
P7	0.041 ± 0.056	0.019 ± 0.028	0.027 ± 0.020	0.065 ± 0.011
P8	0.151 ± 0.064	0.031 ± 0.028	0.043 ± 0.026	0.055 ± 0.011
P9	0.092 ± 0.012	0.059 ± 0.006	0.043 ± 0.006	0.060 ± 0.005

averaged κ-coefficients calculated in the periods and monthly cases are compatible within the errors and a graphical illustration is reported in Figures 5.5 and 5.6 where they are represented by a solid line (periods case) and a dashed line (monthly case).
The absence of seasonal trends in the monthly κ-coefficients is due to the PWV normalization at 2.3 mm.

Particular care is necessary when the κ-coefficients (specially for J and J_S) are used for atmospheric extinction corrections between 1 and 2 airmasses because the extinction coefficients can be under estimated of about 15-30% (Manduca&Bell 1979). The underes-

Table 5.4: *Weighted averaged κ-coefficients for J, J_S, H and K_S for periods and monthly cases.*

Band	κ (periods) [mag airmass^{-1}]	κ (months) [mag airmass^{-1}]
J	0.089 ± 0.010	0.081 ± 0.006
J_S	0.054 ± 0.005	0.060 ± 0.004
H	0.039 ± 0.005	0.042 ± 0.003
K_S	0.055 ± 0.004	0.061 ± 0.002

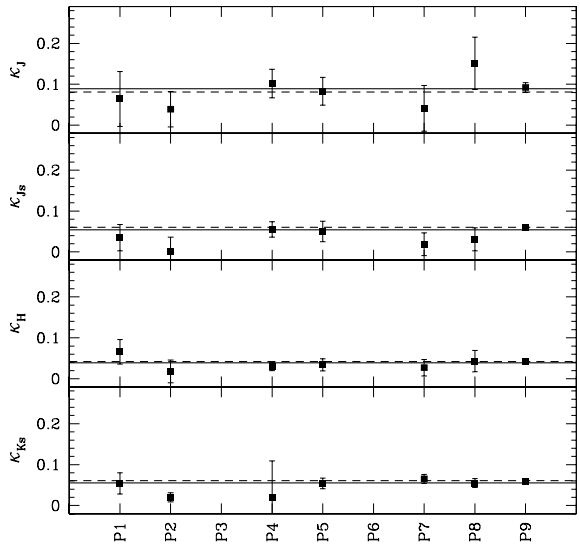

Figure 5.5: *κ-coefficients in [mag airmass^{-1}] for J, J_S, H and K_S in different periods. The weighted averages are also reported: (solid line) periods case; (dashed line) monthly case.*

timation is due to the linear extrapolation at $X = 0$ that induces an error that depends on the H_2O column abundance above the site and the color of the observed objects (see Figure 2 in Manduca&Bell 1979). A "square root law" extrapolation at airmass 0 (Johnson 1965) results inadequate because gives an huge over estimation of the κ-coefficients ($> 100\%$) (Manduca&Bell 1979). In general, no simple rule exists for an adequate extrapolation at airmass 0. Manduca&Bell (1979) indicate a maximum error of 15-30% in the κ-coefficients when used for corrections between 1 and 2 airmasses as an acceptable compromise.

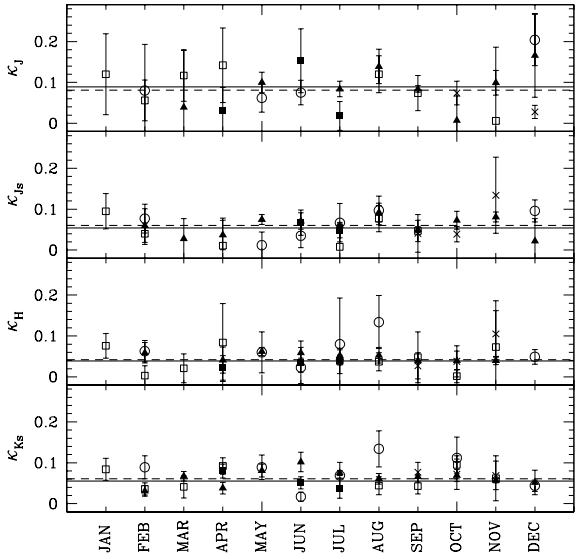

Figure 5.6: *Monthly extinctions in [mag airmass^{-1}] (different years have different symbols). There is no evidence of a seasonal trend. The weighted averages are also reported: (solid line) periods case; (dashed line) monthly case.*

Chapter 6

Measuring the turbulence

Abstract

In this Chapter is briefly described the theory of a set of instruments that I have used in combination for Paranal site monitoring and E-ELT site selection campaigns: the Differential Image Motion Monitor (DIMM), the Multi-Aperture Scintillation Sensor (MASS) and the SLope Detection and Ranging (SLODAR). Information provided by these instruments are presented in the following Sections.

6.1 The Differential Image Motion Monitor (DIMM)

In the years '80, after the knowledge of the theories of the perturbations of the incoming wavefront, several new techniques based on the wavefront sensing method, provided quantitative information on seeing (Roddier 1981). Some techniques, such as star trail photograph and photoelectric image motion monitors, provide information sensitive to tracking errors, while interferometers techniques shown to be affected in adverse and dusty environments. Therefore, at the end of 1984, ESO decided to develop a new instruments free from the limitations explained above: the Differential Image Motion Monitor (DIMM).
The DIMM started its observations in Paranal in 1988 in connection with the Very Large Telescope site testing campaign. The instrument measures wavefront slope differences over two small pupils some distance apart, caused by the atmospheric turbulence. This measurement of distortion is then converted into an estimate of the image size (seeing FWHM) it would correspond to on a large telescope, using the Kolmogorov-Fried model (Sarazin&Roddier 1990).
Schematically, the instrument is composed by a small telescope (typically between 35 and 40 cm) observing a single bright star. On the entrance pupil, the starlight passes through a mask having two holes of diameter D at distance d (Hartmann holes), symmetric with respect to the center of the pupil, in order to obtain dual star images (spots) whose relative motion in the image plane represents local wavefront tilts. The re-imaging of the entrance pupil is obtained by a collimator and a prism in the image plane introducing a symmetrical tilt in the direction parallel to the holes separation (Sarazin&Roddier 1990). A schematic example is shown in Figure 6.1.
Longitudinal and transversal (in the direction of the prism tilt) seeing FWHM are calculated from the longitudinal and transversal covariance of the spots separation derived on

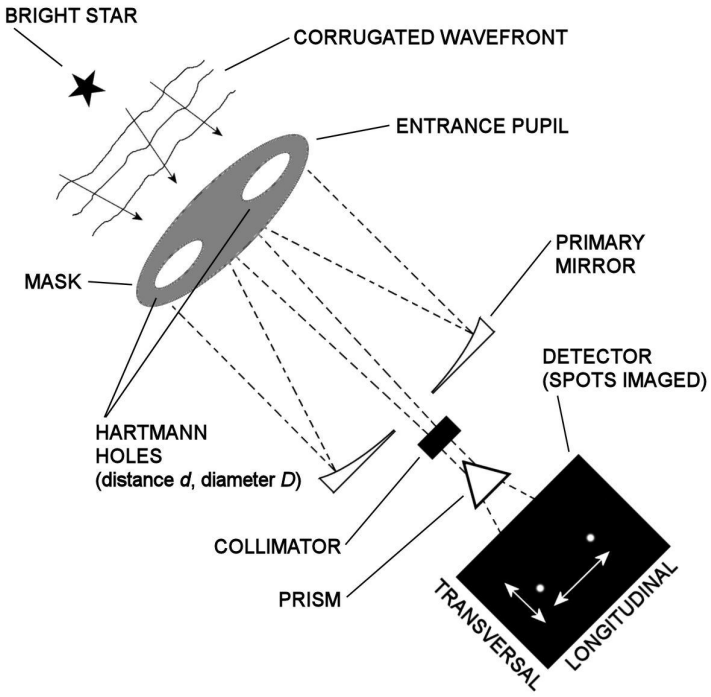

Figure 6.1: *A simple scheme of the DIMM layout (interpretation from Sarazin&Roddier 1990).*

the image plane. The final seeing estimation is the average of the longitudinal and transversal FWHM. Since the method is differential, it is not affected by vibrations of the mount system, shaking due to wind and tracking errors.
The calculated seeing represents the total turbulence energy (C_n^2) in the column of atmosphere observed by the DIMM corrected at airmass 1.

6.2 The Multi-Aperture Scintillation Sensor (MASS)

The MASS measures the vertical distribution of the energy of the atmospheric turbulence in the high atmosphere by analyzing the scintillation[1] of a bright star. It consists of an off-axis reflecting telescope and a detector unit which measures the scintillations of single stars in four concentric zones of the telescope pupil using photo-multipliers. A statistical analysis of these signals yields information of the vertical profile of the turbulence ($\langle C_{n,M}^2(h)\rangle$ in $[\mathrm{m}^{-2/3}]$).
The method uses the connection between the distance of a turbulent layer and its effects on the spatial scale of the light variations due to the scintillation. The light from the star is collected on an four concentric-ring mirror apertures acting as a spatial filter (a simple scheme is shown in Figure 6.2). The dependence between the layer distance and scintillation is used to separate the contributions from different layers. The distribution of the turbulence in altitude is calculated from the statistical processing of the series of photon counts within each sub-aperture ring with 1 ms sampling (Tokovinin&Kornilov 2002).

[1] See Section 2.8

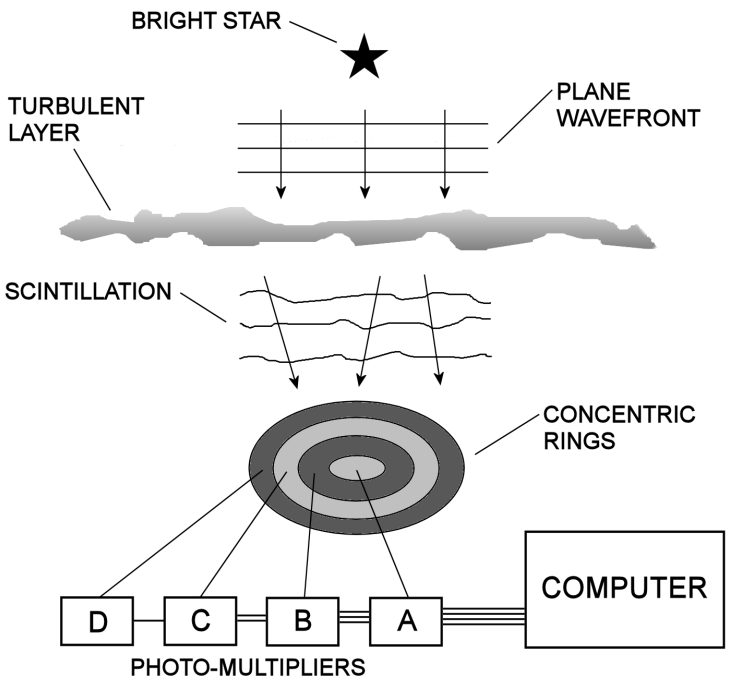

Figure 6.2: *A simple scheme of the MASS concept (interpretation from Tokovinin 2008).*

Each ring mirror aperture, called A, B, C and D in Figure 6.2, converges light to four photon counters. In the method both the *scintillation index* (SI) and the *differential scintillation index* are retrieved. The scintillation index in each aperture is computed as the variance of intensity normalized by the average intensity squared (thus, SI is not dependent on the star brightness, but only on the strength of the scintillation). The differential scintillation index for two apertures (i.e. A and B) is defined as the variance of the ratio of intensities in A and B normalized by the square of the average intensity ratio A/B (Tokovinin&Kornilov 2002).
Both indexes are calculated as the product of the turbulence energy in a given layer and the corresponding instrumental weighting function relative to that layer. Thus, the $C^2_{n,M}(h)$ of each layer is calculated inversely.
The MASS is operating at Paranal since 2003 and gives the $C^2_{n,M}(h)$ corrected at airmass 1 for 6 layers placed at 0.5, 1, 2, 4, 8 and 16 km above the telescope pupil. The scintillation is mostly produced by layers at high altitudes in the atmosphere, therefore measurements of layers below 500 are poor. The DIMM may compensate this limitation, indeed the combination of a DIMM and a MASS gives the possibility to measure both seeing and low-resolution turbulence profiles from the ground.

6.2.1 MASS weighting functions

The MASS weighting functions can be assumed as triangles having the peak in correspondence of the layer specific altitude h_i (Figure 6.3). In another way we can affirm that the peak corresponds to the altitude in which the MASS has the maximum sensitivity to the signal. The altitudes and the bases of each weighting function are fixed on a 2^n logarithmic

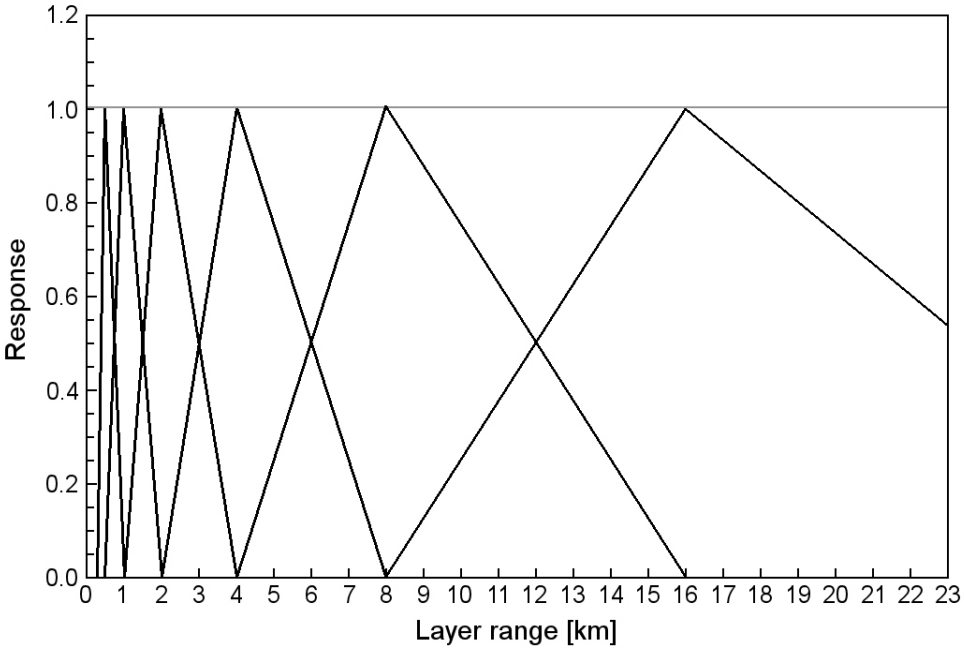

Figure 6.3: *MASS weighting functions.*

Table 6.1: *MASS weighting functions extremes definition at Paranal (in [m]).*

Layer	h	Δh	min_i	max_i
1	500	750	250	1000
2	1000	1500	500	2000
3	2000	3000	1000	4000
4	4000	6000	2000	8000
5	8000	12000	4000	16000
6	16000	24000	8000	32000

grid. The six altitudes are expressed by the formula

$$h_i = 2h_{i-1} \tag{6.1}$$

where $i = 1, 2, ..., 6$ and $h_1 = 500$ m. The width of the base of each triangle, assumed as the thickness (Δh_i) of the sensed layer, is defined by the formula

$$\Delta h_i = 2h_i - \frac{h_i}{2} = \frac{3}{2}h_i \tag{6.2}$$

where $2hi = max_i$ and $h_i/2 = min_i$ correspond respectively to the two extremes of the base. Table 6.1 reports the altitude, the base width and the base extremes for each layer sensed by the MASS operating at Paranal. As one can argue from the table, the resolution of the profile decreases as $1/\Delta h_i$, but the relative resolution $\Delta h_i/h_i$ is constant for each layer.

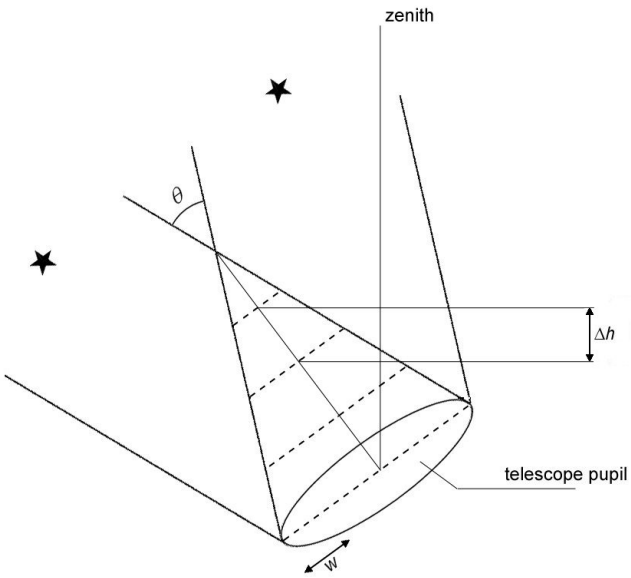

Figure 6.4: *A simple scheme of the SLODAR concept.*

6.3 SLope Detection And Ranging (SLODAR)

The SLODAR is a method developed by University of Durham (Wilson 2002) for measurement of the strength, altitude and motion of the atmospheric turbulence in the ground layer. In site characterisation it allows to predict anisoplanatism and fractional sky coverage in the design of adaptive optical systems for astronomy. The instrument is powerful also in the real-time optimization of adaptive optics applications.
The SLODAR instrument has operated in several runs at Paranal in 2005, 2006, 2007 and 2008. It uses an optical triangulation method for the measurement of the atmospheric turbulence profile in the ground layer. The profile is determined from the spatial covariance of the slope of the wavefront phase aberration at the ground for the two different paths through the atmosphere defined by a double star target observed using a Shack-Hartmann (SH) wavefront sensor (Butterley 2006).
The double star projects the wavefront aberration produced by the turbulent layer at altitude h onto the ground. Thus, there is a peak in the cross-correlation function of the wavefront slope for a generic spatial offset w (i.e. the sub-aperture of the SH). The energy of the turbulence in a given layer (corrected at airmass 1) is related to the amplitude of the cross-correlation signal. The altitude is given by a simple triangulation, having the binary star separation θ[2]. A schematic example is shown in Figure 6.4.
The number of layers sensed by a SLODAR instrument depends on the number of the sub-apertures of the SH wavefront sensor. In the case of the SLODAR used at Paranal, the SH is a 8×8 lenslet array, therefore 8 different layers in the ground layer are sensed by the instrument.

[2]For more details see http://www.cfai.dur.ac.uk/new/rd/SLODAR/SLODAR.html

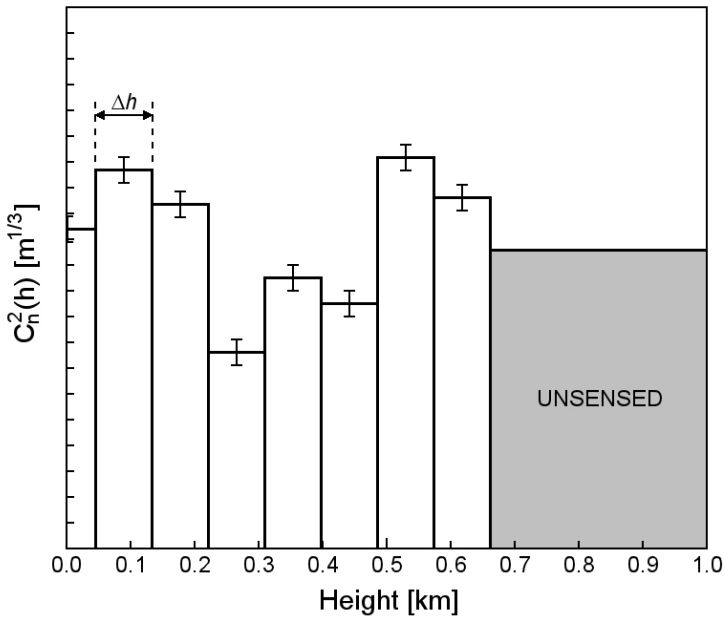

Figure 6.5: *A simple scheme of the SLODAR layers.*

6.3.1 SLODAR weighting functions

When compared to MASS ones, the SLODAR weighting functions are subtler of at least 2 orders of degree. In fact their thickness varies between ∼50 and ∼100 m depending on the zenithal distance (z) of the observed double star. For this reason we consider them as rectangles centred in the sensed layer altitude (see Figure 6.5). The base of the rectangles, corresponding to the thickness of the layers, is the same for each layer and depends by the angular separation of the observed binary system and the Shack-Hartmann sub-aperture (w) by the formula (see Figure 6.4)

$$\Delta h = \frac{w}{\theta} \tag{6.3}$$

Δh also depends on the zenithal distance of the binary by the secant of z. During the observations z changes continuously, thus also Δh changes at the same time. The SLODAR operating at Paranal gives measurements every minute, so both altitudes of the layers, their thickness and the restored profile change every minute of a small amount. The first layer is centred at $h = 0$, so an half of its thickness is at negative altitude. In this way the total height of the low atmosphere profiled by the SLODAR is $H = 8\Delta h - \Delta h/2 = 7.5\Delta h$ (see Figure 6.5). The residual $C_{n,S}^2$ above H is the difference between the total $C_{n,S}^2$ and the sum of $C_{n,S}^2(h_i)$ for the 8 sensed layers and is defined as *unsensed* $C_{n,S}^2$ ($Cu_{n,S}^2$).

Chapter 7

Combining turbulence profiles from MASS and SLODAR

Abstract

The present Chapter describes the algorithm used in simultaneous measurements of atmospheric turbulence profiles using a DIMM, a MASS, and a SLODAR. The described technique allows the restoration of unified profiles from the surface (or platform) of an observatory up to the high atmosphere.

7.1 The reason to combine profiles from different instruments

Typically the height of the atmosphere worsening the seeing is supposed ranging between 0 and 20 km and can be represented as a collection of several independent layers. The atmospheric turbulence profile is known if there is a good estimation of the amount of energy in each layer, therefore if it is known the contribution of each layer to the total seeing. This is crucial in the calibration of Adaptive Optics systems, in particular the knowledge of the strongest turbulent layers is decisive in the choice of the conjugation layers in Multi-Conjugated Adaptive Optics (MCAO).
As already mentioned (Section 6.2), at Paranal the MASS gives the atmospheric turbulence profiling for 6 layers placed at 0.5, 1, 2, 4, 8 and 16 km above the telescope pupil of the MASS[1], while the SLODAR provides ground layer profiles[2] of 8 layers with a resolution that can vary between few tens of meters up to 100 m, depending on several parameters such as the separation of the observed binary system, the width of the wavefront lenslet array sub-apertures and the zenithal distance of the observed binaries (Section 6.3). In this way we collect the information about 8 thin layers in low atmosphere from SLODAR and 6 layer in the high atmosphere from MASS.
The combination of the profile from SLODAR and the simultaneous one from MASS allows us to have the turbulence profile of the entire atmosphere.

[1]DIMM and MASS at Paranal are installed on two dedicated telescopes 6 m above ground.
[2]SLODAR at Paranal is installed on a dedicated telescope at ground level.

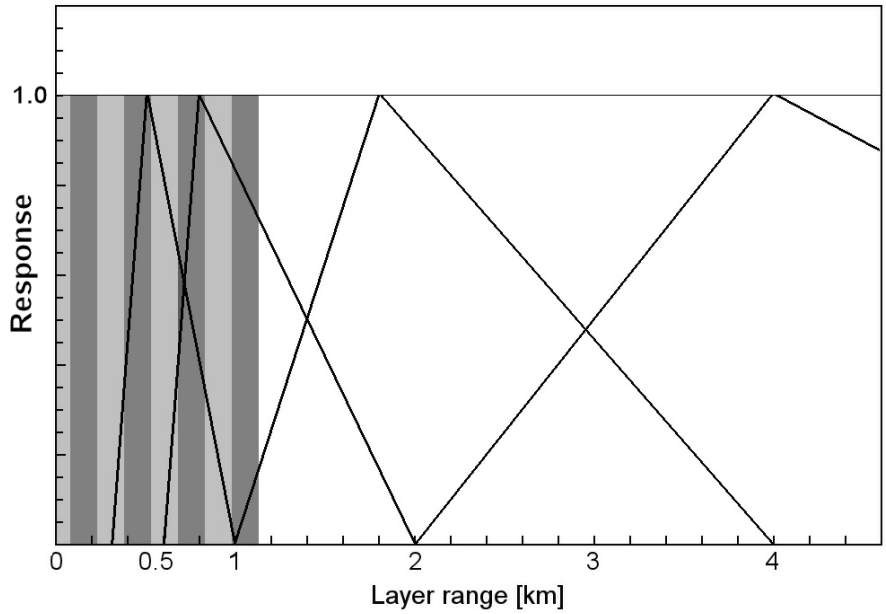

Figure 7.1: *En example of superimposition of SLODAR and MASS layers.*

7.2 The problem of the weighting functions

The knowledge of the MASS and SLODAR weighting functions is crucial to correctly combine their profiles, since they have different profiles restoration (see Sections 6.2.1 and 6.3.1). The crucial point is introduced if the SLODAR layers thickness Δh is big enough to have the upper part of the low atmosphere sensed by the SLODAR superimposed the lower part of the atmosphere sensed by the MASS (Figure 7.1). But Δh is changing continuously within the zenithal distance of the observed star having as consequence a continuous changing of the superimposed area. This enforce that the interpolation method of the two profiles must be flexible according to the kind of overlap between MASS and SLODAR.

7.3 The method

The first step is the transformation of the triangular functions of the MASS into rectangular ones compatible with the SLODAR (see Figure 7.2). The process must be conservative, that means to maintain the final rectangular area, proportional to its energy, of the same value of triangular one. Considering Table 6.1 and Figure 7.2 (top), being $\langle C^2_{n,M}(i)\rangle$ the energy of a generic i-th MASS layer in $[\mathrm{m}^{-2/3}]$, the area is

$$A_i = (max_i - min_i)\,\frac{\langle C^2_{n,M}(i)\rangle}{2} \tag{7.1}$$

and represents the integral $C^2_{n,M}(i)$ of the turbulent energy in $[\mathrm{m}^{1/3}]$. The extremes of each rectangular layer are defined as the contact points of two consecutive triangles. The geometrical nature of the weighting functions lets the contact point of two adjacent triangles i-th and $(i+1)$-th to be placed in the middle between max_i and min_{i+1}. In fact, the negative slope of the i-th layer and the positive slope of the $(i+1)$-th layer are symmetric (Figure

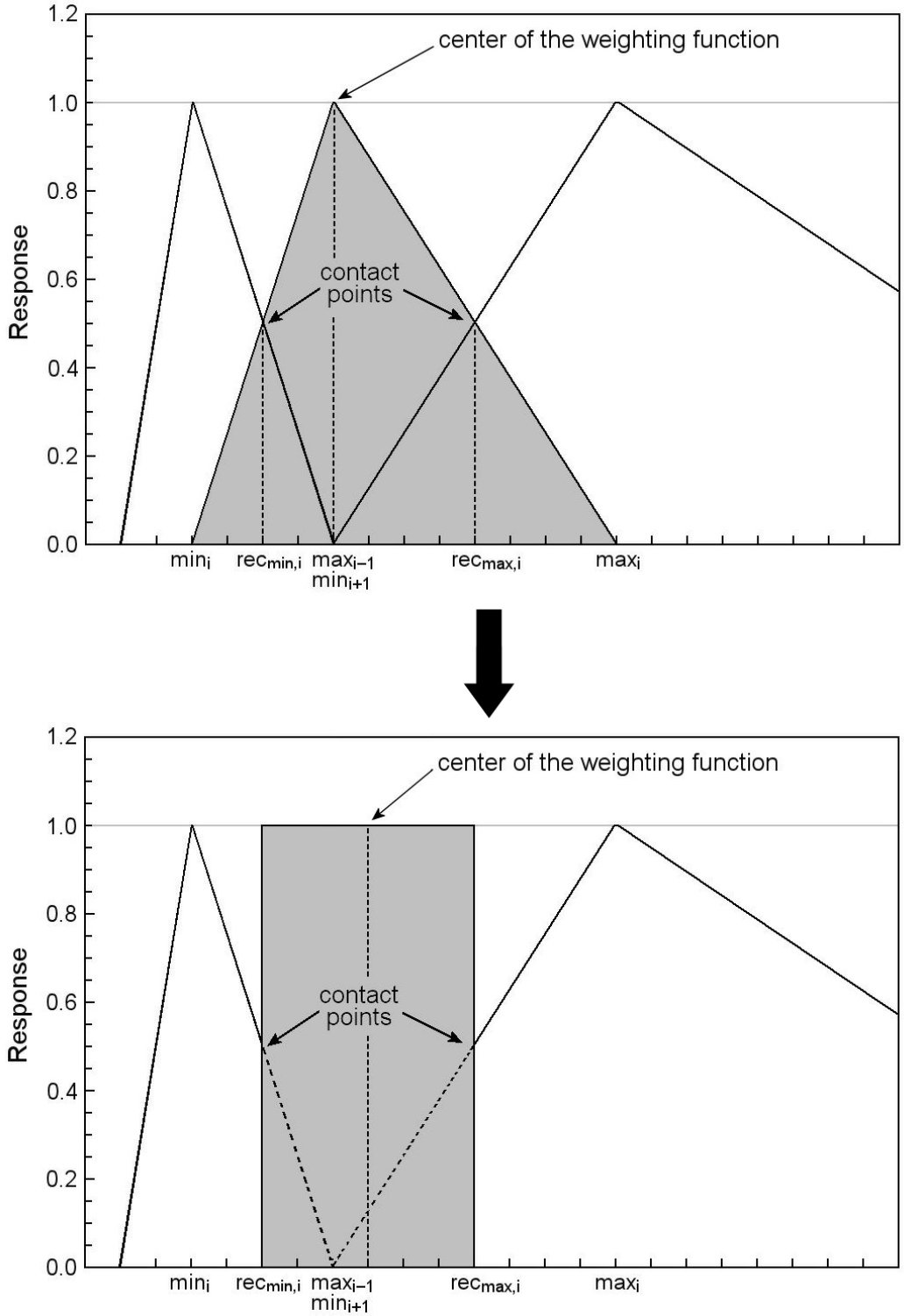

Figure 7.2: *Transformation of the MASS triangular weighting functions (top) into rectangular ones (bottom) compatible with SLODAR.*

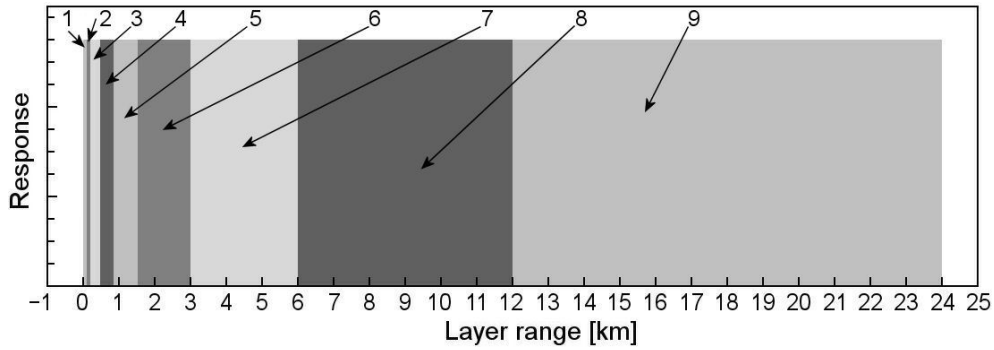

Figure 7.3: *A qualitative scheme of the new unified grid of layers.*

7.2, top). In this way each rectangle results to be confined inside the following limits

$$rec_{min,i} = min_i + \frac{max_{i-1} - min_i}{2} \tag{7.2}$$

$$rec_{max,i} = min_{i+1} + \frac{max_i - min_{i+1}}{2} \tag{7.3}$$

and the center of the new layer is

$$h_{rec,i} = rec_{min,i} + \frac{rec_{max,i} - rec_{min,i+1}}{2} \tag{7.4}$$

In this way we have established a mathematical process that define a grid of new rectangular layers distributed within a 2^n logarithmic scale similarly to the MASS. The definition can be extended uniformly from the ground to the high atmosphere and give us a new unified grid of layers (or *bins*, see Figure 7.3) which extremes are reported in Table 7.1. The first bin is arbitrarily defined taking into account the maximum resolution of the SLODAR, in fact beyond this limit the layers are not resolved.

In our assumption the sum of the layers 1, 2 and 3 represents the *ground layer* (GL) that extent between the ground and 375 m according to Table 7.1. The sum of the layers 4, 5, 6, 7, 8 and 9 derived from the MASS define the *high* (or *free*) *atmosphere* (FA), that extents between 375 m to 24 km (see Figure 7.4).

Table 7.1: *Definition of the extremes of the new unified grid of layers.*

	Layer	h	Δh	min_i	max_i	
	1	47	94	0	94	*unified ground layer*
GL	2	140	94	94	188	*extending from 0 to 375 m*
	3	281	188	188	375	*and centered at 188 m*
	4	562	375	375	750	
	5	1125	750	750	1500	
FA	6	2250	1500	1500	3000	*unified free atmosphere*
	7	4500	3000	3000	6000	*extending from 375 m to 24 km*
	8	9000	6000	6000	12000	
	9	18000	12000	12000	24000	

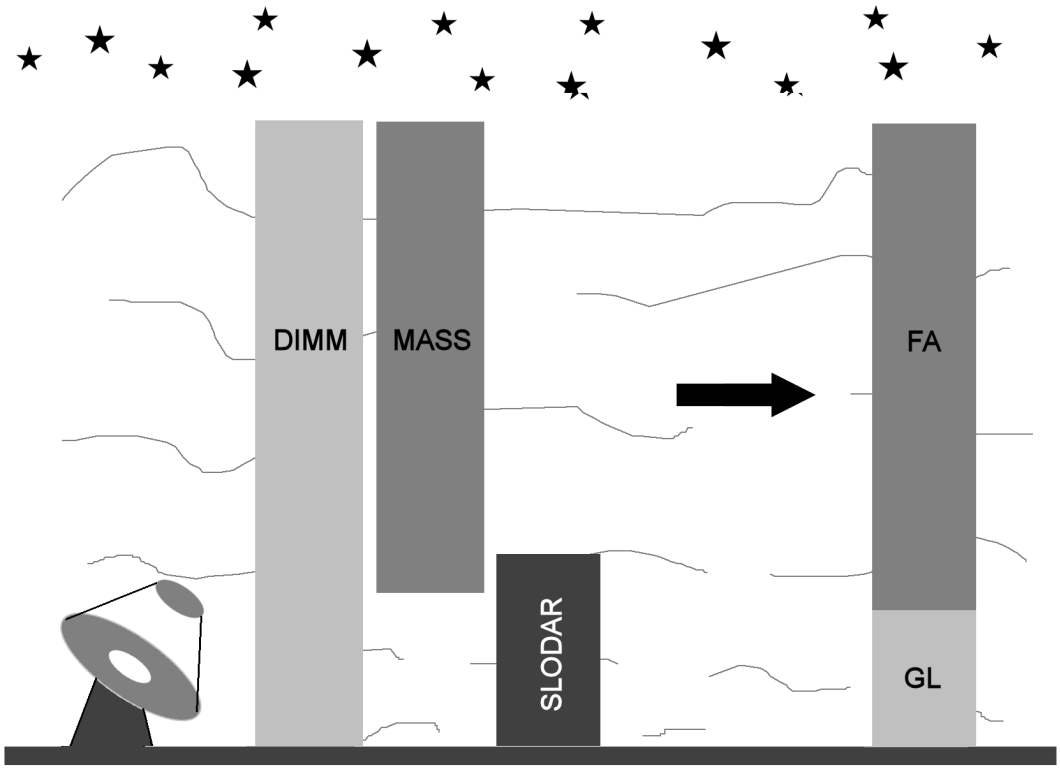

Figure 7.4: *A schematic representation of the atmospheric coverage of DIMM, MASS and SLODAR sensing. The representation of the recombined profile is also shown.*

Finally, for what concerns the rectangular layer originated from the MASS transformation, their height, that must be proportional to the original energy $C_n^2(h_i)$, is calculated as

$$height_i = \frac{A_i}{rec_{max,i} - rec_{min,i}} \tag{7.5}$$

7.3.1 Restoration of the turbulence profile

We assume that the turbulence is uniformly distributed in each layer of the new defined grid. Bins 1, 2 and 3 correspond to the ground layer and we *fill* them starting from the first using the 8 SLODAR layers energies $C_{n,S}^2(i)$. In principle, the high atmosphere is already set using the 6 $C_{n,M}^2(i)$ of the MASS, and we will need to normalize the SLODAR $C_{n,S}^2(i)$ to the simultaneous total C_n^2 of the DIMM. In this way the recombination is conservative, because *no energy must be added or subtracted in the restoration.*
Particular care must be used when the Δh of the SLODAR layers is big enough and also the bin number 4, corresponding to the lower MASS layer, is overlapped. In this case, because the SLODAR has higher resolution with respect to the MASS, we will use the SLODAR layers and will recalculate the energy in bin number 4 depending on the nature of the overlap.

Taking into account all the considerations above we have fixed the following rules for the restoration of the profiles.

A SLODAR layer fully inside a bin i

If the considered j-th SLODAR layer is fully inside the bin i (see Figure 7.5) having energy $\overline{C_n^2}(i)$, we simply add the SLODAR $C_{n,S}^2(j)$ and obtain

$$C_n^2(i) = \overline{C_n^2}(i) + C_{n,S}^2(j) \tag{7.6}$$

A SLODAR layer partially inside a bin i and partially inside a bin $(i+1)$

If the considered j-th SLODAR layer is partially inside the bin i and partially inside the bin $(i+1)$ (see Figure 7.6) we calculate the fractions of the area inside each bin and add the same $C_{n,S}^2(j)$ fractions to the respective bins. Because the SLODAR weighting functions are flat, the fractions of the layer area in each bin are proportional to

$$\begin{cases} frac_i \propto \frac{rec_{max,i} - sl_{min}}{\Delta h} & (\text{bin } i) \\ \\ frac_{i+1} \propto \frac{sl_{max} - rec_{max,i}}{\Delta h} & (\text{bin } i+1) \end{cases}$$

where sl_{min} and sl_{max} are the j-th SLODAR layer extremes in altitude. In this way the total $C_n^2(i)$ and $C_n^2(i+1)$ become

$$\begin{cases} C_n^2(i) = \overline{C_n^2}(i) + \left[C_{n,S}^2(j) \cdot frac_i\right] & (\text{bin } i) \\ \\ C_n^2(i+1) = \overline{C_n^2}(i+1) + \left[C_{n,S}^2(j) \cdot frac_{i+1}\right] & (\text{bin } i+1) \end{cases}$$

The bin is only partially filled by the *last* SLODAR layer

This is a particular case regarding only the 8-th SLODAR layer (see Figure 7.7). We define $A_{bin,i}$ the total area of the bin i. In this case we calculate the fraction of $A_{bin,i}$ filled by the last SLODAR layer ($j = 8$). Again, because the SLODAR weighting functions are flat, the filled fraction of $A_{bin,i}$ is simply

$$frac_{A,i} = \frac{sl_{max,8} - rec_{min,i}}{rec_{max,i} - rec_{min,i}} \tag{7.7}$$

where $sl_{max,8}$ is the upper extreme in altitude of the 8th SLODAR layer. At this point we fill the empty part of the bin i with a fraction of $\overline{C_n^2}(i)$ that is proportional to $1 - frac_{A,i}$

$$C_n^2(i) = \overline{C_n^2}(i) + \left[\frac{\overline{C_n^2}(i)}{frac_{A,i}}(1 - frac_{A,i})\right] = \overline{C_n^2}(i) + \Delta\overline{C_n^2}(i) \tag{7.8}$$

The added fraction $\Delta\overline{C_n^2}(i)$ is a part of the unsensed $Cu_{n,S}^2$ of the SLODAR and has to be removed from the total $Cu_{n,S}^2$.

Superimposition between SLODAR and MASS layers in bin number 4

In case the SLODAR layers are overlapping bin number 4, that correspond to the lower MASS rectangular layer which energy is $C_{n,M}^2(4)$, we distinguish between two cases:

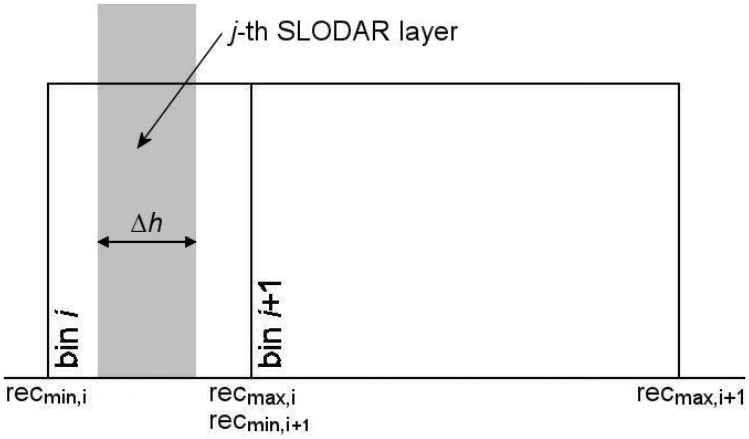

Figure 7.5: *A SLODAR layer (grey area) fully inside a bin i (white area).*

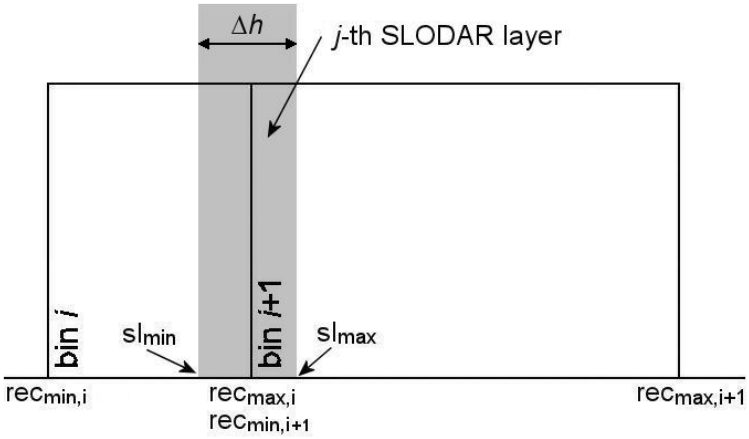

Figure 7.6: *A SLODAR layer partially inside a bin i and partially inside a bin $(i+1)$. Symbols are the same of Figure 7.5.*

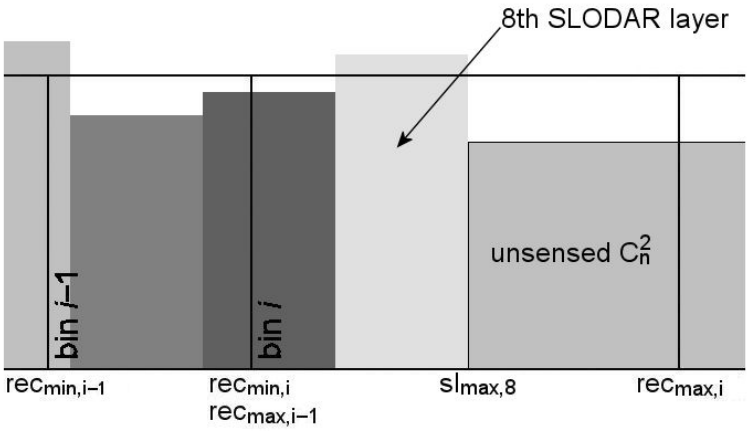

Figure 7.7: *The bin is only partially filled by the last SLODAR layer. Symbols are the same of Figure 7.5.*

- The SLODAR layer fully cover the bin: in this case, because the SLODAR has higher resolution with respect to MASS, the MASS layer is substituted by the calculated $C_n^2(i)$
- The SLODAR layer partially cover the bin: in this case we keep the biggest between $C_{n,M}^2(4)$ and $C_{n,S}^2(j)$ in order to not subtract energy to the layer

Normalization of the profile

As already mentioned, the DIMM is delivering the total turbulence energy $C_n^2(D)$ in the column of atmosphere observed. This means that $C_n^2(D)$ and the sum of the $C_n^2(i)$ of the restored layers must be equal. Often the DIMM and the MASS observe different portions of sky with respect to the SLODAR, thus a difference in the total sensed turbulent energy is expected. In this case, in order to be conservative, we force the restored energy to be equivalent to $C_n^2(D)$.
We define the energy of the ground layer as

$$C_n^2(GL) = C_n^2(D) - \sum_{i=4}^{9} C_{n,M}^2(i) \tag{7.9}$$

The sum of layers 1, 2, and 3 must be equal to the ground layer energy

$$C_n^2(1) + C_n^2(2) + C_n^2(3) = C_n^2(GL) \tag{7.10}$$

so we normalize the layers proportionally to their fraction

$$frac_{GL,i} = \frac{C_n^2(i)}{\sum_{i=1}^{3} C_n^2(i)} \qquad (i = 1, 2, 3) \tag{7.11}$$

Thus, the final values of the energy of the layers 1, 2, and 3 becomes

$$C_n^2(i) = C_n^2(GL) \cdot frac_{GL,i} \qquad (i = 1, 2, 3) \tag{7.12}$$

The case of missing of SLODAR data

In case of missing of SLODAR data we cannot resolve the layers 1, 2 and 3 because we do not have any information on the distribution of the energy in the ground layer. In this case, in order to maintain the grid, we consider the merging of the bins 1, 2 and 3 as a general unified ground layer having a thickness of 375 m and centered at 188 m (see Table 7.1 and Figure 7.4) which energy integral is the difference between the total DIMM C_n^2 and the total MASS $C_{n,M}^2(i)$, therefore the ground layer is filled using the DIMM data as established in equation 7.9

7.4 Results from the recombination

Having the exact amount of $C_n^2(i)$ in $[m^{1/3}]$ for each layer we can set the calculation of all the parameters we need for a complete analysis of the atmospheric turbulence. Figure 7.8 shows an example of a restored turbulence profile plot plus all the calculated parameters.

Turbulence profile

We calculate the turbulence profile normalized for the thickness Δh_i of each layer dividing the integral of the energy $C_n^2(i)$ in [$m^{1/3}$] by Δh_i in [m] (see Table 7.1)

$$\langle C_n^2(i) \rangle = \frac{C_n^2(i)}{\Delta h_i} \tag{7.13}$$

Percentage of energy in each layer

The percentage of turbulent energy in each layer is calculated using the elementary expression

$$\%C_n^2(i) = \frac{C_n^2(i)}{\sum_{i=1}^{9} C_n^2(i)} 100 \tag{7.14}$$

We also calculate the total percentage of energy in the ground layer and in the free atmosphere as follows

$$\%C_n^2(GL) = \frac{\sum_{i=1}^{3} C_n^2(i)}{\sum_{i=1}^{9} C_n^2(i)} 100 \qquad \%C_n^2(FA) = \frac{\sum_{i=4}^{9} C_n^2(i)}{\sum_{i=1}^{9} C_n^2(i)} 100 \tag{7.15}$$

Fried Parameter (r_0)

The Fried radius in [cm] is calculated applying known formulas from Roddier (1981) and Roddier (1989) (see also Section 2.4)

$$r_0 = \left[\left(6.67298 \cdot 10^{-13}\right) \sum_{i=1}^{9} C_n^2(i) \right]^{-3/5} \cdot 100 \tag{7.16}$$

Total seeing (ϵ)

Finally, the total seeing in [arcsec] is calculated using equation (2.18)

$$\epsilon = 0.98 \left[\frac{\lambda}{r_0(\lambda)} \right] \tag{7.17}$$

where $\lambda = 550$ nm.

Cumulative ascending and descendant seeing

We calculate the cumulative seeing starting from the ground layer (ascending, +), and from the free atmosphere (descendant,). For a j-th layer ($j = 1, 2, ..., 9$) the considered C_n^2 for the calculation of r_0 and therefore the seeing is expressed by the following formulas

$$C_n^2(+) = \sum_{i=1}^{j} C_n^2(i) \qquad C_n^2(-) = \sum_{j}^{i=8} C_n^2(i) \tag{7.18}$$

Coherence time (τ_0)

The coherence time is taken directly from the MASS data archive.

Slope of the power spectrum in the turbulence law (β)

The slope of the power spectrum in the turbulence law is taken directly from the SLODAR data archive. If $\beta = 11/3 = 3.67$ the Kolmogorov law is perfectly approximated.

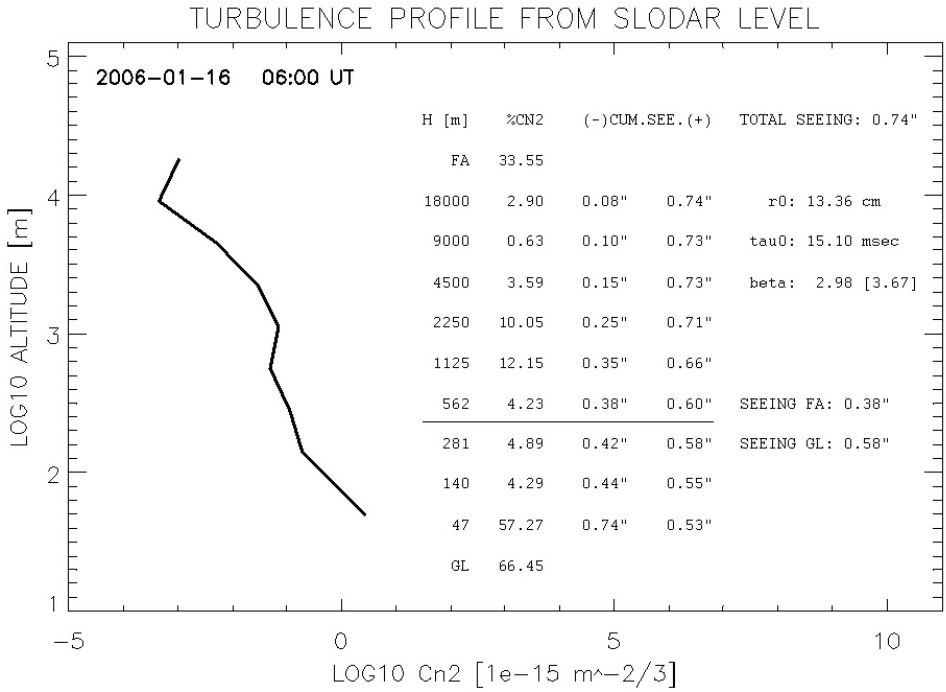

Figure 7.8: *An example of turbulence profile restored combining MASS and SLODAR profiles. The Figure shows one frame of the whole sequence of the atmospheric profile obtained in real time during the acquisition process. The plot reports all the parameters calculated from the recombination.*

Figure 7.8 is the milestone of our turbulence study. We can understand the contribution of each layer to the total turbulence in terms of percentage of energy and real seeing. The cumulative descending and ascendant seeing clearly predict the image quality that an observation can reach while excluding consecutively the turbulence contribution of each layer, simulating the improvement achieved by an hypothetic Adaptive Optic system conjugated to the considered layers. To conclude, the technique shown in the present Chapter constitutes a powerful tool in real-time studies of the turbulence evolution during Multi-Conjugated Adaptive Optics observations.

Chapter 8

The study of the evolution of the seeing at Paranal

Abstract

The application of the recombination of the turbulence profiles from MASS and SLODAR gives a detailed statistics of the evolution of the turbulence and the seeing at Paranal. The main goal of this study is to understand the differences between the image quality of the Very Large Telescopes and the DIMM seeing. We explain this difference in terms of variation of the ground layer. Some of the results shown in this Chapter are part of the E-ELT Design Study under the internal reference documentation number E-ELT-TRE-222-0215.

8.1 Introduction

Since the commissioning of the VLT the image quality delivered by the Unit Telescopes (UT) appears significantly better than the seeing measured by the DIMM. This difference is not negligible and not usual.
Already in 1999 the careful observations made with the test camera during the commissioning of UT2 revealed an alarming discrepancy between the UT2 image quality and the DIMM seeing of about 0.2 arcsec (Sarazin et al. 2008). During these tests that lasted several nights, UT2 was pointing at the same region of the sky and through the same filter as the DIMM, so there was no straightforward explanation for the lack of agreement. A clear manifestation of the discrepancy between the DIMM and the UT's is given by the time evolution of seeing on Paranal. In fact, the DIMM seeing worsen considerably over the past 17 years from a median value of 0.65 arcsec in 1990 to more than 1.10 arcsec in 2007. On the other hand, Sarazin et al. (2008) show that the image quality logged through the quality control process by FORS2 and ISAAC instruments seem to have improved with time.

8.2 Data analysis

To understand the seeing evolution we made use of long term recombined databases from Paranal DIMM, MASS and SLODAR in the period from 2 January 2005 to 30 June 2007. The three instruments provide measurements each minute. DIMM and MASS simultaneous

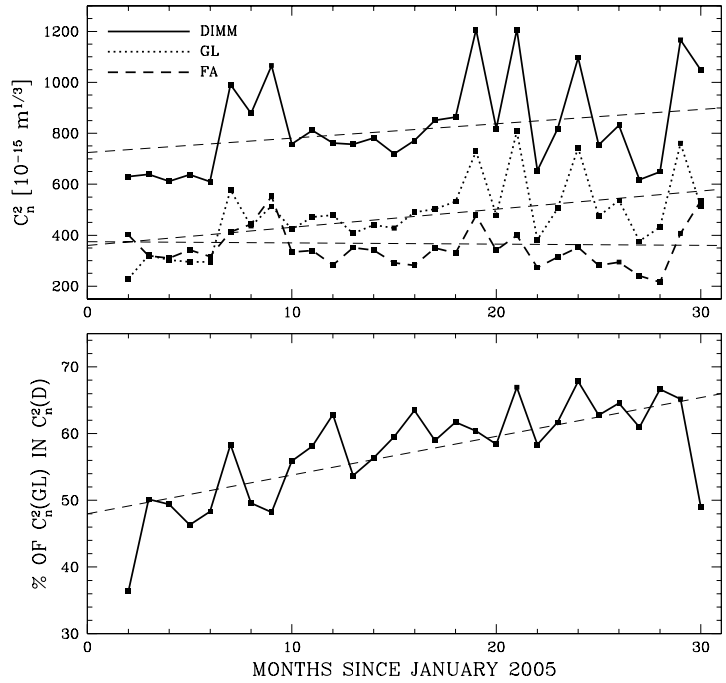

Figure 8.1: *(top) Comparison of the monthly evolution of the total C_n^2 of DIMM, GL and FA at Paranal between January 2005 and June 2007. The linear fit of the DIMM energy has a slope of* 6.7*, while it is* 8.4 *for the ground layer and* -1.6 *for the free atmosphere. (bottom) Percentage of $C_n^2(GL)$ in the total DIMM C_n^2. The linear fit of the points gives a slope of* 0.6*.*

databases are composed by 657 nights, while SLODAR database by 56 nights. In order to eliminate short-time fluctuations in the data, we proceed with a smoothing of the minute-by-minute measurements calculating 10-minutes averages. Then we calculate the averaged profile of each night, and from those we proceed to calculate the monthly averages.
Using the new grid defined in Chapter 7 we have the possibility to check the differences between the turbulence of the ground layer (GL) and the turbulence of the free atmosphere (FA) in order to analyze which of the two is having the stronger effect on the total seeing.

8.2.1 MASS+DIMM analysis

We consider the grid obtained using data from the DIMM and MASS, so according to Table 7.1 the ground layer extent from 0 to 375 m and is centered at 188 m. We compare the total $C_n^2(D)$ measured by the DIMM with the C_n^2 of the GL and the FA. Figure 8.1 (top) shows an increasing trend in the DIMM $C_n^2(D)$ ($80.4 \cdot 10^{-15}$ $m^{1/3}$ per year). This increasing is clearly driven by the increasing of the ground layer ($100.8 \cdot 10^{-15}$ $m^{1/3}$ per year), while the free atmosphere has a small negative trend ($-19.2 \cdot 10^{-15}$ $m^{1/3}$ per year).
This result is confirmed in Figure 8.1 (bottom) where we report the monthly percentages of the C_n^2 in the ground layer with respect to the total DIMM $C_n^2(D)$. As shown in the figure, the trend is increasing of $\sim$7% per year, and this demonstrates that the influence of the ground layer on the total seeing is becoming stronger.

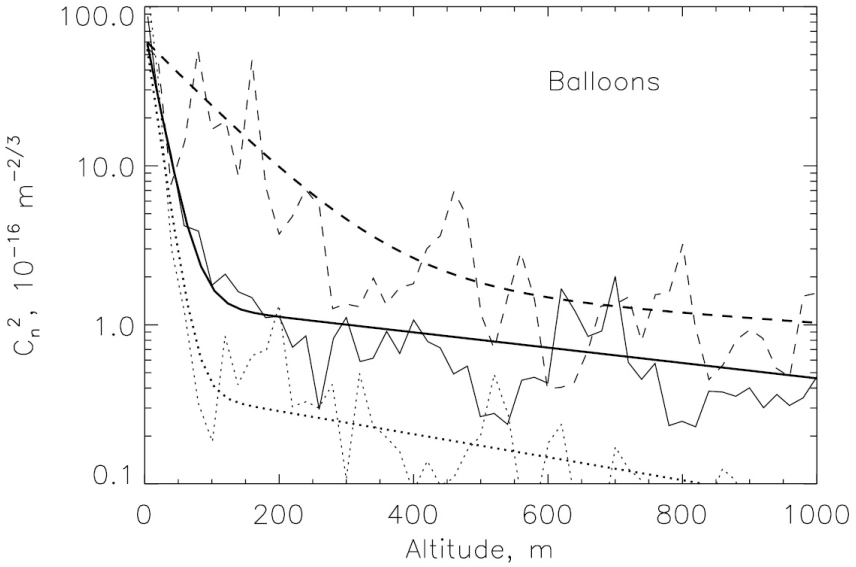

Figure 8.2: *Ground layer atmospheric turbulence model at Cerro Pachon (Chile) (Figure 6 in Tokovinin&Travouillon 2006).*

8.2.2 MASS+SLODAR analysis

Because the seeing is more affected by the ground layer, we decide to consider only the first 375 m above the observatory constituting the ground layer (layers 1, 2 and 3 in Table 7.1). To evaluate the contribution of the first layer to the total GL we have used the SLODAR monthly averages in order to compare the energy of layer 1, $C_n^2(1)$, extended between 0 and 94 m and centered at 47 m, with the sum of the energy of the layers 1, 2 and 3 that correspond to the total $C_n^2(GL)$.
The regression analysis is made imposing to have the zero point at 0 (no energy in the GL) and has a confidence level of 0.9. We obtain that typically the 76% of the $C_n^2(GL)$ is concentrated in the first layer. The (very few) points having poor correlation correspond to profiles in which the turbulence was dominated by the free atmosphere.

8.3 The surface layer hypothesis

It is known from the literature that the turbulence in the ground layer follows a log-normal distribution (Tokovinin&Travouillon 2006). Figure 6 from Tokovinin&Travouillon (2006) (Figure 8.2 in this Chapter) shows that in median seeing conditions 80-90% of the turbulence in the ground layer stays below a layer of about 100 m.
Using SLODAR data, the first layer of our grid is centered at 47 m above the ground and has a thickness of 94 m (see Table 7.1), comparable with the strongest layer in Figure 8.2. The primary mirror of the VLT Unit Telescopes is at about 15 m above the ground, while the domes are 30 m tall. Hypothesizing a non-perfect protection of the domes from turbulence around, we assume that the turbulence affecting the VLT has to be considered starting from an altitude of 20-30 m. This assumption is also valid considering an hypothetic ELT having the primary mirror at 50 m above the ground.
From the considerations above and following the assumption of Tokovinin&Travouillon

(2006), we formulate the hypothesis that the discrepancy between the UT's image quality and the DIMM at Paranal is due to a *surface layer* (SL) 20 m thick containing between 70% and 80% of the total turbulence of the ground layer; this surface layer stays below the UTs and is not seen by them. In this way we can affirm that the first layer of the recombined grid can be considered as representative of the surface layer below the UTs with an overestimation of about 10%.
If our hypothesis is correct, on a long time scale statistics the median image quality of the UTs should be equivalent, in the same time scale, to the median seeing calculated skipping the first layer of the grid.

8.4 The evolution of the seeing at Paranal

Considering the contribution of the first layer into the total GL we can recalculate the total seeing affecting the VLT Unit Telescopes using the 24% of $C_n^2(GL)$. Thus, the total integral of the turbulence above surface layer (ASL) affecting the UTs should be

$$C_{n,ASL}^2 = 0.24 C_n^2(GL) + C_n^2(FA) = C_n^2(\text{ASL}) + C_n^2(FA) \tag{8.1}$$

and the seeing is recalculated as

$$\epsilon_{\text{ASL}}^{5/3} = \epsilon^{5/3}(\text{ASL}) + \epsilon^{5/3}(FA) \tag{8.2}$$

In this way we skip the effects of the turbulence of the hypothesized surface layer. The $C_{n,ASL}^2$ can also be considered as the C_n^2 measured by an imaginary DIMM placed on one of the UT domes.
We recalculate the 10-minutes averaged profiles applying equation 8.1. Then, we calculate the median and the averaged seeing applying equation 8.2 on the entire database composed by the 10-minutes averages (20057 samples). We obtain that the median seeing is 0.61 ± 0.20 arcsec. The uncertainty is calculated as the median of the scatters of the values from the median seeing.
An independent analysis has been developed by J. Navarrete at ESO Paranal Observatory using 23888 empirical image quality samples from Unit Telescope 1 Shack-Hartmann (SH) at Cassegrain focus (Active Optics) in the and corrected for lenslet aberration. Data archive covered the period between September 2004 and June 2007. Figure 8.3 shows the distributions of the calculated ϵ_{ASL} and the UT1 SH image quality database from J. Navarrete analysis. The UT1 SH median image quality is 0.63 ± 0.19 arcsec, in very good agreement with results from our theoretical method.
We recalculate the C_n^2(ASL) monthly averages from the 10-minutes ones and the relatives monthly seeing. Figure 8.4 shows the regression analysis of the monthly image quality at UT1 SH versus the monthly ASL seeing derived from our theoretical calculations. The slope of the fit is imposed to be 1. We obtain a confidence level of 0.9.
All results above demonstrate the good reliability of the method when compared to real data. Most of the points in the plot in Figure 8.4 are below the $X = Y$ fit line. This is an evidence of the fact that the surface layer contribution to the total ground layer turbulence could be overestimated by a small amount compatible within the expected 10% error. Furthermore, the surface layer is expected to be not constant in time, varying within local meteorological conditions (wind and vertical temperature gradients).

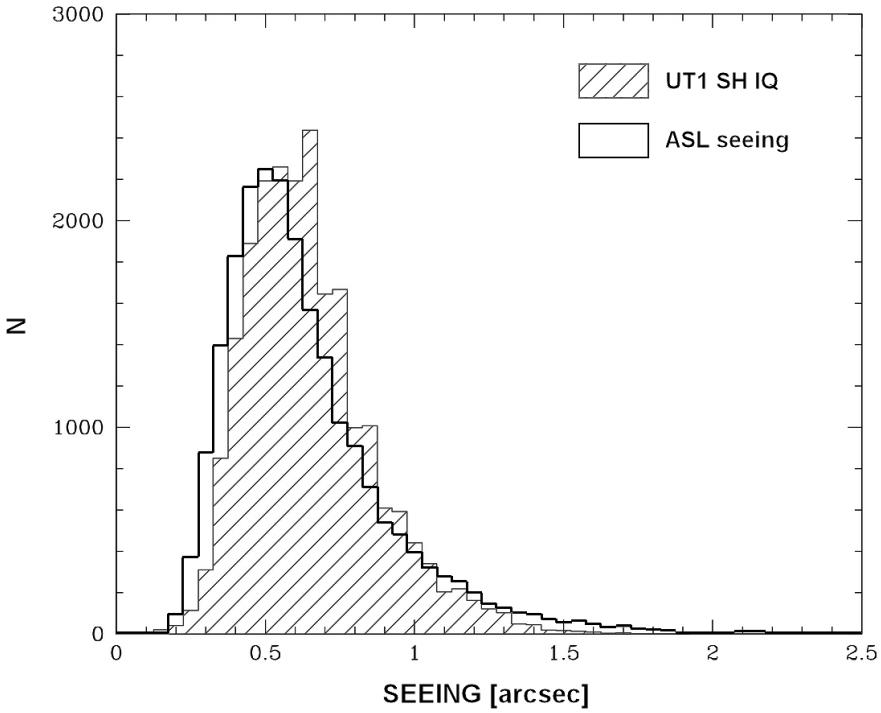

Figure 8.3: *Distribution of ϵ_{ASL} and UT1 SH image quality. The median ASL seeing is* 0.61 ± 0.20 *arcsec, while median image quality of UT1 SH is* 0.63 ± 0.19 *arcsec.*

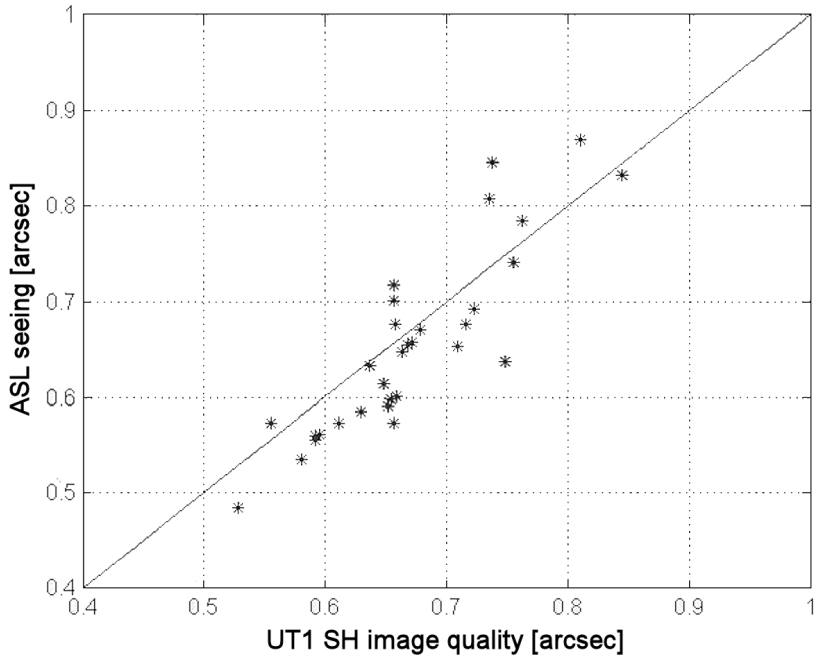

Figure 8.4: *Regression analysis of the monthly image quality at UT1 SH versus the monthly ASL seeing derived from our theoretical calculations (Lombardi et al. 2008b).*

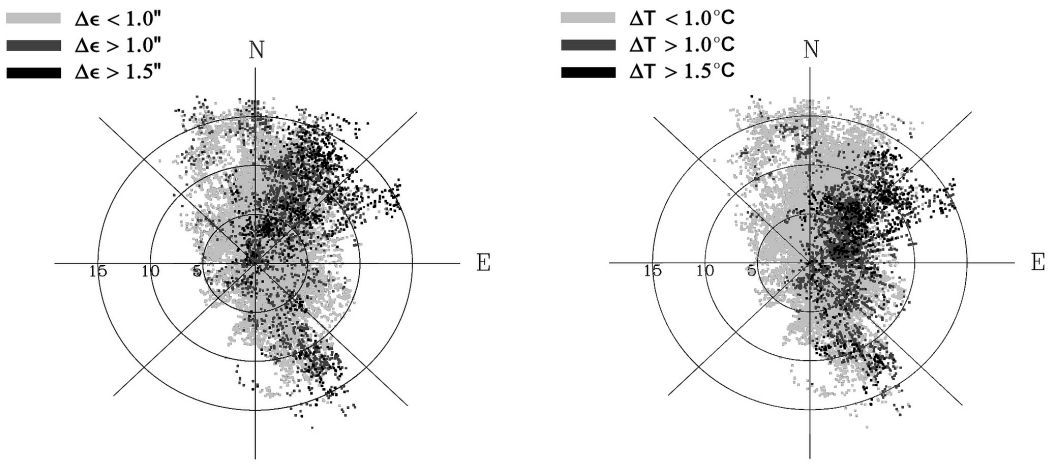

Figure 8.5: *(left) Paranal wind rose in connection with* $\Delta\epsilon = \epsilon_{DIMM}^{5/3} - \epsilon_{SH}^{5/3}$. *(right) Paranal wind rose in connection with* $\Delta T = T_{30} - T_2$ *(Sarazin et al. 2008).*

8.5 The origin of the surface layer

Data continuously provided by the Paranal meteorological tower can be used to investigate if meteorological parameters may influence the presence of the surface layer.
We assume the strength of the surface layer to be proportional to difference between the DIMM seeing and the UT1 SH image quality

$$\Delta\epsilon = \epsilon_{DIMM}^{5/3} - \epsilon_{SH}^{5/3} \tag{8.3}$$

Figure 8.5 (left) shows the wind rose of Paranal in connection with $\Delta\epsilon$, while Figure 8.5 (right) shows the connection between wind and the difference in temperature at 30 m and 2 m, $\Delta T = T_{30} - T_2$.
$\Delta\epsilon$ is higher when the wind comes from the NNE to SSE and this confirm results reported in Section 3.11.3 (see Table 3.18). It is interesting to note the also the temperature gradient is largest when the wind comes from the NNE and SSE. This suggests that the bad seeing occurs when the wind blows warm turbulent air from nearby summits along the Atacama fault over the top of the mountain. There is a weak trend of $\Delta\epsilon$ increasing with ΔT, indicating that local conditions can determine the properties of the surface layer (i.e. confining it to very low altitudes).
From considerations above we expect the wind distribution to have changed over the years. This has been already confirmed in Section 3.10 (see Figure 3.10 and Table 3.15), in fact since 1998 wind from north shows a clear decreasing trend through the years togheter with an increasing of the wind direction from NE to S.

8.6 Some conclusions and a begin

Figure 8.6 compares the monthly DIMM seeing and the monthly ASL seeing. An increasing trend in the DIMM seeing is evident ($\sim$0.1 arcsec per year) while the trend of the ASL seeing is clearly constant during the considered 30 months. Therefore, two conclusions raise from our analysis about the evolution of seeing at Paranal:

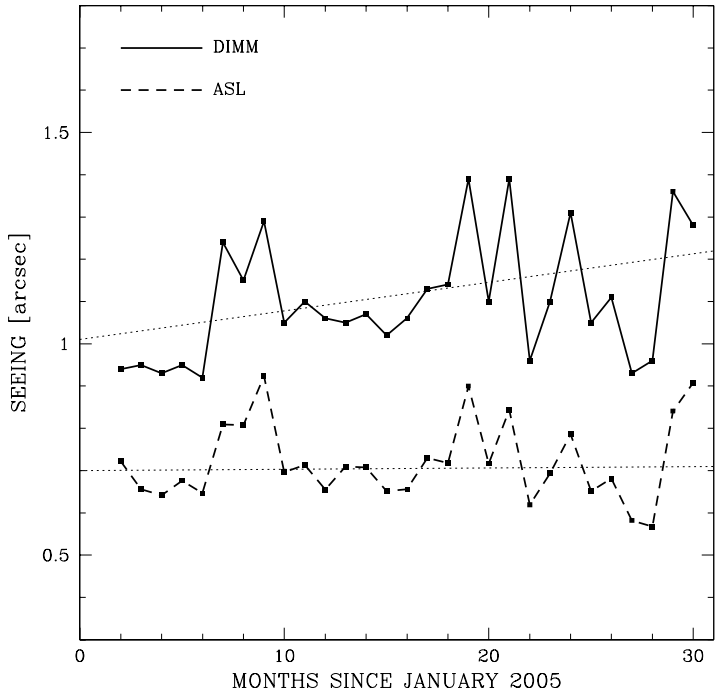

Figure 8.6: *Monthly DIMM seeing compared to ASL seeing. The monthly trend of the DIMM clearly increases (the trend is ∼0.1 arcsec per year), while the ASL seeing is almost constant in the considered period (the slope of the fit is null).*

The surface layer exists
: There is a worsening of the turbulence of the ground layer at Paranal, but this worsening is almost concentrated in the first 20 m above the ground in a way that is not significantly affecting the image quality of the VLT Unit Telescopes.

The surface layer is a product of local meteorological conditions
: The surface layer is strongest when the wind blows from the NNE and from the SSE. These winds have become increasingly since 1998, explaining why the surface layer appears more and more often. This change in the prevailing winds over Paranal can be due to climate change.

The conclusions above put two important questions:

1. What is the cause of the wind pattern change at Paranal since 1998?
2. Does the surface layer extends over the entire Paranal platform, or does it affect only the immediate surroundings of the DIMM?

The first question can be answered hypothesizing a connection with El Niño-La Niña episodes. From Table 3.6 we know that strong El Niño occurred in 1997. From the Thirty Meters Telescope (TMT) site testing campaign of Cerro Armazones, close to Paranal, we knew that the wind rose have not changed after 1998, and this suggest that the hypothesized connection with El Niño-La Niña is not the correct answer. Furthermore, there have been

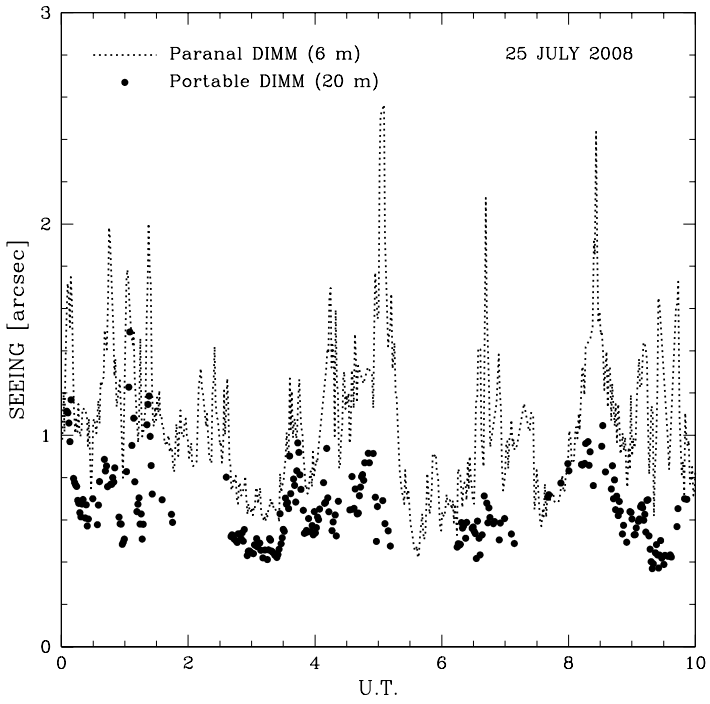

Figure 8.7: *25 July 2008: Paranal DIMM seeing at 6 m above the ground and Portable DIMM seeing at 20 m above the ground. There is a strong evidence of the presence of the surface layer below 20 m.*

others El Niño-La Niña episodes since 1998, which however do not affected the Paranal (or Armazones) winds in any significant way. The other important change that occurred in 1998 is that the last large structure on the Paranal summit (UT4) was completed, suggesting that perhaps the local orography of the mountain played a role in affecting the wind patterns. If this is the case, it may be that the surface layer is local and could change significantly on the platform.

Several experiments are undergoing at Paranal in the present. The studies involve a new generation SLODAR instrument able to sense the first 80 m above ground with a resolution of 10 m. A Lunar Scintillometer (LuSci) is also running together with the SLODAR in order to compare their results. LuSci is a turbulence profiler using a MASS-like profile restoration technique. It gives the turbulence profile at 4, 16, 50, and 200 m above ground by scintillation sensing of the lunar disc.

Finally, a Portable DIMM has been placed for 10 nights on the VLT Survey Telescope (VST) dome at 20 m above ground, measuring simultaneously with the DIMM at 6 m. Furthermore, four Sonic Anemometers measuring temperature and 3D wind at 6, 10, 20 and 30 m above ground ran simultaneously with the Portable DIMM. The data provided from such experiments are still under investigation, but preliminary analysis gave the strong impression that in peculiar conditions vertical temperature gradients coincide with the presence of the surface layer. Figure 8.7 shows an example of a night (25 July 2008) with a strong surface layer between 6 and 20 m.

Site testing campaigns must evolve to *surface layer analysis*, since up to now this has never been done. Micro-thermal towers and instruments sensitive to low turbulent layers (such as SLODAR) need to be correlated. The local orography of the site must be always taken into account, and the effects of changes in the prevailing winds modeled. In any case, a strong suggestion is given: do build your telescope as high above the ground as possible.

8.7 A median turbulence profile for Paranal

To finalize the results we have calculated the typical turbulence profiles for Paranal in case of good (33%), median and bad (66%) seeing using the MASS+DIMM recombination. These profiles are computed above surface layer in order to give a better estimation of the turbulence affecting the UTs. In this case, excluding the first layer, the remaining GL have a thickness of 280 m and is centered at 235 m. The results are reported in Table 8.1 and plotted in Figure 8.8. Although in this case the ground layer is not well resolved with respect to the MASS+SLODAR recombination, we consider these profiles more realistic because of the higher extension of the database.

Table 8.1: *MASS+DIMM. Typical profiles ASL for good (33%), median and bad (66%) seeing at Paranal. The statistics is made on the basis of 657 observing nights (20057 10-minutes averages) in the period between 2 January 2005 and 30 June 2007. For comparison also the typical seeing values from DIMM altitude (6 m) without SL subtraction are reported.*

Layer	h [m]	Δh [m]	$C_n^2(h)$ $\left[10^{-15}\mathrm{m}^{-2/3}\right]$ (ASL)		
	(above platform)		GOOD	MEDIAN	BAD
GL	235	280	0.25329	0.39586	0.53727
4	562	375	0.01558	0.06751	0.45174
5	1125	750	0.00099	0.00746	0.05373
6	2250	1500	0.00341	0.01700	0.06376
7	4500	3000	0.00827	0.01798	0.03482
8	9000	6000	0.00356	0.00559	0.00712
9	18000	12000	0.00303	0.00421	0.00505
SEEING ASL [arcsec]			0.42	0.61	0.97
SEEING AT 6 M [arcsec]			0.62	0.86	1.30

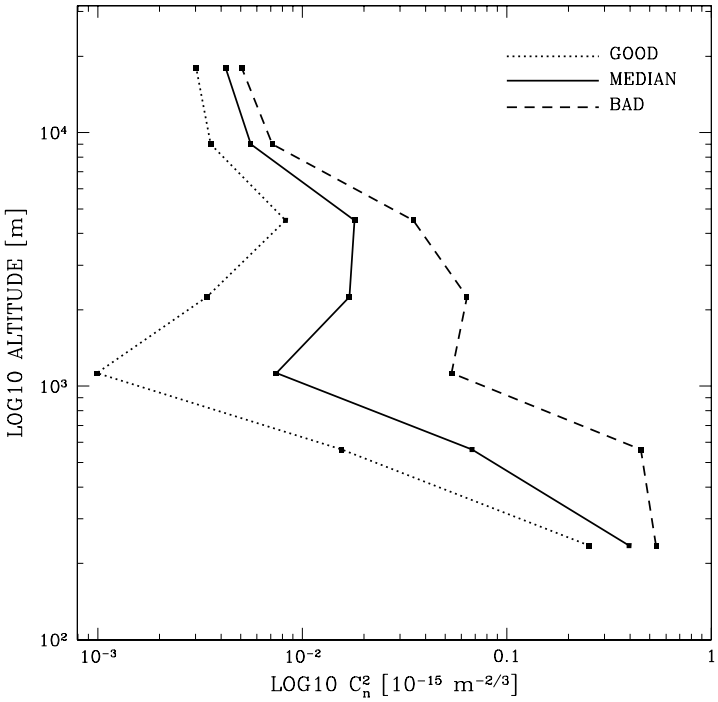

Figure 8.8: *MASS+DIMM. Typical profiles ASL for good (33%), median and bad (66%) seeing at Paranal. The statistics is made on the basis of 657 observing nights (20057 10-minutes averages) in the period between 2 January 2005 and 30 June 2007.*

Appendix A

The site testing for the European Extremely Large Telescope

Abstract

The E-ELT programme office is currently studying a number of potential sites for the E-ELT observatory. A decision on the site is foreseen by the end of 2009. A general overview of the E-ELT site selection process, its current status and my personal participation in the process is here described.

A.1 The site selection process

An artist impression of the 42 m E-ELT inside its dome is reported in Figure A.1. The E-ELT site selection process takes into account several aspects related not only to the sky quality of the site, but include more general scientific aspects, as well as parameters essential for construction and operations. In general, the considered aspects are the following[1]:

Atmospheric parameters
: Number of clear nights, infrared properties (height, temperature, precipitable water vapour, etc), seeing, atmospheric turbulence profile, mean coherence length and time, outer scale length, etc.

Geophysical properties
: Composition of the mountain soil, seismicity and presence of volcanos

Scientific synergy aspects
: Which facilities will be supported by the E-ELT and vice versa (e.g. VLT/VLTI, ALMA, surveys such as LSST, JWST, SKA, etc)

Construction aspects
: A flat surface equivalent to several football fields is needed, over 1500 containers will need to be delivered to the construction site from all over the world, construction will last several years

Logistical aspects
: For its operations, the observatory will require up to 10 MW of power

[1] See more details at http://www.eso.org/sci/facilities/eelt/site/index.html

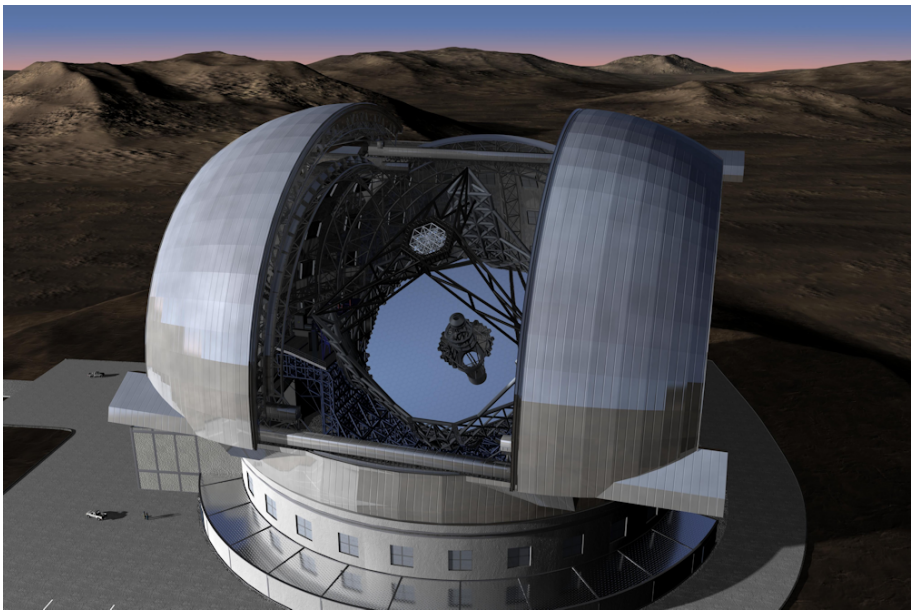

Figure A.1: *An artist impression of the European Extremely Large Telescope.*

Political agreements
: Political stability and future relationships and agreements within the hosting country will be established

A Site Selection Advisory Committee (SSAC) has been formed and is advising the ESO Director General who will deliver a proposal to the ESO council.
In this Appendix we will consider aspects related only to sky quality.

A.2 The working packages

For practical reasons, the work of the scientific teams involved in the study of the sites have been divided into four working packages (Vernin et al. 2008):

- WP12000: Site Characterization. Existing data and studies of several sites have been used for pre-selecting the candidate sites, furthermore previous works helped the definition of techniques and tools for the investigations
- WP12100: Review of parameters space. To characterize two top astronomical sites (ORM and North-Paranal) and to explore other alternatives (Macon in Argentina, Izaña in Canries and Aklim in Morocco) suitable to install an ELT under the best conditions
- WP12200: Instrumentation, measurement and modeling. It is dedicated to design, build and operate a standard equipment in all the sites and to perform long term campaign
- WP12300: Large Scale Atmospheric Properties. Investigates wavefront properties over large baselines (50-100 m) corresponding to the size of the future ELT, as well as the ne characterization of the optical turbulence within the boundary layer

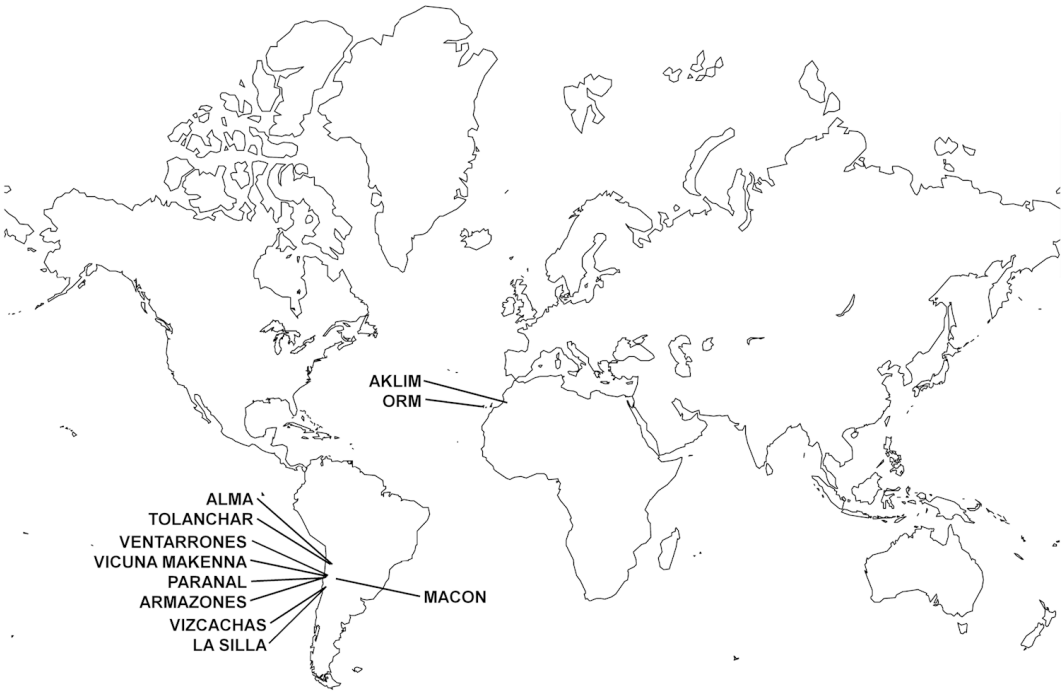

Figure A.2: *A World map reporting the locations of the candidate sites and nearby existing facilities.*

A.3 The sites

At the present five sites are under investigation. Figure A.2 shows the locations of the candidate sites and nearby already existing facilities:

Ventarrones (North-Paranal)
: Cerro Ventarrones is located in the Atacama Desert in northern Chile. It has an altitude of 2800 m a.s.l. and is about 50 km north-east far from Paranal

Vizcachas (La Silla)
: Cerro Vizcachas is a mountain of 2450 m a.s.l. few kilometers far from La Silla Observatory in the chilean Norte Chico

Macon
: The Cordón Macon is a mountain ridge in the Puna in northern Argentina, at same latitude of Paranal. The location of the site is the southern part of the ridge, at an altitude of 4760 m a.s.l.

Observatorio del Roque de los Muchachos
: The ORM has been extensively studied in this thesis. The altitude of the chosen location in the ORM is of about 2350 m a.s.l.

Aklim
: The Aklim peak is located in the Atlas Mountains in Morocco. The site has an altitude of about 2400 m a.s.l.

Table A.1: *Instruments and tools used for the E-ELT site testing campaigns in each site (X if used, – if not used).*

Instrument/tool	Ventarrones	Vizcachas	Macon	ORM	Aklim
MASS-DIMM	X	X	X	X	X
GL profilers	X	X	–	X	–
G-SCIDAR	X	–	–	X	–
ASC	X	X	X	X	X
AWS	X	X	X	X	X
Satellites (aerosols)	–	–	X	X	X
Satellites (climatology)	X	X	X	X	X
Meteorological models	X	X	X	X	X
Soil mechanics	X	X	X	–	X
Seismicity	X	X	X	–	X

In addiction to the mentioned "official" sites, other two locations are going to be investigated in the incoming months. The first is Cerro Tolanchar (4770 m a.s.l.) located in northern Chile, close to Chajnantor site hosting ALMA, while the second is Cerro Vicuña Makenna (3150 m a.s.l.) located in front of Cerro Ventarrones, close to Paranal. These sites have been added for several reasons in order to provide a wider range of choice in the Southern Hemisphere in an area – northern Chile – where several other European astronomical facilities are present (ALMA and Paranal) which are important for both scientific synergy and logistical aspects.

A.4 Instruments and tools

WP12200 is funded the the European Community under the Framework Programme 6 (FP6) ELT Design Study "Site Characterization" project.
A set of common instruments is used in the long term campaigns in each site. In addition, on the basis of the peculiarities of each site (i.e. seismicity, dust pollution, high relative humidity etc.), other tools can be added in the investigations. The list of the instruments and tools is reported below, while Table A.1 shows the installations present in each investigated site (Vernin et al. 2008).

- MASS-DIMM (a complex having a MASS and a DIMM in the same telescope), for atmospheric turbulence profiling
- Ground layers profilers (SLODAR, LuSci, SODAR etc.), for investigation of the lower atmosphere and the surface layer
- Generalized-SCIDAR (G-SCIDAR), for atmospheric turbulence profiling
- All Sky Camera (ASC), for cloud coverage statistics
- Automatic weather station (AWS), for the measurement of meteorological parameters (temperature at different altitudes, pressure, relative humidity, dew point temperature, wind direction and wind speed at different altitudes)
- Satellites, for high altitudes aerosols and dust pollution
- Satellites, for wide scale climatological studies
- Meteorological models, for climatological predictions in the incoming years

- Soil mechanics, for mountains composition
- Seismicity statistics, for safety of the observatory

A.5 My personal participation in the E-ELT site testing

In the present I am involved as ESO staff in the site selection of the E-ELT. In particular I am in charge of the infrastructures and operations at Ventarrones (North-Paranal) and Macon (Argentina). In the incoming future I will also be in charge of the installation of the MASS-DIMM facilities at Tolanchar and Vicuña Makenna.
In general, the work consist in several tasks. First, the mounting, test and calibration of the new instrumentation (telescope, MASS-DIMM, computers, network) at Paranal. Optical devices such as MASS-DIMM are aligned and collimated in the Optical Laboratory (Figure A.3) and then calibrated and tested on sky (Figure A.4). After that the instruments are transported to the sites for installation and maintenance of the Astronomical Site Monitors (Figures A.5 and A.6). Visits at sites are frequents (no less than 15 nights per month). In such occasions nighttime outdoor work is done, often in adverse conditions such as extremely cold temperatures, strong winds and staying for several hours on the 5 m telescope tower. Figure A.7 shows the typical installations of the Astronomical Site Monitors.
In addition, several new studies are undergoing at Paranal and Ventarrones using SLODAR, LuSci (Figure A.8) and Portable DIMM (Figure A.9) in order to characterize in detail the ground layer turbulence at the site. These studies are completely new in the literature, since new generation instruments are used on sky for the first time, and new theories about the ground layer dynamic are going to be formulated and then extended to the future chosen E-ELT site.

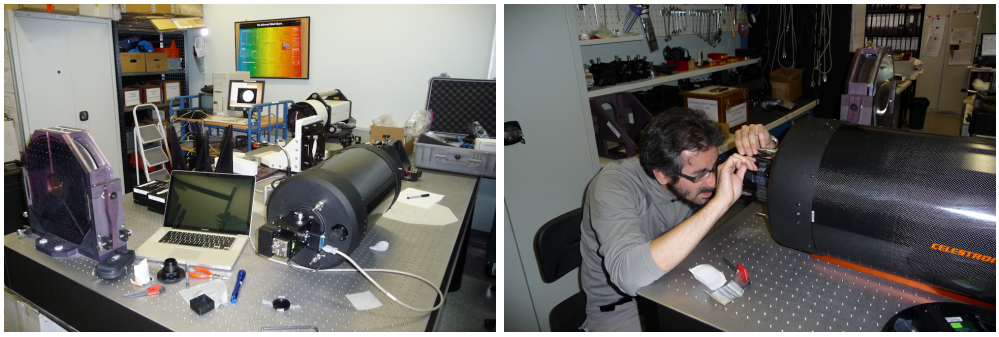

Figure A.3: *Celestron C11 telescope and MASS-DIMM #31 device on the Optical Laboratory during alignment and collimation procedure. The telescope and the MASS-DIMM #31 will be installed at Tolanchar in the incoming months.*

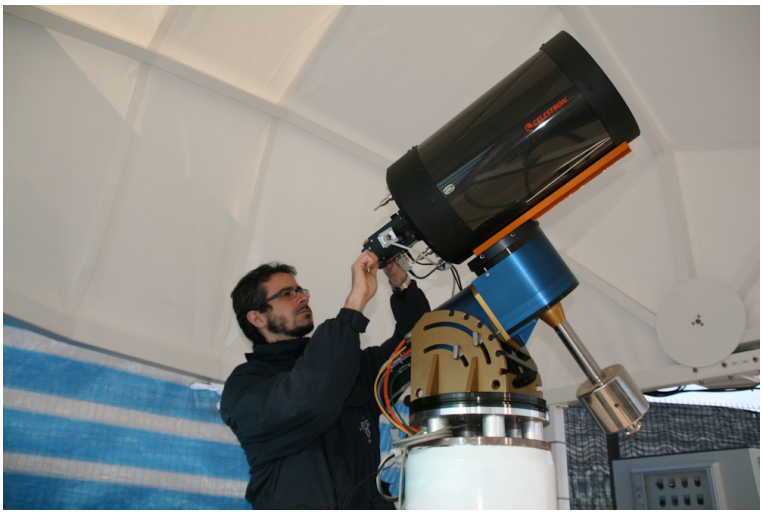

Figure A.4: *Preparation of the MASS-DIMM on Astelco EQ mount for nighttime test observations at Paranal.*

Figure A.5: *Astronomical Site Monitor installation at Macon in May 2008.*

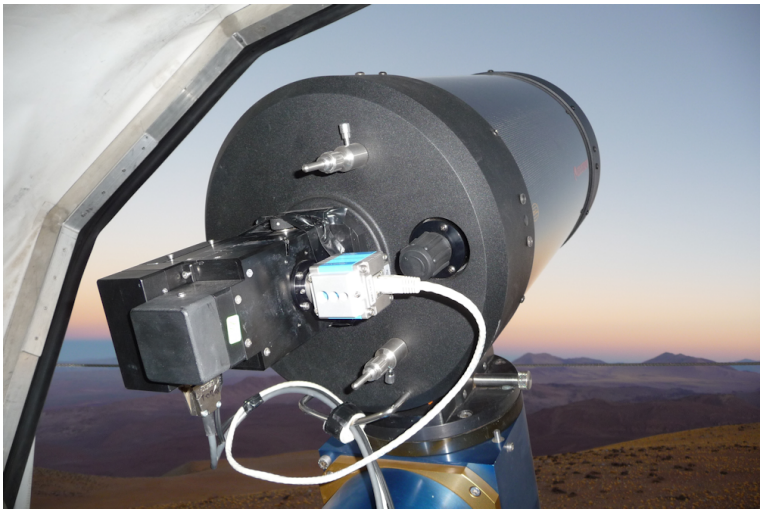

Figure A.6: *MASS-DIMM instrument installed at Macon.*

Figure A.7: *This picture shows the typical Astronomical Site Monitor installations. From left to right: a hut for nighttime work, solar panels for energy providing, the 5 m MASS-DIMM tower and the automatic weather station. The picture has been taken at Macon in July 2008.*

Figure A.8: *Lunar Scintillometer observing at Paranal in February 2008.*

Figure A.9: *Portable DIMM on a 10 m tower at Ventarrones at the end of February 2008. The experiment consists in the comparison between the MASS-DIMM at 6 m and the DIMM at 11 m for surface layer analysis.*

Bibliography

[2000] Allen, C.W., 2000, Allen's Astrophysical Quantities, 4th edition, ed. A. N. Cox

[2002] Amico, P., Cuby, J. G., Devillard, N., Jung, Y., Lidman, C. January 30, 2002, ISAAC Data Reduction Guide 1.5, ESO Very Large Telescope

[1976] Barletti, R., Ceppatelli, G., Paternò, L., Righini, A., & Speroni, N. 1976, J. Opt. Soc. Am., 66, 1380

[1977] Barletti, R., Ceppatelli, G., Paternò, L., Righini, A., & Speroni, N. 1974, Appl. Opt., 16, 2419

[2005] Bertolin, C. 2005, private communication

[1970] Brandt, P. N. 1982, Solar Phys., 13, 243

[1982] Brandt, P. N., & Woehl, H. 1982, A&A, 109, 77

[1985] Brandt, P. N., & Righini, A. 1985, Vistas Astron., 28, 437

[1995] Burki, G., Rufener, F., Burnet, M., Richard, C., Blecha, C., Bratschi, P. 1995, A&AS 112, 383

[2006] Butterley, T., Wilson, R. W., and Sarazin, M. 2006, MNRAS, 369, 835

[1997] Caporali, A., & Barbieri, C. 1997, The Astronomic and Geodetic Coordinates of the Telescopio Nazionale Galileo, Canary Islands, TNG Technical Report no. 64

[1980] Carlson, T. N., & Benjamin, S. G. 1980, J. Atmos. Sci., 37, 193

[1973] Ceppatelli, G., & Righini, A. 1973, Struttura microtermica della bassa atmosfera e qualit dell'immagine solare, Contributi dell'Osservatorio Astrofisico di Arcetri, fascicolo 285, pag. 154, in Riv. It. Geof. vol. XXII n. 3/4

[2004] Cuby, J. G., Jaunsen, A. O., Johnson, R., Lidman, C., Mason, E., Moutou, C. December 15, 2004, ISAAC User Manual (Issue 2), ESO Very Large Telescope

[1956] Font-Tullot, I. 1956, The weather in the Canary Islands (in Spanish) Madrid, Servicio Nacional de Meteorología, Publ. Ser. A 26

[1987] Fouquart, Y., Bonnel, B., Chaoui Roquai, M., Santer, R., & Cerf, A. 1987, J. Climate Appl. Meteor., 26, 28

[1966a] Fried, D. L. 1966, J. Opt. Soc. Am., 56, 1372

[1966b] Fried, D. L. 1966, J. Opt. Soc. Am., 56, 1380

[1998] Frogel, J. A. 1998, PASP 110, 200

[2004] Ghedina, A., Pedani, M., Guerra, J. C., Zitelli, V., & Porceddu, I. 2004, SPIE, 5489, 227

[2006] Gilmozzi, R. 2006, Sci. Am., 294, 64

[2005] Graham, E. 2005, Astroclimatological report for the observatory of La Palma, Canary Island, report for The Large Synoptic Survey Telescope project

[1998] Guerrero, M. A., García-López, R. J., Corradi, R. L. M., Jiménez, A., Fuensalida, J. J., et al. 1998, New Astron. Rev., 42, 529

[2000] Jabiri, A., Benkhaldoun, Z., Vernin, J., & Muñoz-Tuñon, C. 2000, A&A, 147, 271

[1998] Jiménez, A., Gonzalez Jorge, H., & Rabello-Soares, M. C. 1998, A&AS, 129, 413

[1965] Johnson, H. L., 1965, Comm. Lunar and Planetary Lab. 3, 67

[1990] Hardy, J. 1990, Adaptive optics for astronomical telescopes, Oxford University Press

[1975] Hayes, D. S. & Latham, D. W. 1975, Ap.J. 197, 593

[1992] Holton, J. R. 1992, in International Geophysics Ser. 48, An Introduction to Dynamic Meteorology, 3rd edition, ed. R. Dmowska, & J. R. Holton, Academic Press Inc.

[1981] Huber, P. J. 1981, Robust Statistics, ed. J. Wiley, & Sons, New York

[1993] Hubin, N. & Noethe, L. 1993, Science, 262, 1390

[1999] Hsu, N. C., Herman, J. R., Torres, O., Holben, B. N., Tanre, D., et al. 1999, J. Geophys. Res., 104, 6269

[1980] Kittel, C., & Kroemer, H. 1980, Thermal Physics, ed. W. H. Freeman Company (2nd ed.)

[1941] Kolmogorov, A. 1941, Local structure of turbulence in incompressible uids with very high reynolds number. Dan. S.S.S.R., 30, 229

[2003] Le Roux, B. 2003, Commande optimale en optique adaptative classique et multiconjuguée, Université de Nice SophiaAntipolis

[1998] Leinert, C., Bowyer, S., Haikala, L. K., Hanner, M. S., Hauser, M. G., Levasseur-Regourd, A. C., Mann, I., Mattila, K., Reach, W. T., Schlosser, W., Staude, H. J., Toller, G. N., Weiland, J. L., Weinberg, J. L., Witt A. N. 1998, A&AS 127, 1

[2006] Lombardi, G., Zitelli, V., Ortolani, S., & Pedani, M. 2006, PASP, 118, 1198 (Paper I)

[2007] Lombardi, G., Zitelli, V., Ortolani, S., & Pedani, M. 2007, PASP, 119, 292 (Paper II)

[2008a] Lombardi, G., Zitelli, V., Ortolani, S., Pedani, M., & Ghedina, A. 2008a, A&A, 483, 651 (Paper III)

[2008b] Lombardi, G., Navarrete, J., & Sarazin, M. 2008b, Combining turbulence profiles from MASS and SLODAR. A study of the evolution of the seeing at Paranal, SPIE Proc., 7012-21

[2009] Lotz, J. 2009, http://www.pha.jhu.edu/ jlotz/aoptics/empaper2.html

[1998] Mahoney, T., Muñoz-Tuñón, C., & Varela, A. M. 1998, ed. C. Muñoz-Tuñón, New Astron. Rev. 42, 409

[1979] Manduca, A. & Bell R.A. 1979, PASP 91, 848

[1999] Marley, M. S., Gelino, C., Stephens, D., Lunine, J. I., & Freedman, R. 1999, ApJ, 513, 879

[1977] Mathis, J. S., Rumpl, W., & Nordsieck, K. H. 1977, ApJ, 217, 425

[1974] McInnes, B., & Walker, M. F. 1974, PASP, 86, 529

[1973] Moroder, E., & Righini, A. 1973, A&A, 23, 307

[1998] Muñoz-Tuñón, C., Varela, A. M., & Mahoney, T. 1998, New Astr. Rev., 42, 409

[1985] Murdin, P. 1985, Vistas Astron., 28, 449

[1990] Murphy, J. R., Toon, O. B., Haberle, R. M., & Pollack, J. B. 1990, J. Geophys.Res., 95, 14629

[2008] Ortolani, S. 2008, private communication

[2003] Patat, F. 2003 A&A, 401, 797

[1977] Patterson, E. M. 1977, Appl. Opt., 16, 2414

[1981] Patterson, E. M. 1981, Science, 211, 836

[1998] Persson, S. E., Murphy, D. C., Krezeminsky W., Roth M., and Rieke M. J. 1998, Ap.J. 116, 2475

[2002] Porceddu, I., Zitelli, V., Buffa, F., & Ghedina, A. 2002, SPIE, 4844, 358

[1991] Racine, R., Salmon, D., Cowley, D., & Sovka, J. 1991, PASP, 103, 1020

[1978] Roddier, F., Ricort, G., & Roddier, G. 1978, Opt. Comm., 24, 281

[1981] Roddier, F. 1981. The effects of atmospheric turbulence in optical astronomy, volume 19. North Holland

[1989] Roddier, F. 1989. Optical propagation and image formation through the turbulent atmosphere. volume 274 of Proceedings of the NATO Advanced Study Institute, page 33. Kluwer Academic Publisher

[1986] Rufener, F. 1986, A&A 165, 275

[1999] Sandrock, S., Amestica, R., & Sarazin, M. 1999, VLT Astronomical Site Monitor ASM Data User Manual (VLT-MAN-ESO-17440-1773; Garching: ESO)

[1990] Sarazin, M. & Roddier., F. 1990, A&A, 227, 294

[1992] Sarazin, M. 1992, Update of environamental conditions on ESO Observatories, VLT-TRE-ESO-17400-0347, European Southern Observatory

[2004] Sarazin, M. 2004, http://www.eso.org/gen-fac/pubs/astclim/paranal/asm/verif/20years-ClimatologyofParanal-Oct2004.pdf

[2008] Sarazin, M., Melnick, J., Navarrete, J., & Lombardi, G. 2008, The ESO Messenger, 132, 11

[2004] Siher, E. A., Ortolani, S., Sarazin, M., & Benkhaldoun, Z. 2004, SPIE, 5489, 138

[1987] Stickland, D. J., Lloyd, C., Pike., C. D., & Walker, E. N. 1987, The Observatory, 107, 74

[1988] Stull, R. B. 1988, An introduction to Boundary Layer Meteorology, Kluwer Academic Publishers, Dordrecht, The Netherlands

[1961] Tatarskii, V. I. 1961, Wave Propagation in a Turbulent Medium, Dover, New York

[1938] Taylor, G. I. 1938, Proc. Roy. Soc. London, A132, 476

[2002] Tokovinin, A. & Kornilov, V. 2002, Measuring turbulence profile from scintillations of single stars. In: Astronomical Site Evaluation in the visible and Radio Range, Eds. Benkhaldoun, Z., Muñoz-Tuñon, C., Vernin, J., ASP Conf. Ser., 266, 104

[2006] Tokovinin, A. & Travouillon, VT. 2006, MNRAS, 365, 1235

[2008] Tokovinin, A. 2008, http://www.ctio.noao.edu/ atokovin/profiler/index.html

[2008] Vernin, J., Muñoz-Tuñón, C., & Sarazin, M. 2008, E-ELT site characterization status, SPIE Proc., 7012-64

[2001] Wanner, H., Bronnimann, S., Casty, C., Gyalistras, D., Luterbacher, J., Schmutz, C., Stephenson, D. B., & Xoplaky E. 2001, Surv. Geophys., 22, 321

[1987] Whittet, D. C. B., Bode, M. F., & Murdin, P. 1987, Vistas Astron., 30, 135

[2002] Wilson, R. W. 2002, MNRAS 337, 103.

[1980] Wiscombe, W. J. 1980, Appl. Opt., 19, 1505

[1995] Zago, L. 1995, PhD Thesis: The effect of the local atmospheric environment on astronomical observations, Thése No. 1394, Ecole Polytechnique Féderale de Lausanne

Acknowledgments

Valentina Zitelli, from INAF Bologna, gave me the possibility to *have* a possibility: this thesis. She is the scientific supervisor of this research, and she was always extremely patient and smart in teaching and giving her support, sustain (scientific and moral!), suggestions and useful blames, also when I was 13.000 km far.

Professor Bruno Marano, from Department of Astronomy at University of Bologna, is the academic supervisor of this research. He considered that Doctorate in Astronomy should deal as well with a number of interdisciplinary and technical issues, mostly critical for future developments. He also believed that I was the right one to do that. I will never stop to thank him for his deed of trust in me.

Professor Sergio Ortolani, from Department of Astronomy at University of Padova, has been my Master Degree thesis advisor in 2004. Since then he never left me in the development of my scientific profile and career. If today I can defend this thesis, is primarily thank to his constant support.

Marc Sarazin, from ESO, has been my "on field" tutor. He patiently taught me everything about the instruments. He also taught me how to be a scientist in a desert in the middle of nowhere, in the dark and with temperatures like -10°C. Without his sustain I could never have understood which are my personal skills, both technicals and "theoretical". But, the most important, he trusted in me when I had to expose our recombination theory at SPIE Conference 2008: this I will never forget.

Julio Navarrete por su amistad, el soporte en las operaciones en Paranal y por inventarse "GL": el nombre perfecto!

Rodrigo Hinojosa, Herman Barrios y Sergio Orrego por acompañarme, ayudarme y brindarme su amistad en las noches heladas de Atacama.

Jorge Melnick for the extremely helpful comments and bright ideas on the surface layer

The various works at the sites could never have been done, and could not go on in the future, without the irreplaceable support of Fernando Luco with his Team, and Paranal Engineers (in particular Serge Guniat and Juan Carlos Palacios).

DCS IT support en Santiago y Paranal nunca se han quejado cuando yo me quejaba! No se como iva a hacer todo mi trabajo sin la ayuda de Manuel Arratia, Ivan Carmona, Jose Flores, Papito, Oscar Molina, Andres Herrera, Hernan Fernandez y Jose Francisco Riquelme.

The Astornomers, the TiO's and all the friends in Paranal, La Silla and Santiago, for giving a little warm in the cold nights.

A los hermanos de Tolar Grande y Cordoba, sobre todo a Ruben (otras cumbres nos esperan!), Victor, Diego, Pablo, Hernan y Elsa.

A los amigos de las Canarias, Jose Miguel, Hector con su familia, Jesus, Marcos y Nieves

A Emanuela, Gaspare, Elena, Paola e Gianni per i preziosi consigli e per sopportarmi ogni volta che mi lamento del freddo e del vento (e non solo)!

A los increibles amigos de Santiago, porque nunca me dejaron solo: Alessandro (più cileno di un cileno del Chile), Omar (y toda su familia), Andrea, Lucia, Sandra y Paulina con la Victoria.

A tutti gli amici di Bologna, per aver condiviso questi anni di duro lavoro e le occasioni di "svago": Giuseppe, Rodrigo, Daniela, Laura, Annamaria, Francesco, Gabriele, Antonio, Federico, Alessio, Manolo e tutti gli altri.

Agli Amici di sempre, perché *ognuno ha gli amici che si merita*: Nando, Gabriele, Simone, Gianluca, Diego, Adele, Carlo, Alberto, Illen, Walter, Marco, il Doc, Filomena, Pamela, TurboPeppe, Fabietto e tutti gli altri.

A los Andes, por ser majestuosos y darme la tranquilidad y la fuerza para seguir caminando.

A las Cumbres, a las Aguas y a los Hielos Patagónicos, porque un día regresaré, lo juro.

Saretta, per la pazienza e l'amore mai venuti a mancare nonostante le distanze che a volte sembrano incolmabili.

Ai Nonni, perché non ci sono più, ma ci sono sempre.

Mamma, Papà, Marcello, per essere i punti cardine della mia vita.

GIANLUCA LOMBARDI
Taranto, Bologna, Santiago, Atacama or elsewhere
March 9, 2009